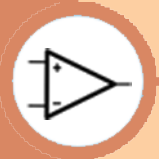


I J
A T
E S²

International Journal of Advances in Telecommunications Electrotechnics, Signals and Systems

a publication of the International Science and Engineering Society



**Vol. 2, No. 2
2013**

ISSN: 1805-5443

www.ijates.org

I J
A T
E S² **International Journal of
Advances in Telecommunications
Electrotechnics, Signals and Systems**

a publication of the International Science and Engineering Society

Vol. 2, No. 2, 2013

ISSN: 1805-5443

Editor-in-Chief

Jaroslav Koton, Brno University of Technology, Czech Republic

Co-Editors

Ondrej Krajsa, Brno University of Technology, Czech Republic

Norbert Herencsar, Brno University of Technology, Czech Republic

Bilgin Metin, Bogazicy University, Turkey

Editorial Board

Oguzhan Cicekoglu, Bogazicy University, Turkey

Sergey Ryvkin, Trapeznikov Institute of Control Sciences Russian Academy of Sciences,
Russian Federation

Hongyi Li, Bohai University, China

Emilia Daniela Bordencea, TU Cluj-Napoca, Romania

Albert Abilov, Izhevsk State Technical University, Russian Federation

Joze Guna, University of Ljubljana, Slovenia

Jaroslav Koton, Brno University of Technology, Czech Republic

Ondrej Krajsa, Brno University of Technology, Czech Republic

Aims and Scope

The International Journal of Advances in Telecommunications, Electronics, Signals and Systems (IJATES²) is an all-electronic international scientific journal with the aim to bring the most recent and unpublished research and development results in the area of electronics to the scientific and technical societies, and is supported by the ISES (International Science and Engineering Society, o.s.). The journal's scope covers all the aspects of telecommunication, signal processing, theory and design of circuits and systems for electronics.

The IJATES² is ready to publish experimental and theoretical full papers and letters submitted by prospective authors. Paper submitted for publication must be written in English and must follow a prescribed format. All papers are subjected to a critical peer-review prior to publication.

The IJATES² is an open access journal which means that all content is freely available without charge to the user or his/her institution. Users are allowed to read, download, copy, distribute, print, search, or link to the full texts of the articles in this journal without asking prior permission from the publisher or the author. This journal provides immediate open access to its content on the principle that making research freely available to the public supports a greater global exchange of knowledge.

www.ijates.org

Copyright © 2012-2013, by ISES, o.s.

All the copyright of the present journal belongs to the International Science and Engineering Society, o.s.

CONTENTS

Vol. 2, No. 2, 2013

ISSN: 1805-5443

A Current-mode Electronically Controllable Multifunction Biquadratic Filter Using CCCIs <i>Montree Siripruchyanun, Somchai Srisakultiew, and Supawat Lawanwisut</i>	45
Pulse Wave Velocity Measuring System using Virtual Instrumentation on Mobile Device <i>Razvan Alin Ciobotariu</i>	51
FIR Filter Implementation Based on the RNS with Diminished-1 Encoded Channel <i>Dragana Uros Zivaljevic, Negovan Stamenković, and Vidosav Stojanović</i>	56
Estimation of Direction of Arrival of Multiple Sound Sources in 3D Space Using B-Format <i>Hasan Khaddour, Jiri Schimmel, and Michal Trzos</i>	63
Definition of Typical Textures of Sedimentary Grains Using Co-occurrence Features and K-means Clustering Technique <i>Aleš Křupka</i>	68
Programmable Cellular Automata Encryption Algorithm Implemented in Reconfigurable Hardware <i>Petre Anghelescu</i>	73
Precision Full-Wave Rectifiers with Current Active Elements and Current Biasing <i>Lukas Langhammer and Jan Jerabek</i>	79
Novel Robust Optimization and Power Allocation of Time Reversal-MIMO-UWB Systems in an Imperfect CSI <i>Sajjad Alizadeh and Hossein Khaleghi Bizaki</i>	84

A Current-mode Electronically Controllable Multifunction Biquadratic Filter Using CCCII

S. Srisakultiew¹, S. Lawanwisut² and M. Siripruchyanun³

Abstract— This article presents a current-mode multifunction biquadratic filter performing completely standard functions low-pass, high-pass, band-pass, band-reject and all-pass functions. The circuit principle is based on second-generation current-controlled current conveyor (CCCII) with three input terminals and one output terminal. The features of the circuit are that, the pole frequency can be tuned via the bias currents. The circuit topology is very simple, consisting of merely 2 CCCIIs and 2 grounded capacitors. Without any external resistor and using only grounded elements, the proposed circuit is very comfortable to further develop into an integrated circuit architecture. The PSpice simulation results are shown. The given results agree well with the theoretical anticipation. The total power consumption is approximately 1.87mW at $\pm 1.5V$ power supply voltages.

Keywords— Current-mode, Biquadratic filter, CCCII.

I. INTRODUCTION

An analog filter is an important building block, widely used for continuous-time signal processing. It can be found in many fields: including, communications, measurement, and instrumentation, and control systems [1-2]. One of most popular analog filters are multi-purpose and universal filters that can be classified either as multi-input and single-output (MISO) filter [3] or single-input and multi-output (SIMO) filter [4]. The MISO current-mode filters have rather simple structures [5]. Recently, a multifunction filter working in current-mode has being been more popular than the voltage-mode type. Since the last two decades, there has been much effort to reduce the supply voltage of analog systems. This is due to the demand for portable and battery-powered equipment. Since a low-voltage operating circuit becomes necessary, the current-mode technique is ideally suited for this purpose. Actually, a circuit using the current-mode technique has many other advantages, such as, larger dynamic range, higher bandwidth, greater linearity, simpler circuitry and lower power consumption [6-7].

A second generation current conveyor (CCII) is a reported active component, especially suitable for a class of analog signal processing [8]. The fact that the device can operate in both current and voltage-modes provides

flexibility and enables a variety of circuit designs. In addition, it can offer advantageous features such as high slew-rate, high-speed, wide bandwidth and simple implementation [8-9]. However, the parasitic resistance at X (R_x) port cannot be controlled so when it is used in some circuits, it unavoidably requires some external passive components, especially the resistors. This makes it not appropriate for IC implementation due to occupying more chip area, consuming high power and without electronic controllability. On the other hand, the introduced second-generation current-controlled conveyor (CCCII) [10] has the advantage of electronic adjustability over the CCII. Also, the use of multiple-output current conveyors is found to be useful in the derivation of current-mode single-input three-output filters using a reduced number of active components [11-12].

From our survey, it is found that several implementations of current-mode multifunction biquadratic filters have been reported [13-33]. Unfortunately, these reported circuits suffer from one or more of following weaknesses:

- Excessive use of the passive elements, especially the external resistors [15-17, 19, 23-26, 28-33].
- Lack of electronic adjustability [15-17, 19, 23-26, 28-32].
- Require changing circuit topologies to achieve several functions [14-16, 20-21, 24-26].
- Some outputs of the filter responses are not in high output impedance [13-14, 15, 17-18].
- Cannot provide completely standard function [19-20, 22, 24-25, 28-29, 31]

The aim of this paper is to propose a current-mode multifunction biquadratic filter, emphasizing on use of the CCCIIs and grounded capacitors. The features of the proposed circuit are that, the proposed multifunction biquadratic filter can completely provide 5 functions which are low-pass high-pass band-pass band-reject and all-pass, without changing circuit topology, the circuit description is very simple, employing only grounded capacitors as passive components, thus it is suitable for fabricating in monolithic chip. The quality factor and pole frequency can be electronically adjusted. The PSpice simulation results are also shown, which are in correspondence with the theoretical analysis.

II. PRINCIPLE OF OPERATION

A. Multiple-output Current Controlled Current Conveyor (MO-CCCII)

Since the proposed circuit is based on MO-CCCII, it will be introduced in this section. Typically, the MO-CCCII is a

Manuscript received October 20, 2012, revised January 18, 2013.

S. Srisakultiew¹ Computer Engineering, Faculty of Engineering and Architecture, Rajamangala University of Technology Isan, 744 Suranarai Rd. Nai-Maung, Maung, Nakhonratsima, 30000, Thailand (e-mail: somchaikorat2008@hotmail.com)

S. Lawanwisut² Dept. of Information and Communication Engineering, Faculty of Industrial Technology, Thepsatri Rajabhat University, Lopburi, 15000, Thailand (e-mail: s.lawanpisut@hotmail.com)

M. Siripruchyanun³ Dept. of Teacher Training in Electrical Engineering, Faculty of Technical Education, King Mongkut's University of Technology North Bangkok, Bangsue, Bangkok, 10800, Thailand (e-mail: mts@kmutnb.ac.th)

doi: 10.11601/ijates.v2i2.11

versatile analog building block which including 3-ports, x, y and z. The matrix-relationship between voltage and current are variables among port x, y and z of ideal following matrix equation in Eq. (1). Where the positive and negative signs of the current i_z denote the positive (CCCII+) and negative (CCCII-), respectively, and R_x is an intrinsic resistance of CCCII. The x-terminal resistance is calculated by Eq. (2) and V_T is the thermal voltage. Fig.1 (a) and (b) illustrates the symbol and equivalent circuit, respectively.

$$\begin{bmatrix} i_y \\ v_x \\ i_z \end{bmatrix} = \begin{bmatrix} 0 & 0 & 0 \\ 1 & R_x & 0 \\ 0 & \pm 1 & 0 \end{bmatrix} \begin{bmatrix} v_y \\ i_x \\ v_z \end{bmatrix}, \quad (1)$$

where

$$R_x = \frac{V_T}{2I_B}, \quad (2)$$

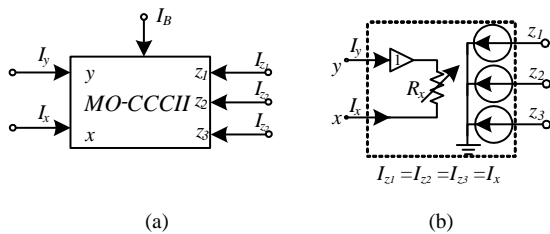


Fig. 1. MO-CCCII (a) Symbol, (b) Equivalent circuit.

B. Implementation of the filter

The proposed filter is designed by cascading summing currents and the current-mode lossless integrator as systematically shown in Fig. 2. From block diagram in Fig. 2, its transfer function can be found to be [34-36]

$$I_{out} = \frac{(s^2 + sb + ab)I_{in3} + sbI_{in2} + abI_{in1}}{s^2 + sb + ab}. \quad (3)$$

From Eq. (3), the pole frequency (ω_0) and quality factor (Q_0) of each filter response can be expressed as

$$\omega_o = \sqrt{ab}, \quad (4)$$

and

$$Q_o = \sqrt{\frac{a}{b}}. \quad (5)$$

It is found that the pole frequency and the quality factor can be adjusted by either a or b.

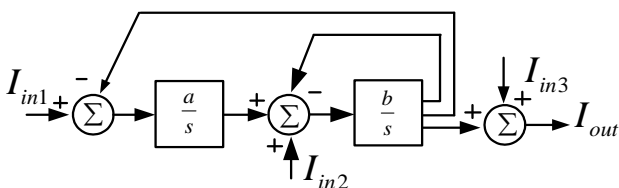


Fig 2. Block diagram for filter implementation [34].

C. Proposed current-mode multifunction biquadratic filter

The filter is designed by cascading the lossless integrators as systematically shown in Fig. 3. From circuit in Fig. 3, the current transfer function can be expressed as

$$\frac{I_{out}}{I_{in}} = \frac{1}{s\tau}, \quad (6)$$

where $\tau = \frac{2I_B}{CV_T}$

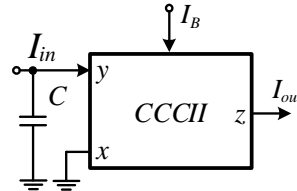


Fig. 3. Lossless integrator using CCCII.

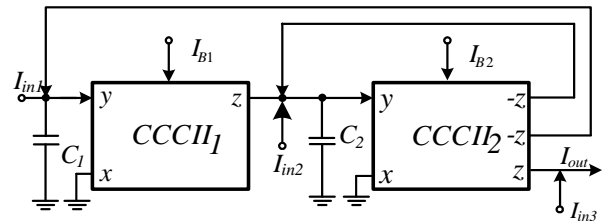


Fig. 4. Proposed current-mode multifunction biquadratic filter.

The complete current-mode multifunction biquadratic filter is shown in Fig. 4. From Eq. (7), the output current of the circuit in Fig. 4 can be obtained as

$$I_{out} = \frac{\left(s^2 + \frac{s}{C_2R_{x2}} + \frac{1}{R_{x1}R_{x2}C_1C_2}\right)I_{in3} + \frac{s}{C_2R_{x2}}I_{in2} + \frac{1}{R_{x1}R_{x2}C_1C_2}I_{in1}}{s^2 + \frac{s}{C_2R_{x2}} + \frac{1}{R_{x1}R_{x2}C_1C_2}}. \quad (7)$$

From Eq. (7), the all standard transfer functions can be obtained by selecting appropriate inputs by following conditions

1) If $I_{in} = I_{in1}$, and $I_{in2} = I_{in3} = 0$, a low-pass function is achieved at the output. The transfer function can be written to be

$$\frac{I_{out}}{I_{in}} = \frac{1}{R_{x1}R_{x2}C_1C_2} \cdot \frac{1}{s^2 + \frac{s}{C_2R_{x2}} + \frac{1}{R_{x1}R_{x2}C_1C_2}}. \quad (8)$$

2) If $I_{in} = -I_{in1} = -I_{in2} = I_{in3}$, a high-pass function can be obtained. The transfer function can be written to be

$$\frac{I_{out}}{I_{in}} = \frac{s^2}{s^2 + \frac{s}{C_2R_{x2}} + \frac{1}{R_{x1}R_{x2}C_1C_2}}. \quad (9)$$

3) If $I_{in} = I_{in2}$, and $I_{in1} = I_{in3} = 0$, the obtained output function is a band-pass. The transfer function can be given by

$$\frac{I_{out}}{I_{in}} = \frac{\frac{s}{C_2 R_{x2}}}{s^2 + \frac{s}{C_2 R_{x2}} + \frac{1}{R_{x1} R_{x2} C_1 C_2}} \quad (10)$$

4) If $I_{in} = I_{in3} = -I_{in2}$, and $I_{in1} = 0$, a band-reject function is provided. The transfer function can be written to be

$$\frac{I_{out}}{I_{in}} = \frac{s^2 + \frac{1}{R_{x1} R_{x2} C_1 C_2}}{s^2 + \frac{s}{C_2 R_{x2}} + \frac{1}{R_{x1} R_{x2} C_1 C_2}} \quad (11)$$

5) If $I_{in} = I_{in3} = -2I_{in2}$, and $I_{in1} = 0$, an all-pass filter is obtained. The transfer functions can be written to be

$$\frac{I_{out}}{I_{in}} = \frac{s^2 - \frac{s}{C_2 R_{x2}} + \frac{1}{R_{x1} R_{x2} C_1 C_2}}{s^2 + \frac{s}{C_2 R_{x2}} + \frac{1}{R_{x1} R_{x2} C_1 C_2}} \quad (12)$$

The selection to obtain each function can be achieved by digital method, the digital selection circuit can be found in [37].

The pole frequency (ω_0) and quality factor (Q_0) can be expressed to be

$$\omega_0 = \frac{1}{\sqrt{C_1 C_2 R_{x2} R_{x3}}} \quad (13)$$

and

$$Q_0 = \sqrt{\frac{C_1 R_{x2}}{C_2 R_{x3}}} \quad (14)$$

where $R_{x1} = \frac{V_T}{2I_{B1}}$, $R_{x2} = \frac{V_T}{2I_{B2}}$. Thus, we get

$$\omega_0 = \frac{2}{V_T} \sqrt{\frac{I_{B1} I_{B2}}{C_1 C_2}} \quad (15)$$

and

$$Q_0 = \sqrt{\frac{C_1 I_{B2}}{C_2 I_{B1}}} \quad (16)$$

From Eqs. (15) and (16), the pole frequency can be electronically controlled, which is independent from the quality factor by varying I_{B1} and I_{B2} (keeping their ratio constant). Furthermore, bandwidth of the system can be expressed by

$$BW = \frac{\omega_0}{Q_0} = \frac{2I_{B1}}{V_T C_1} \quad (17)$$

We found that the bandwidth can be linearly controlled by I_{B1} .

D. Sensitivity analysis

The sensitivities of the proposed filter can be found to be:

$$S_{C_1, C_2}^{\omega_0} = -\frac{1}{2}, \quad S_{I_{B1}, I_{B2}}^{\omega_0} = \frac{1}{2} \quad (18)$$

$$S_{I_{B2}, C_1}^{Q_0} = \frac{1}{2}, \quad S_{I_{B1}, C_1}^{Q_0} = -\frac{1}{2} \quad (19)$$

and

$$S_{V_T, C_2}^{BW} = -1, \quad S_{I_{B1}}^{BW} = 1 \quad (20)$$

Therefore, all active and passive sensitivities are equal or less than unity in magnitude.

E. Non-ideal Case

For non-ideal case, the voltage and current tracking errors of the MO-CCCII effect on the performance of the proposed filter. By routine analysis, the MO-CCCII with non-ideal case can be respectively characterized with the following equations

$$I_y = 0, V_x = \beta V_y + R_x I_x, I_z = \alpha I_x \quad (21)$$

$\beta = 1 - \varepsilon_v$ ($\varepsilon_v \ll 1$) is the voltage gain, where ε_v is the voltage tracking error from V_y to V_x of MO-CCCII. α is the current gain equal to $1 - \varepsilon_i$ ($\varepsilon_i \ll 1$), where ε_i is the output current tracking error of MO-CCCII. In the case of non-ideal and reanalysis of proposed filter circuit in Fig. 4, it yields the output current as

$$I_{out} = \frac{\left(s^2 + \frac{s\alpha_2\beta_2}{C_2 R_{x2}} + \frac{\alpha_1\alpha_2\beta_1\beta_2}{R_{x1} R_{x2} C_1 C_2} \right) I_{in3} + \frac{s\alpha_2\beta_1}{C_2 R_{x2}} I_{in2} + \frac{\alpha_1\alpha_2\beta_1\beta_2}{R_{x1} R_{x2} C_1 C_2} I_{in1}}{s^2 + \frac{s\alpha_2\beta_2}{C_2 R_{x2}} + \frac{\alpha_1\alpha_2\beta_1\beta_2}{R_{x1} R_{x2} C_1 C_2}} \quad (22)$$

In this case, the ω_0 and Q_0 are changed to

$$\omega_0 = \sqrt{\frac{\alpha_1\alpha_2\beta_1\beta_2}{C_1 C_2 R_{x1} R_{x2}}} \quad (23)$$

and

$$Q_0 = \sqrt{\frac{\alpha_2\beta_2 C_1 R_{x1}}{\alpha_1\beta_1 C_2 R_{x2}}} \quad (24)$$

while BW is still equal to Eq. (17). These errors affect the sensitivity to temperature and high frequency response of the proposed circuit, then the MO-CCCII should be designed to achieve these errors as low as possible, for example, using a high performance current mirror. Consequently, these deviations are very small and can be ignored.

III. SIMULATION RESULTS

To prove and investigate the performances of the proposed circuit, the PSpice simulation program was used for the examination. The PNP and NPN transistors employed in the CCCII were simulated by respectively using the parameters of the PR200N and NR200N bipolar transistors of ALA 400 transistor array from AT&T [38]. Fig. 5 depicts schematic description of the CCCII used in the simulations. The circuit was biased with $\pm 1.5V$ power supplies voltage, $C_1=C_2=1nF$, $I_{B1}=I_{B2}=50\mu A$. The results shown in Fig. 6 are the gain responses of the proposed multifunction biquadratic filter. It is clearly seen that it can provide low-pass high-pass band-pass band-reject and all-pass functions dependent on selection as depicted in Eqs. (8)-(12). Fig. 7 shows gain responses of band-pass function, where I_{B1} and I_{B2} are equally set to keep the ratio to be constant and changed for several values. It is found that pole frequency can be adjusted without affecting the quality factor as analyzed in Eqs. (15)-(16). Fig. 8 shows gain responses of band-pass function where I_{B1} is set for several values. It is found that pole frequency can be adjusted electronically. Fig. 9 shows evaluated pole frequency compared with simulation result. The transient and spectrum responses of the proposed filter from band-pass function for center frequency of 547.293kHz can be seen in Fig. 10 and 11, respectively, where THD is 0.227%. Total power consumption obtained from PSpice is about 1.87mW.

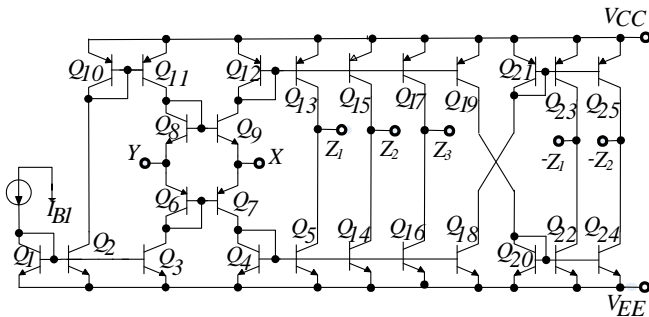


Fig. 5. Internal construction of MO-CCCII.

IV. CONCLUSION

The current-mode multifunction biquadratic filter with three input terminals and one output terminal based on CCCII has been presented. The advantages of the proposed circuit are that, it performs completely standard functions, which are low-pass high-pass band-pass band-reject and all-pass functions from the same circuit configuration, without component matching conditions and changing circuit topology. The pole frequency can be electronically adjusted without affecting the quality factor. The circuit description comprises only 2 MO-CCCII and 2 grounded capacitors. With mentioned features, it is very suitable to realize the proposed circuit in monolithic chip to use in battery-powered, portable electronic equipment such as wireless communication system.

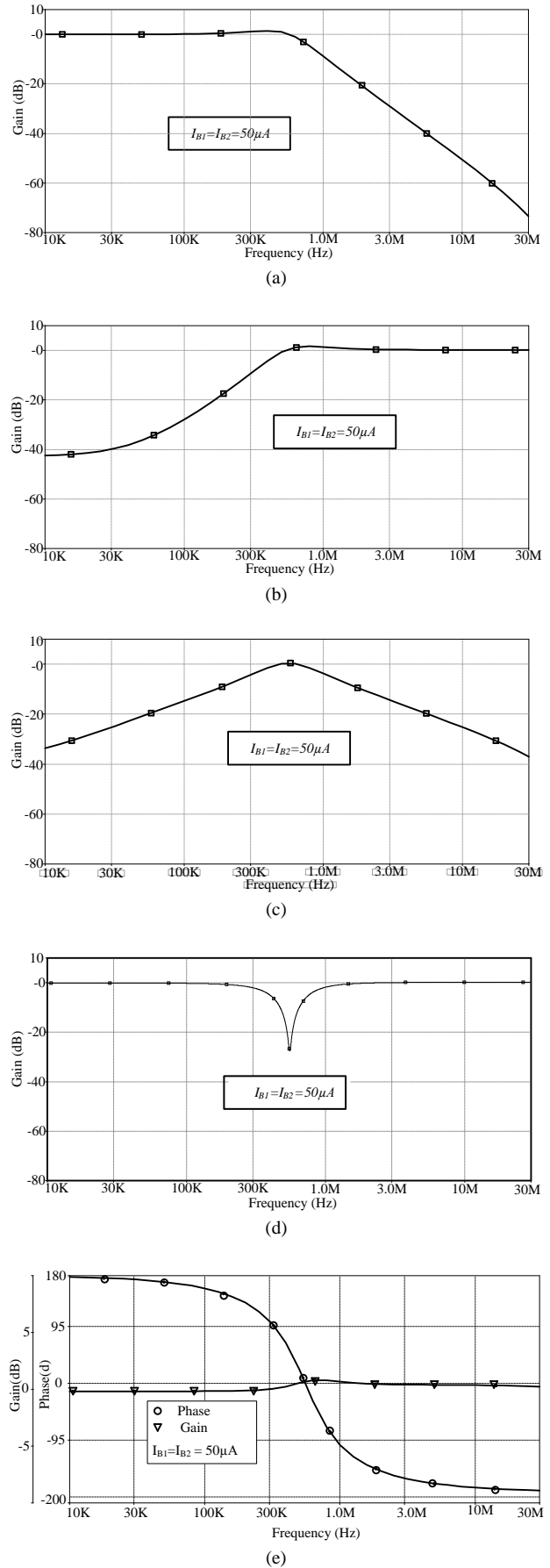


Fig. 6. Gain responses of the biquadratic filter (a) LP (b) HP (c) BP (d) BR (e) AP.

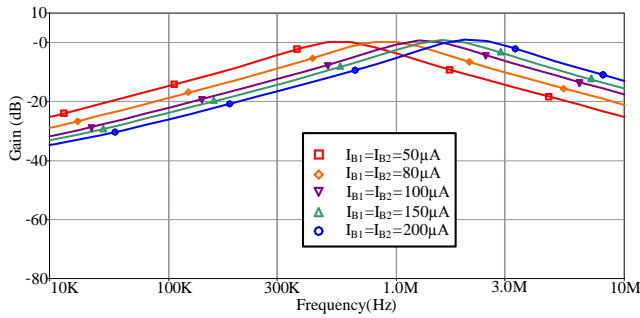


Fig 7. Band-pass responses for different values of I_{B1} and I_{B2} with keeping their ratios constant.

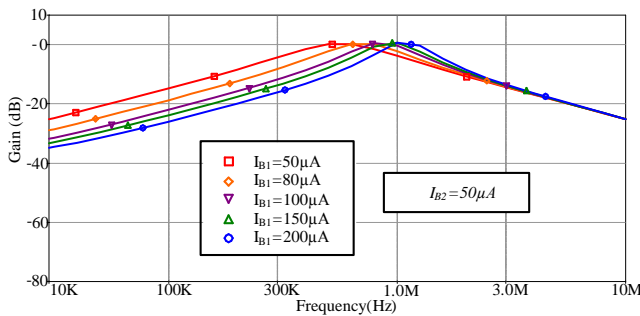


Fig 8. Current-mode bandpass responses for different values of I_{B1}

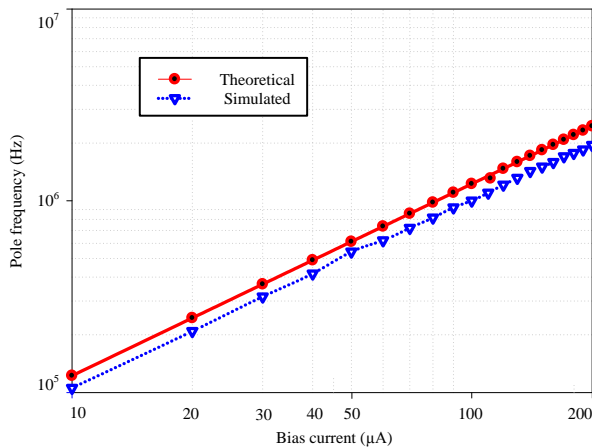


Fig 9. Deviation of the calculated pole frequency compared with the simulated value.

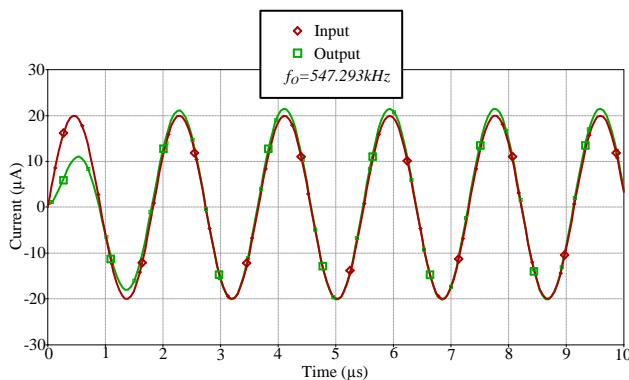


Fig 10. Transient responses at center frequency of 547.293kHz obtained from the proposed filter for BP function.

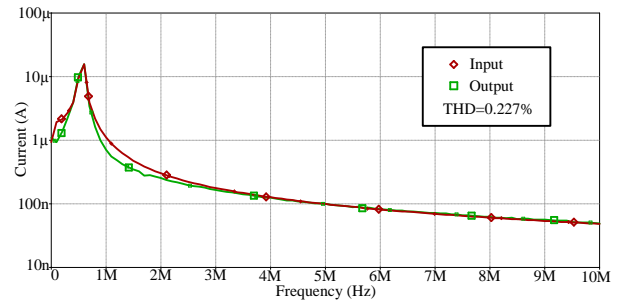


Fig. 11. Frequency spectrum of obtained signal in Fig. 10.

REFERENCES

- [1] A. S. Sedra, and K. C. Smith, *Microelectronic circuits*, 5rd ed., Florida: Holt, Rinehart and Winston, 2003.
- [2] M. A. Ibrahim, S. Minaei, and H.A. Kuntman, "A 22.5 MHz current-mode KHN-biquad using differential voltage current conveyor and grounded passive elements," *International Journal of Electronics and Communications (AEU)*, vol. 59, pp. 311-318, 2005.
- [3] W. Chunhua, L. Haiguang, and Z. Yan, "Universal current-mode filter with multiple inputs and one output using MOCCII and MO-CCCA," *International Journal of Electronics and Communications (AEU)*, vol. 63, no. 6, pp. 448-453, 2009.
- [4] S. Minaei, H. Kuntman, O. Cicekoglu, S. Turkoz and N. Tarim, "A new high output impedance current-mode universal filter with single input and three outputs using dual output CCII," *Proceedings of the 7th IEEE International Conference on Electronics, Circuits and Systems*, vol. 1, pp. 379-382, 2000.
- [5] W. Chumhua, Z. Yan, Z. Qiuqing and D. Sichun, "A new current mode SIMO-type universal biquad employing multi-output current conveyors (MOCCII)," *Radioengineering*, vol 18, no. 1, pp. 83-88, 2009.
- [6] C. Toumazou, F. J. Lidgley, and D. G. Haigh, "Analogue IC design: the current-mode approach," *Peter Peregrinus*, London, 1990.
- [7] D. R. Bhaskar, V. K. Sharma, M. Monis, and S. M. I. Rizvi, "New current-mode universal biquad filter," *Microelectronics Journal*, vol. 30, pp. 837-839, 1999.
- [8] K. C. Smith and A. Sedra, "The current conveyor-a new circuit building block," *IEEE Proc.* vol. 56, pp. 1368-1369, 1968.
- [9] A. Sedra and K. C. Smith, "A second-generation current conveyor and its applications," *IEEE Trans. Circuit Theory*, vol. 17, pp. 132-134, 1970.
- [10] A. Fabre, O. Saaid, F. Wiest, and C. Boucheron, "Current controllable bandpass filter based on translinear conveyors," *Electronics Letters*, vol. 31, pp. 1727-1728, 1995.
- [11] K. Ikeda and Y. Tomita, "Realization of current-mode biquadratic filter using CCII with current followers," *Electronics and Communications in Japan*, part 2, vol. 77, pp. 99-107, 1994.
- [12] A. M. Soliman, "New current-mode filters using current conveyors," *International Journal of Electronics and Communications (AEU)*, vol. 51, pp. 275-278, 1997.
- [13] S. Ozoguz, A. Toker, and C. Acar. "Current-mode continuous-time fully-integrated universal filter using CDBAs," *Electronics Letters*, vol. 35, pp. 97-98, 1999.
- [14] S. Maheshwari, and I.A. Khan, "Current-controlled current differencing buffered amplifier: implementation and applications," *Active and Passive Electronic Components*, vol. 27, pp. 219-227, 2004.
- [15] S. Kilinc, and U. Cam, "Current differencing buffered amplifier (CDBA) based current-mode filters," *Proceedings of the IEEE 12th Signal Processing and Communications Applications*, Cesme, Turkey, pp. 634-637, 2004.
- [16] A. Toker, S. Ozoguz, O. Cicekoglu, and C. Acar, "Current-mode all-pass filters using current differencing buffered amplifier and a new high-Q bandpass filter configuration," *IEEE Transactions on Circuits*

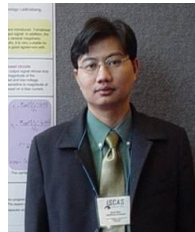
- and Systems II-Analog and Digital Signal Processing, vol. 47, pp. 949–954, 2000.
- [17] S. Ozoguz, A. Toker, and C. Acar, “Cascadable current mode multipurpose filters employing current differencing buffered amplifier (CDBA),” *International Journal of Electronics and Communications (AEU)*, vol. 56, pp. 67–72, 2000.
- [18] W. Jaikla, K. Sooksood, M. Siripruchyanun, “Current controlled CDBAs, (CCCDBAs)-based novel current-mode universal biquadratic filter,” *Proceedings of the 2006 IEEE International Symposium on Circuits and Systems (ISCAS 2006)*, Kos, Greece, pp. 3806–3809, 2006.
- [19] N. A. Shah and M. A. Malik, “Multifunction mixed-mode filter using FTFNs,” *Analog ICs and Signal Processing*, vol. 47, pp. 339–343, 2006.
- [20] J. WU and E. I. EL-Masry, “Universal voltage- and current-mode OTAs based biquads,” *International Journal of Electronics*, vol.85, pp. 553-560, 1998.
- [21] J D. R. Bhaskar, R. K. Sharma, A. K. Singh, and R. Senani, “New dual-mode Biquads Using OTAs,” *Frequenz*, vol. 60, pp. 246-252, 2006.
- [22] D. R. Bhaskar, A. K. Singh, R. K. Sharma and R. Senani, “New OTA-C universal current-mode/trans-admittance biquads,” *IEICE Electronics Express*, vol. 2, pp.8-13, 2005.
- [23] N. Pandey, S. K. Paul, A. Bhattacharyya and S. B. Jain, “A new mixed mode biquad using reduced number of active and passive elements,” *IEICE Electronics Express*, vol. 3, pp.115-121, 2006.
- [24] C. L. Hou, C. C. Huang, Y. S. Lan, J. J. Shaw and C. M. Chang, “Current-mode and voltage-mode universal biquads using a single current-feedback amplifier,” *International Journal of Electronics*, vol. 86, pp. 929-932, 1999.
- [25] N. A. Shah and M. A. Malik, “Voltage/current-mode universal filter using FTFN and CFA,” *Analog ICs and Signal Processing*, vol. 45, pp. 197-203, 2005.
- [26] S. T. Liu and J. L. Lee, “Insensitive current/voltage-mode filters using FTFNs,” *Electronics Letters*, vol. 32, pp.1079–1080, 1996.
- [27] N. A. Shah and M. A. Malik, “Multifunction mixed-mode filter using FTFNs,” *Analog ICs and Signal Processing*, vol. 47, pp. 339–343, 2006.
- [28] N. A. Shah S. Z. Iqbal and B. Parveen, “SITO high output impedance transadmittance filter using FTFNs,” *Analog ICs and Signal Processing*, vol. 40, pp. 87-89, 2004.
- [29] C. L. Hou and C. C. Lin, “A filter with three voltage-inputs and one voltage-output and one current-output using current Conveyors,” *Tamkang Journal of Science and Engineering*, vol. 7, pp. 145-148, 2004.
- [30] N. Pandey, S. K. Paul, A. Bhattacharyya and S. B. Jain, “A new mixed mode biquad using reduced number of active and passive elements,” *IEICE Electronics Express*, vol. 3, pp.115-121, 2006.
- [31] A. Toker, O. Cicekoglu, S. Ozoguz and H. Kuntman, “High output impedance transadmittance type continuous time multifunction filter with minimum active elements,” *International Journal of Electronics*, vol.88, pp. 1085-1091, 2001.
- [32] M. T. Abuelma'atti and A. Bentrchia, “A novel mixed-mode CCII-based filter,” *Active and Passive Electronic Components*, vol. 27, pp. 197-205, 2004.
- [33] M. T. Abuelma'atti, “A novel mixed-mode current-controlled current conveyor-based filter,” *Active and Passive Electronic Components*, vol. 26, pp. 185-191, 2003.
- [34] S. Lawanwisut, and M. Siripruchyanun, “Active-only electronically controllable current-mode multifunction biquadratic filter using CCCCTA,” *Electrical Engineering Conference 33*, vol. 2, pp. 1097-1100, 2010.
- [35] Y. Sun, and B. Jefferies, “Current-mode biquadratic filters using dual output current conveyors”, *IEEE Int. Conf. Electronics, Circuits and Systems*, vol. 3, pp. 135-138, 1998.
- [36] M. Kungern, P. Moungnoul, S. Junnapiya, and K. Dejhan, “Current-mode universal filter using translinear current conveyors”, *Int. Conf. Elect. Eng./Electr., Comp., Telecom., Inf. Tech.*, pp. 717-720, 2008.
- [37] Y. Maruyama, A. Hyogo, and K. Sekine, “A digitally programmable CMOS biquad filter using current-mode integrators,” *IEICE trans. on fundamentals*, vol. E85-A, no. 2, pp. 316-323, 2002
- [38] D.R. Frey, “Log-domain filtering: an approach to current-mode filtering,” *IEE Proceeding of Circuit Devices Systems*, vol. 140, pp. 406-416, 1993.



Somchai Srisakultiew received the B. Tech. Ed. in telecommunication engineering, and M.Tech electrical communication engineering degree in from King Mongkut's Institute of Technology Ladkrabang, Thailand in 1985 and 2002, B.Eng Master of Tech. Ed. in electrical technology from Rajamangala Institute of Technology Thunyaburi, Pha-thumthani in 2003. He has been with Computer Engineering, Faculty of Engineering and Architecture, Rajamangala University of Technology Isan, 744 Suranarai Rd. Nai-Maung, Maung, Nakhonratsima, 30000, Thailand since 1986. His research interests include electronic communications, analog signal processing and analog integrated circuit. He is a member of ECTI (Thailand).



Supawat Lawanwisut was born in Petchaburi, Thailand in 1975. He received the B. Tech. Ed. degree in electronic and computer and M. Tech. Ed. in electrical communication engineering from King Mongkut's Institute of Technology Ladkrabang, Thailand in 1996 and 2001, B. Eng. in electrical engineering from Thonburi University Thailand in 2011, respectively. He has been with department of Information and Communication Engineering, Faculty of Industrial Technology, Thepsatri Rajabhat University, Lopburi, Thailand since 2002. His research interests include electronic communications, analog signal processing and analog integrated circuit.



Montree Siripruchyanun received the B. Tech. Ed. degree in electrical engineering from King Mongkut's Institute of Technology North Bangkok (KMITNB), the M.Eng. and D. Eng. degree both in electrical engineering from King Mongkut's Institute of Technology Ladkrabang (KMILT), Bangkok, Thailand, in 1994, 2000 and 2004, respectively. He has been with Faculty of Technical Education, KMITNB since 1994. Presently, he is with Department of Teacher Training in Electrical Engineering as an Associate Professor, KMITNB. His research interests include analog-digital communications, analog signal processing and analog integrated circuit. He is a member of IEEE (USA), IEICE (Japan), and ECTI (Thailand).

Pulse Wave Velocity Measuring System using Virtual Instrumentation on Mobile Device

Răzvan A. Ciobotariu, Cristian Foşalău, Cristian Rotariu

Abstract — Virtual instrumentation is a concept that permits customizable modular software measurement and the development of the user-defined tools for control, process and visualization of data, creating versatile systems, using modular programming, intuitive and easy to use. In this paper we investigate a possibility of using virtual instrumentation in the development of two physiological parameters monitoring system, in order to assess a cardiovascular parameter, the Pulse Wave Velocity (PWV). We choose to monitor this parameter due to major incidence and impact of cardiovascular diseases (CVD).

Keywords—cardiovascular diseases, mobile devices, pulse wave velocity, patient monitoring, virtual instrumentation.

I. INTRODUCTION

VIRTUAL instrumentation is one of the major development resulted from the extensive use of computers, which offers the benefits of customizable software development of user-defined tools for control, process, and visualization of data, creating versatile systems, using modular programming, intuitive and easy to use. In this paper we present the development and implementation of virtual instrumentation software for medical application running on a mobile device.

According to recent studies and statistics, cardiovascular diseases (CVD) are among the most frequent cause of death. The total cost and the indirect mortality cost estimated for CVD are higher than for any other major diagnostic group [1].

Early diagnosis of CVD could prevent further

Manuscript received October 27, 2012. Manuscript accepted February 17, 2013. This work was realized with the support of POSDRU CUANTUMDOC “DOCTORAL STUDIES FOR EUROPEAN PERFORMANCES IN RESEARCH AND INOVATION” ID79407 project funded by the European Social Found and Romanian Government and the support of PERFORM-ERA “Postdoctoral Performance for Integration in the European Research Area” (ID-57649), financed by the European Social Fund and the Romanian Government.

R. A. Ciobotariu and C. Foşalău are with “Gheorghe Asachi” Technical University of Iasi, Faculty of Electrical Engineering, Dimitrie Mangeron, no. 51-53, 700050 IASI, ROMÂNIA (phone: +40-232-237627; e-mail: razvan.ciobotariu@yahoo.com).

C. Rotariu is with the “Gheorghe Asachi” Technical University of Iasi, Faculty of Automatic Control and Computer Engineering, Dimitrie Mangeron no. 27, 700050 ROMANIA, (phone: +40232231343; e-mail: cr.rotariu@yahoo.com).

complications, leading to improvement of patient’s quality of life and, for long term, can decrease the costs of the medical system. One step further to this goal is the long term monitoring of the patients, in their usual habitat and during daily activities, without restricting their freedom of movement.

The studies in the health area have shown the major influence that arterial stiffness has on appearance and evolving of atherosclerosis [2], [3], rheumatoid arthritis [4], complications due to high blood pressure, development of myocardium and coronary diseases, affection of vascular bed of several organs, such as brain or kidney [5]. One of the non-invasive techniques of assessing the arterial stiffness is the measurement of Pulse Transit Time (PTT) / Pulse Wave Velocity (PWV) [6]. PTT is a technique that measures the time needed for a blood pressure pulse wave to cross a known section of the arterial tree, and the PWV represents the ratio between the length of the measured arterial segment and the elapsed time from the ventricular ejection until the pulse pressure reaches the distal measurement site. The delay of the propagation is due to elasticity of the blood vessels walls [7]. During blood ejection from the left ventricle, the sudden rise of blood pressure is absorbed by the elastic walls of the aorta, a pulse wave propagates along the aorta, transmitting their energy to the aortic wall. The energy stored in the artery walls is released after the cardiac contraction has finished, helping to blood propagation.

The Moens-Kortweg model (eq. 1) [8] states that PWV depends on the elasticity of the blood vessel wall, its thickness and diameter, and the density of blood: the stiffer the artery, the faster a pressure pulse is propagated through it [9].

$$PWV = \frac{\text{distance}}{PTT} = \sqrt{\frac{Eh}{\rho 2r}} \quad (1)$$

E represents the Young’s module of the blood vessel, h is its thickness, ρ is the density of blood, and r is the radius of the blood vessel.

The major determinants of PWV are: age [3], – with age increases the stiffness of arterial walls by replacing the elastic fibers with collagen [10], hence, the pressure wave generated by left ventricle ejection travels along the arterial vascular tree more rapidly; blood pressure [11], [12] – high arterial

blood pressure is associated with an increased arterial stiffness, which generates an increase of systolic pressure and decrease of diastolic pressure [13]; gender; heart rate – because of frequency-dependant viscoelasticity of the arterial wall: increased heart rate leads to an increased arterial stiffness [14]; and sympathetic nervous system – sympathetic activation increases blood pressure, heart rate and smooth muscle cells tonus, hence, increases arterial stiffness [15].

II. MATERIALS AND METHOD

A. Hardware development of the system

There are many devices used for measuring the PTT and PWV, by different techniques, as example: measuring the pulse transit time from carotid to femoral artery [16], using pressure sensors; measuring the delay between the ECG R-wave and the arrival of the pulse at the radial artery [17], recorded by a brachial obtrusive cuff, or by performing ECG-gated Doppler measurements. The inconvenient of the methods described above is that a few of them can be performed ambulatory and without the presence of a well-trained operator [18].

Our system for measuring the PWV is based on recording the ECG and photoplethysmographic (PPG) signals. This technique uses the R-wave extracted from the ECG signal as the beginning of the ventricular contraction, which is the start moment of the pulse wave, which travels from the heart to distal regions. The arrival moment of the pulse wave to the index of the left hand is determined from the PPG signal (Fig. 1).

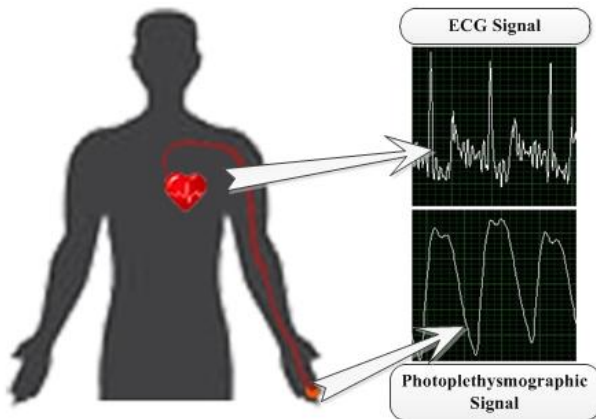


Fig. 1. Measurement sites of the ECG and PPG signals

The PWV was computed, as it is shown in equation (2), from the time difference between the starting point of the pulse wave and the moment when the pulse wave reaches the finger (Fig. 2).

By dividing the length of the blood vessel considered to the time measured from indexes difference, the PWV is determined.

$$PWV = \frac{\text{blood vessel length} * \text{sampling frequency}}{|\text{Index}(ECG) - \text{Index}(PPG)|} \quad (2)$$

The length of the blood vessel was measured using anatomical landmarks for determining the heart position, the aortic branch and brachial trunk.

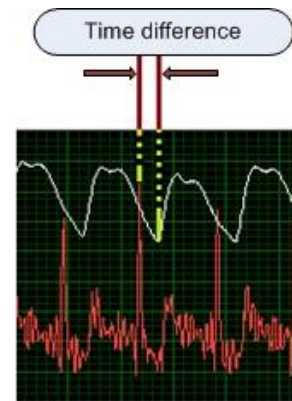


Fig. 2. Time difference between the ECG R-wave and the arrival moment of the pulse wave to the finger

The system was made using two ez430-RF2500 boards from Texas Instruments [19]. The ez430-RF2500 is an ultra-low power wireless development system that has an MSP430F2274 microcontroller with a 10 bits A/D converter, for gathering and converting the data from the analog modules, and a wireless transceiver CC2500 at 2.4GHz, working in ISM (industrial, scientific and medical) radio band, for data transmission. The ez430-RF2500 boards use for communication SimpliciTI [20], protocol developed by Texas Instruments and aimed at small RF ultra-low-power wireless sensor networks. The programming of the two ez430-RF2500 modules was done using the IAR Embedded Workbench for MSP430 [21].

One of the ez430-RF2500 modules was programmed to scan in the same cycle, both the ECG and PPG channels, at a frequency of 200 times per second, converting the signals from analog to digital.

The ECG module, made in our laboratory, is a low-power device, supplied from two AAA 1.5V batteries and detects one lead ECG signal by measuring the skin potentials using 3 electrodes placed on the skin surface.

Fig. 3 presents the electrical diagram of the ECG module. The circuit amplifies the signal and filters it, first high-pass, rejecting the oscillations due to respiration, after that it filters low-pass, for rejecting the muscular activity noise.

The PPG module, also made in our laboratory, is powered from four AAA 1.5V batteries, and uses a photodiode which emits light in IR domain. The IR fascicle is reflected by the finger skin, in accordance with the blood pulse wave which causes small oscillations of the light beam. A phototransistor detects these changes, causing a variation of its collector current. After that, a simple electronic circuit amplifies and filters the signal, creating the PPG wave. The electrical diagram is depicted in Fig. 4.

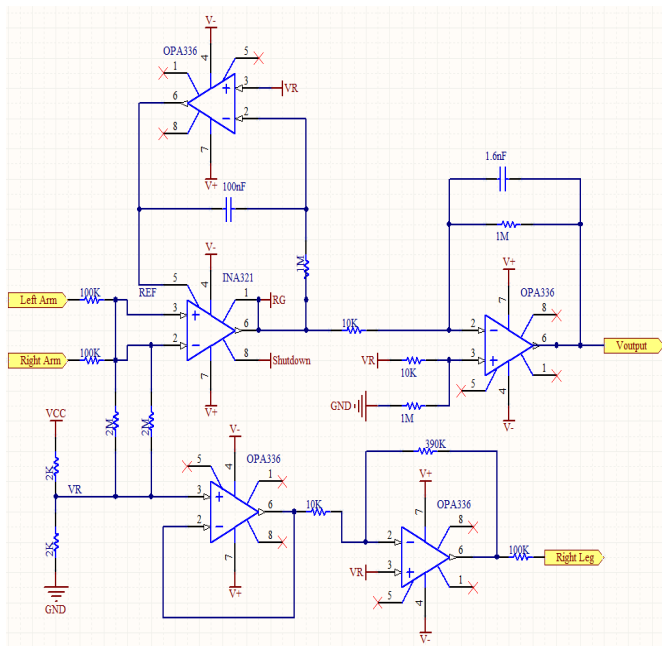


Fig. 3. ECG board schematic [22]

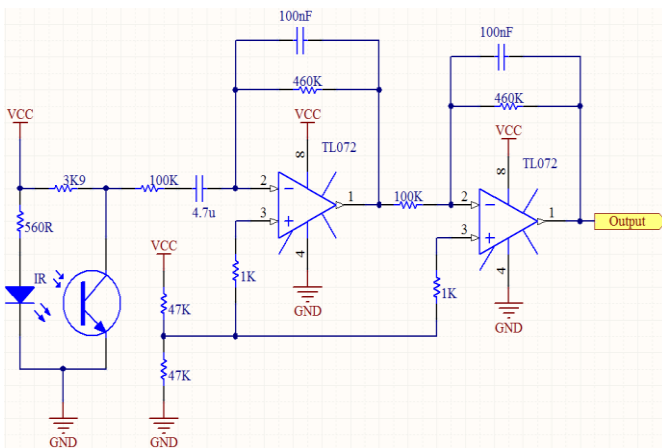


Fig. 4. PPG board schematic

After the A/D conversion, the ez430-RF2500 module packs the collected data and transmits them to the other ez430-RF2500 module, which works as receiver, for saving them on the mobile device. Fig. 5 presents the ECG and PPG modules connected to the ez430-RF2500 transmitter module.

As mobile device, we choose a HTC X7500 smartphone, which has an USB interface, for connecting the receiver module, and uses Windows Mobile 5 as operating system (Fig. 6).

B. Software development of the system

The software that runs on the mobile device was developed by using LabVIEW 2010 from National Instruments [23], a graphical system design which offers the tools needed to create and deploy measurement and control systems.

To accomplish the signal processing, we developed and tested algorithms using Matlab 2011a software [24] to find

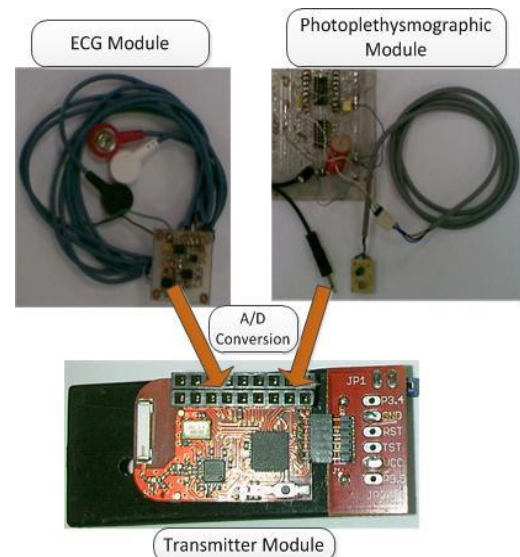


Fig. 5. ECG and PPG modules, connected to the transmitter module



Fig. 6. HTC X7500 smartphone

the ECG R wave-indexes, to determine the PPG-indexes and to compute the PWV. After that, we implemented the algorithms on LabVIEW Mobile.

The software for PWV computation, running on the smartphone as virtual instrument, is represented in the Fig 7.

The software unpacks the data as two separate signals and processes them separately.

For determining the ECG R-indexes and PPG-indexes, the algorithm uses a 500 points moving window.

First, the ECG signal is processed to determine the R-waves and to extract the corresponding sample index. Because we were interested only on detection of the R-waves, which are the most prominent wave from ECG and the signal has a good signal to noise ratio, no additional filtration was necessary.

III. RESULTS

The constant used to compute the threshold was experimentally determined, and has the value around 0.5.

The algorithm calculates the ECG threshold for each window, as follow in (3):

$$\text{Threshold} = \text{mean}(\text{ECG}) + 0.5 \times [\text{max}(\text{ECG}) - \text{mean}(\text{ECG})] \quad (3)$$

Using the equation (3), the algorithm finds the points that exceed the threshold and, in a 10 points window, it searches the maximum value, representing the maximum ECG R-wave point for that QRS complex. Finally, the window is moved and the whole process is restarted.

Fig. 8 presents in the top window, the found indexes on the ECG signal.

For finding the arrival moment of the pulse wave to the finger, the software follows the next steps:

Considering the ECG R-index previously determined to be the starting point for scanning the PPG signal, the software uses a 40 points moving window, in which searches the lowest signal value, considered to be the moment at which the pulse wave reaches the finger, and stores the value of that point and its index (Fig. 8. in bottom window).

The next step is to differentiate the indexes from the ECG R-wave and PPG and, multiplying the result with the sampling frequency, it is obtained the time passed from the start moment of the pulse wave until it reaches the finger (see (2)).

The final step on measuring the velocity of the pulse wave is to divide the knowing length of the arterial segment, to the time previously found (see (2)).

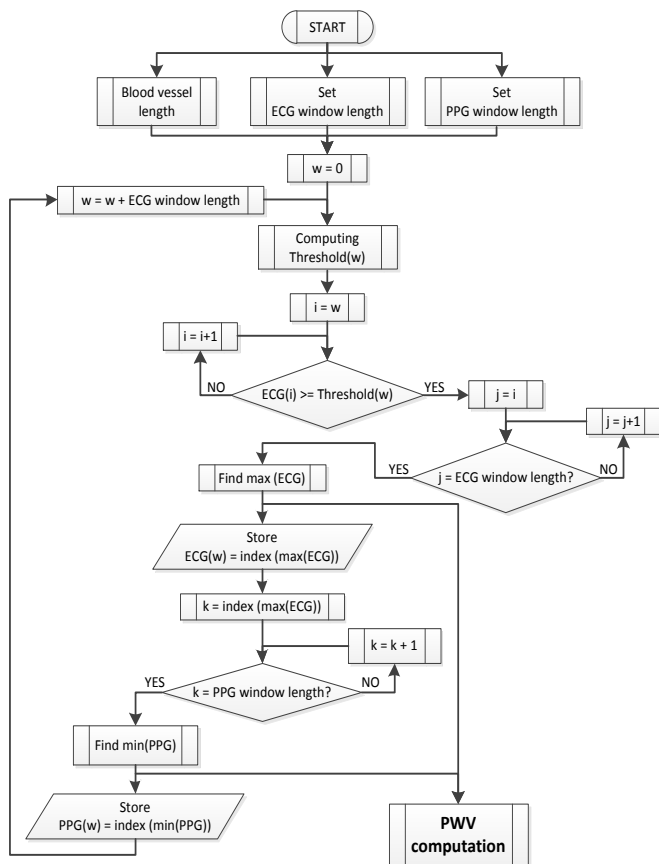


Fig. 7. Flowchart of the software running on LabVIEW for PWV computation

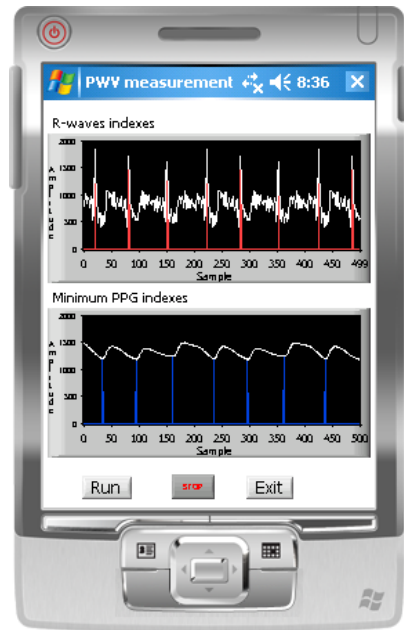


Fig. 8. LabVIEW interface for mobile device, displaying the ECG R and PPG indexes (screen shot on LabVIEW Windows Mobile 5 Pocket PC emulator)

After finding the values of PWV, the software creates a file and stores the data on the device.

The chart depicted in Fig. 9 represents the variation in time of the PWV recorded from a patient. The subject was resting and relaxing for a 15-20 minutes period of time and the PWV was recorded.

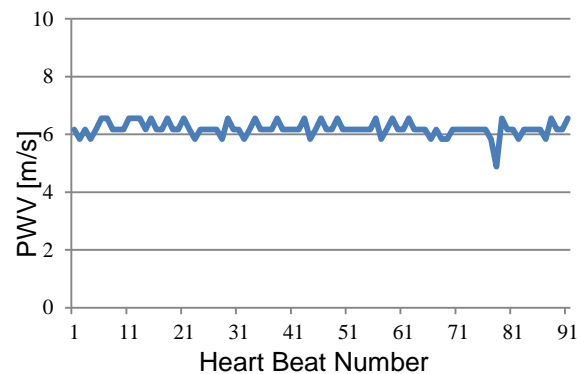


Fig. 9. PWV recorded while the subject was resting

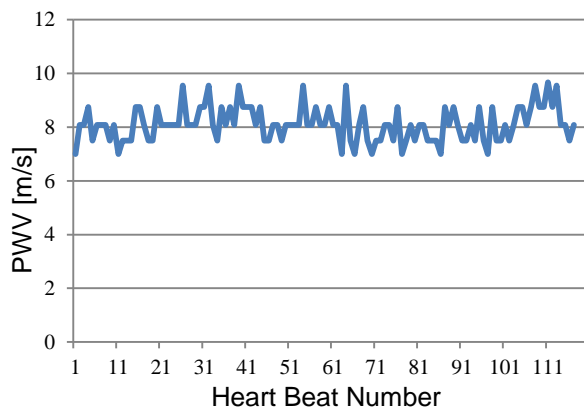


Fig. 10. PWV recorded after the subject had some physical effort

The chart in Fig. 10 presents the variation in time of the PWV recorded from a subject after he had some physical effort, he rapidly climbed stairs for 10 minutes.

IV. CONCLUSIONS

We choose to create a mobile medical device that perform long term PWV measurements, because this is an important parameter in determining the cardiovascular health or the response to some drugs administration, and we wanted to show the use of virtual instrumentation for developing devices with medical applications. Virtual instrumentation has the advantage of versatility, and due to graphical modular programming it is easy to learn and use, even by the untrained users.

In terms of medical applications and patient's welfare, we implemented the software on a mobile device, creating a tool for long term monitoring of patients at home, in their daily living and usual activities, which gives the freedom of movement, improving their quality of life. The mobile devices, such as PDA or smartphones, have the possibility to transmit data through GSM/GPRS or WiFi to the remote units, for the storage and further analysis. This represents one step forward in e-health and telemedicine.

ACKNOWLEDGEMENT

This work was realized with the support of POSDRU CUANTUMDOC "DOCTORAL STUDIES FOR EUROPEAN PERFORMANCES IN RESEARCH AND INNOVATION" ID79407 project funded by the European Social Fund and Romanian Government and the support of PERFORM-ERA "Postdoctoral Performance for Integration in the European Research Area" (ID-57649), financed by the European Social Fund and the Romanian Government.

REFERENCES

- [1] <http://circ.ahajournals.org/content/123/4/e18.full.pdf>
- [2] <http://www.escardio.org/guidelines-surveys/esc-guidelines/GuidelinesDocuments/guidelines-AH-FT.pdf>
- [3] Hertzner N R 1991 The natural history of peripheral vascular disease. Implications for its management *Circulation* **83** (2 suppl.) I12-9
- [4] "Arterial stiffness and central blood pressure, as determined by pulse wave analysis, in rheumatoid arthritis" R Klocke, J R Cockcroft, G J Taylor, I R Hall, D R Blake
- [5] O'Rourke M.F., Safar M.E., "Relationship between aortic stiffening and microvascular disease in brain and kidney: cause and logic of therapy", *Hypertension* 46, 2005;
- [6] Asmar R., "Arterial Stiffness and Pulse Wave Velocity. Clinical Applications", *Elsevier*, 1999;
- [7] Pan Yi-Shan, Jia Xiao-Bo, Cui Chang-Kui, Xiao Xiao-Chun, Analyse of Pulse Wave of Pulse Wave Propagation in Arteries , *Applied Mathematics and Mechanics (English Edition)*, 2006, 27(2):255-262.
- [8] The Moens-Kortweg [x] model = Bramwell J. C. & Hill A. V., "The Velocity of the Pulse Wave in Man", *Proc. Royal Society for experim. Biology & Med.*, Vol. 93, pp. 298-306, London, 1922
- [9] Nichols W. W., Denardo S. J., Wilkinson I. B., McEniery C. M., Cockcroft J., O'Rourke M.F., "Effects of Arterial Stiffness, Pulse Wave Velocity, and Wave Reflections on the Central Aortic Pressure Waveform", *J Clin Hypoertens*, 2008;
- [10] Astrand H., Stalhand J., Karlsson J., Karlsson M., Sonesson B., Lanne T., "In vivo estimation of the contribution of elastin and collagen to the mechanical properties in the human abdominal aorta: effect of age and sex" *J Appl Physiol* 2011;
- [11] B. Gribbin, A. Steptoe and P. Sleight, "Pulse Wave Velocity as a Measure of Blood Pressure Change", *Psychophysiology*, Vol.13, No.1, pp. 86-90, 1976.
- [12] A. Steptoe, H. Smuylan and B. Gribbin, "Pulse Wave Velocity and Blood Pressure Change: Calibration and Applications", *Psychophysiology*, Vol.13, No.5, pp. 488-493, 1976.
- [13] Asmar R., Beneros A., Topouchian J., Laurent P., Pannier B., Brisac A., Target R., Levy B., "Assessment of Arterial Distensibility by Automatic Pulse Wave Velocity Measurement", *Hypertension*, 1995;
- [14] Benetos A., Adamopoulos C., Bureau J. M., et al. "Determinants of accelerated progression of arterial stiffness in normotensive subjects and in treated hypertensive subjects over a 6-year period", *Circulation* 105, 2002;
- [15] Boutouyrie P., Lacolley P., Girerd X., Beck L., Safar M., Laurent S., "Sympathetic activation decreases medium-sized arterial compliance in humans" *Am J Physiol*, 267, 1994;
- [16] Determination of age-related increases in large artery stiffness by digital pulse contour analysis S. C. MILLASSEAU, R. P. KELLY, J. M. RITTER and P. J. CHOWIENCZYK
- [17] Non-Invasive Cuff-Less Measurements of the Arterial Blood Pressure: What does Pulse-Transit-Time tell us all about ? X. L. Aubert, J. Muehlsteff.
- [18] Domenico Campolo, "New Developments in Biomedical Engineering", ISBN 978-953-7619-57-2, *InTech* 2010
- [19] <http://www.ti.com/tool/ez430-rf2500>
- [20] <http://www.ti.com/corp/docs/landing/simpliciTI/>
- [21] <http://www.iar.com/en/Products/IAR-Embedded-Workbench/TI-MSP430/>
- [22] www.ti.com/lit/ds/symlink/ina321.pdf
- [23] <http://www.ni.com/labview/>
- [24] <http://www.mathworks.com/>

FIR Filter Implementation Based on the RNS with Diminished-1 Encoded Channel

Dragana Živaljević, Negovan Stamenković, and Vidosav Stojanović

Abstract—The nonrecursive digital filters implementation based on the RNS arithmetic is presented in this paper. In this implementation popular moduli set $\{2^n - 1, 2^n, 2^n + 1\}$ with diminished-one (diminished-1) $2^n + 1$ encoded channel is used. The diminished-one number system is used to avoid $(n + 1)$ -bit circuits in $(2^n + 1)$ -bit channel. Thus, in proposed approach all operand have n -bit length. The proposed RNS architecture of the filter consists of three main blocks: forward and reverse converter and arithmetic processor for each channel, where binary operations perform. Architecture for residue to binary (reverse) converter with diminished-1 encoded channel and architecture for modulo multiplication have been proposed. Besides, for all RNS channels, the systolic design is used for the efficient realization of FIR filter. A numerical example illustrates the principles of diminished-1 residue arithmetic, signal processing, and decoding for FIR filters.

Keywords—Chinese remainder theorem, diminished-one, FIR filters, residue number system, reverse converter.

I. INTRODUCTION

In many digital signal processing systems, finite impulse response (FIR) digital filters are frequently used because of their stability and linear phase property. On other hand, they are not suitable for recent applications demanding real-time performance and low power consumption. The demand for real-time digital signal processing with respect to power consumption has forced the researchers to look for efficient arithmetic algorithms, which can implement high speed digital signal processor units. The systems based on Residue Number System (RNS) have become the most popular as they take advantage of all the benefits given by the parallelism and the carry free computations.

Filter realizations using Residue Number System (RNS) have been investigated in literature [1][2][3][4]. RNS is suitable for implementation of high-speed digital signal processing due to their inherent parallelism, modularity, fault toleration and local carry propagation properties. Arithmetic operations like multiplication and addition can be carried out more efficiently as RNS ensures localized carry propagation properties. RNS is particularly suitable for implementing FIR filters where multiplications and additions are the core operations. These features make RNS beneficial for digital signal processing applications, particularly, when large word length and high throughput rate are required.

D. Zivaljević, N. Stamenković and V. Stojanović are with University of Niš, Faculty of Electronic Engineering, A. Medvedeva 14, 18000 Niš, Serbia, e-mails: dragana.zivaljevic@elfak.ni.ac.rs; negovanstamenkovic@gmail.com; vidosav.stojanovic@elfak.ni.ac.rs.

Manuscript received February 27, 2012.

doi: 10.11601/ijates.v2i2.32

The selection of the moduli set plays a critical role in the improvement of the performance of RNS FIR filters [5]. The moduli set $\{2^n - 1, 2^n, 2^n + 1\}$ is used to design RNS FIR filters in this paper for the following reasons: firstly, it provides simpler design for converters; secondly, we can utilize the dedicated hardware multipliers on FPGA platforms to implement multiplications with acceptable cost for normally encoded RNS channel; thirdly, since it is the most commonly used one in previous works, using this moduli set makes our work applicable to the most existing designs.

The diminished-1 representation of binary numbers was introduced in [6] to speed up the modulo $(2^n + 1)$ arithmetic operations. Since only n bits are required for the representation of any digit in RNS, the diminished-1 representation can lead to implementations with delay and area that approach to delays and areas of the modulo $(2^n - 1)$ and 2^n representations. A lot of papers on the design of modulo $(2^n - 1)$ adders and multipliers for diminished-1 operands have already been published [7], [8], [9], [10]. However, special treatment is required for operands equal to zero. Since this can lead to implementations with increased area and delay complexity, the efficient integration of zero handling into modulo $(2^n + 1)$ arithmetic units is an open problem.

An RNS-based architecture of the filter consists of three main blocks. As first, all operands are converted into their corresponding sets of residues with binary-to-residue (forward) converters, according to the specified moduli set. Then, the arithmetic processing is performed in parallel in each channel following the corresponding modulo arithmetic. Finally, the RNS representation of the results is converted back to binary with residue-to-binary (reverse) converters.

Forward converters for RNS with diminished-1 encoded channel are proposed in [11], while modulo $(2^n + 1)$ adder architectures for diminished-1 operands with integrated zero handling are proposed in [12], and modulo $(2^n + 1)$ multipliers for diminished-1 operands including zero indication bits are proposed in [13].

This paper proposes a new approach to FIR filters design based on the RNS with diminished-1 encoded channel and also architecture for the reverse converter for RNS with diminished-1 encoded channel.

Organization of the paper is as follows; after recalling the diminished-1 arithmetic in Section II, the architecture of N -th order recursive digital filter is presented in Section III.

II. DIMINISHED-1 ARITHMETIC

To represent all integers in RNS using modulo $(2^n + 1)$, $(n + 1)$ bits are required. The additional bit is required in order

to represent the number $2^n = \langle -1 \rangle_{2^n+1}$. To overcome the problem of performing binary arithmetic with this additional bit, a modified binary number system is used in order to avoid additions and multiplications involving the additional bit. This allows the additional bit to be only 1 when the number to be represented is 0, which can be achieved by subtracting 1 from the normal binary number.

The normal representation and this diminished-1 representation are indicated in the Table I for $n = 4$. When performing

TABLE I
CORRESPONDENCE BETWEEN NORMAL, BINARY AND DIMINISHED-1 REPRESENTATIONS

Normal	Binary	Diminished-1
0	0000	1
1	0001	2
2	0010	3
3	0011	4
4	0100	5
5	0101	6
6	0110	7
7	0111	8
8	1000	9 (-8)
9 (-8)	1001	10 (-7)
10 (-7)	1010	11 (-6)
11 (-6)	1011	12 (-5)
12 (-5)	1100	13 (-4)
13 (-4)	1101	14 (-3)
14 (-3)	1110	15 (-2)
15 (-2)	1111	16 (-1)
16 (-1)	10000	0

arithmetic for mod $(2^n + 1)$ using diminished-1 system, all input operands and the corresponding results are expressed in diminished-1 form. Let x' be diminished-1 representation of normal binary number $x \in [0, 2^n]$, namely

$$x' = \langle x - 1 \rangle_{2^n+1}. \quad (1)$$

In (1), when $x \neq 0$, $x' \in [0, 2^n - 1]$ is an n -bit number, therefore $(n + 1)$ -bit circuits can be avoided in this case. However, when $x = 0$, $x' = 2^n$ is an $(n + 1)$ -bit number. This leads to special treatment for $x' = 0$. According to this representation a number x' is represented as $x'_n X'$, where x'_n is the zero indication bit and $X' = x'_{n-1} x'_{n-2} \dots x'_0$ is the magnitude representation [12].

A. Binary to diminished-1 RNS convertor

With the diminished-1 encoded channel, a very efficient binary to diminished-1 RNS converter is proposed for the $\{2^n - 1, 2^n, 2^n + 1\}$ moduli set [11]. An $3n$ -bits integer $X \xrightarrow{RNS} (x_1, x_2, x'_3)$ in the dynamic range is represented as

$$X = \sum_{i=0}^{3n-1} X_i 2^i = N_2 2^{2n} + N_1 2^n + N_0. \quad (2)$$

As explained above, the diminished-1 representation uses the modulo of $X - 1$ instead of X . Computation of the value x'_3 for this representation, with an identical approach as in standard $(2^n + 1)$ channel, is performed as:

$$x'_3 = \langle X - 1 \rangle_{2^n+1} = \langle 1 + N_2 + \overline{N}_1 + N_0 \rangle_{2^n+1}. \quad (3)$$

Only one CSA (carry save adder) and one full modulo $(2^n + 1)$ adder are required for the diminished-1 modulo $(2^n + 1)$ RNS converter [11].

B. Diminished-1 modulo $(2^n + 1)$ addition

Ordinary addition in diminished-1 number system is performed as follows [14]:

$$S' = \langle x' + y' + 1 \rangle_{2^n+1}. \quad (4)$$

Modulo $(2^n + 1)$ addition can be realized by an end-around-carry adder, where the carry-out is inverted and fed back into the carry-in, i.e. $c_{in} = \overline{c}_{out}$. This can be achieved with two adders to prevent a combinational loop. The carry-out inversion logic does not work when both summands are equal to zero. Therefore an additional AND gate has to be added as the control input for a multiplexer, which selects the correct output $x' + y' = 2^n$, when $x' = y' = 2^n$ [15].

Diminished-1 modulo $(2^n + 1)$ addition is now defined by:

$$\langle x' + y' + 1 \rangle_{2^n+1} = \begin{cases} 2^n & \text{if } x = 2^n \wedge y = 2^n \\ \langle x' + y' \rangle_{2^n+1} + 1 & \text{otherwise} \end{cases} \quad (5)$$

J.-L. Beuchat propose an alternative definition for modulo $(2^n + 1)$ addition [16]. Let us define the $(n + 2)$ -bit integer $S = s_{n+1} s_n \dots s_0 = x' + y'$. The modulo $(2^n + 1)$ addition can be expressed as:

$$\langle x' + y' + 1 \rangle_{2^n+1} = \langle x' + y' \rangle_{2^n+1} + s_{n+1} 2^n + \overline{s_{n+1} \vee s_n}. \quad (6)$$

Figure 1 depicts the resulting hardware operator which requires carry-propagate adder, a NOR gate and incrementer [16].

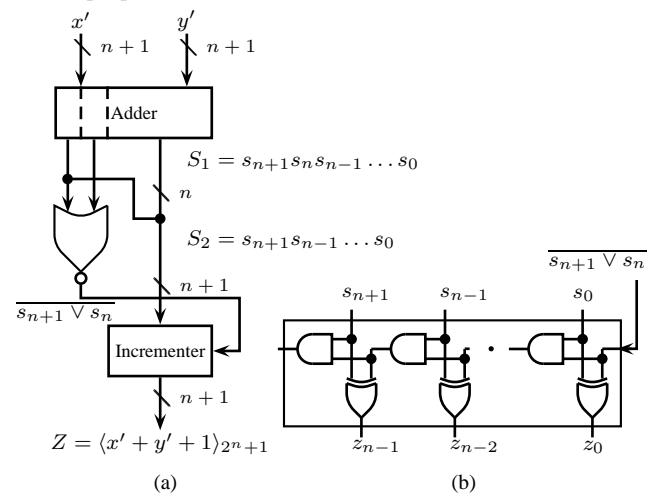


Fig. 1. The architecture of the modulo $(2^n + 1)$ adders for diminished-1 encoded channel (a). Carry propagation increment stage (b).

Efficient parallel VLSI diminished-1 structures for modulo $(2^n + 1)$ two-operand addition have also been proposed recently [9].

Validity of the above diminished-1 addition of two $(n + 1)$ bit numbers, is demonstrated on following example.

Let $x' = 16$ and $y' = 10$. Then

$$\begin{array}{r|l} x' = & 10000 \\ y' = & 01010 \\ \hline S_1 = & 011010 \end{array} \quad \begin{array}{r|l} S_2 = & 01010 \\ \hline S_{n+1} \vee s_n = & 0 \\ \hline S' = x' + y' + 1 & 01010 \end{array}$$

Thus, $S' = 10$, which can be verified to be true¹.

C. Diminished-1 modulo $(2^n + 1)$ multiplication

The diminished-1 multiplication is defined as [17], [14]:

$$Q' = \langle \langle x' \times y' \rangle_{2^n+1} + x' + y' \rangle_{2^n+1}. \quad (7)$$

The modulo $(2^n + 1)$ multiplication algorithm can be easily adapted for the diminished-1 number representation of input operands and output product. Thereby, the two additional terms x' and y' have to be added in the modulo carry save adder, resulting in small increasing of area and delay. The special case of $x'y' = 0$ has to be treated separately and the constant correction term be adapted.

The architecture of diminished-1 modulo $(2^n + 1)$ multiplication is presented in [17]. If the input residues are $(n + 1)$ bits wide, the partial products for modulo $2^n + 1$ multiple are arranged as n bits wide vectors. The partial product generation for inputs of 5 bits width is shown in Table II. Obviously, 4 bits $x_3x_2x_1x_0$ are required for the representation nonzero diminished-1 binary numbers. In this multiplication, the bits

TABLE II
PARTIAL PRODUCT GENERATION MOD $2^4 + 1$

2^6	2^5	2^4	2^3	2^2	2^1	2^0	
			$x'_0y'_3$	$x'_0y'_2$	$x'_0y'_1$	$x'_0y'_0$	$= pp_0$
		$x'_1y'_3$	$x'_1y'_2$	$x'_1y'_1$	$x'_1y'_0$	$x'_1y'_3$	$= pp_1$
	$x'_2y'_3$	$x'_2y'_2$	$x'_2y'_1$	$x'_2y'_0$	$x'_2y'_3$	$x'_2y'_2$	$= pp_2$
$x'_3y'_3$	$x'_3y'_2$	$x'_3y'_1$	$x'_3y'_0$	$x'_3y'_3$	$x'_3y'_2$	$x'_3y'_1$	$= pp_3$
			x_3	x_2	x_1	x_0	$= x'$
			y_3	y_2	y_1	y_0	$= y'$
			0	0	0	0	$= COR$

with weight greater than 2^3 , which are to the left of the straight line, are complemented and repositioned to the right of the line.

The architecture of proposed modulo $2^n + 1$ multiplier for diminished-1 encoded channel is shown in Figure 2. Assuming the coefficient word length of 4-bits and input sample word length of 4-bits, in Fig. 2 is shown the hierarchical decomposition of Wallace tree logic. The partial sum are added by using five carry-save-adders (CSA) and modulo 17 adder which is realized as carry-propagate-adder with end-around-carry. Partial product is generated in parallel.

The principle of the proposed memoryless-based implementation of partial product generator is shown in Fig 3. It consists of n 2-to-1 multiplexers, where n is the input sample word length. The partial product is generated by connecting zero and coefficient value to the MUX data inputs, input data bits to the select input, and circular shifting of the MUX output $s - 1$ bits to the left, for $1 \leq s \leq n$. After circular shifting, $s - 1$ LSB bits are used as complement.

An implementation of the modulo 17 partial product generator for pp_2 is shown in Figure 4. The small circles above the register represent a complement of the input bit.

¹ $S' = (16 + 10)_{17} + 1 = 10$

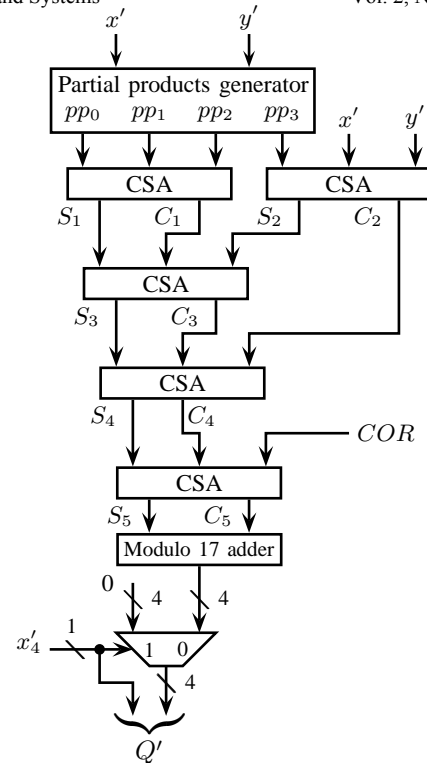


Fig. 2. Architecture of modulo $2^n + 1$ multiplier for diminished-1 encoded channel

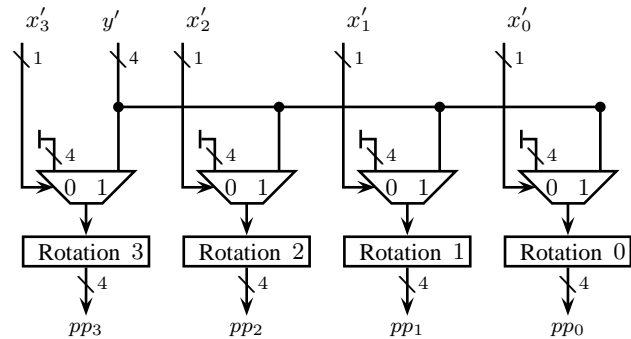


Fig. 3. Partial products generator.

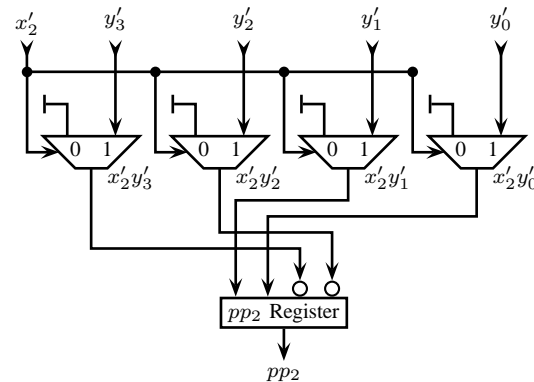


Fig. 4. Partial product pp_2 generator.

Validity of the above diminished-1 multiplication of two 4 bit numbers is demonstrated on following example. Let $x' = 9$ and $y' = 10$. Then

1010×1001					
pp_0	=	1	0	1	0
pp_1	=	0	0	0	1
pp_2	=	0	0	1	1
pp_3	=	0	0	1	0
x'	=	1	0	1	0
y'	=	1	0	0	1
COR	=	0	0	0	0

The first carry-save-adder

pp_0	=	1	0	1	0
pp_1	=	0	0	0	1
pp_2	=	0	0	1	1
S_1	=	1	0	0	0
C_1	=	0	0	1	1

The second carry-save-adder

pp_3	=	0	0	1	0
x'	=	1	0	1	0
y'	=	1	0	0	1
S_2	=	0	0	0	1
C_2	=	1	0	1	0

The third carry-save-adder

S_1	=	1	0	0	0
C_1	=	0	1	1	1
S_2	=	0	0	0	1
S_3	=	1	1	1	0
C_3	=	0	0	0	1

The fourth carry-save-adder

S_3	=	1	1	1	0
C_3	=	0	0	1	1
C_2	=	0	1	0	0
S_4	=	1	0	0	1
C_4	=	0	1	1	0

The fifth carry-save-adder contains only half-adders since $COR = 0000$.

S_4	=	1	0	0	1
C_4	=	1	1	0	1
S_5	=	0	1	0	0
C_5	=	1	0	0	1

Finally

S_5	=	0	1	0	0
C_5	=	0	0	1	0
Q'	=	0	1	1	1

Thus $Q' = 7$, which can be verified to be true: $Q' = \langle \langle 9 \times 10 \rangle_{17} + 9 + 10 \rangle_{17} = 7$.

D. RNS to binary conversion

Consider the well-known 3-moduli set $\{m_1 = 2^n, m_2 = 2^n - 1, m_3 = 2^n + 1\}$ which has a dynamic range approximately equal to $3n$ bits. Wang, Jullien and Miller [18] show that the decoded binary number is obtained as

$$X = Y 2^n + x_1, \quad (8)$$

where

$$Y = \langle (-2^{2n-1} + 2^{n-1})x_3 + (2^{2n-1} + 2^{n-1})x_2 - 2^n x_1 \rangle_{2^{2n-1}} \quad (9)$$

This operation does not need any computation because equation (8) amounts to concatenation of Y obtained in (9) with x_1 as LSBs.

Residue number x_3 is encoded in diminished-1 as $x_3 = x'_3 + 1$. Now let

$$A = \langle -2^n x_1 \rangle_{2^{2n-1}}, \quad (10)$$

$$B = \langle (2^{2n-1} + 2^{n-1})x_2 \rangle_{2^{2n-1}}, \quad (11)$$

$$C = \langle (-2^{2n-1} + 2^{n-1})(x'_3 + 1) \rangle_{2^{2n-1}}. \quad (12)$$

To evaluate A , B and C , the following property is used: modulo $(2^s - 1)$ multiplication of a residue number by 2^t , where s and t are positive integers, is equivalent to t bit circular left shifting.

Assuming that x_1 is expressed in $2n$ bits, where n the most significant bits are zeros

$$x_1 = \underbrace{00 \dots 0}_n \underbrace{x_{1,n-1}x_{1,n-2} \dots x_{1,0}}_n \quad (13)$$

and

$$A = \underbrace{\bar{x}_{1,n-1}\bar{x}_{1,n-2} \dots \bar{x}_{1,0}}_n \underbrace{11 \dots 1}_n \quad (14)$$

where negative value of a number of modulo $(2^{2n} - 1)$ is the one's complement of that number.

Assuming that $2n$ bit expression of x_2 is given by:

$$x_2 = \underbrace{00 \dots 0}_n \underbrace{x_{2,n-1}x_{2,n-2} \dots x_{2,0}}_n \quad (15)$$

it follows that

$$\begin{aligned} B &= x_{2,0} \underbrace{0 \dots 0}_n \underbrace{x_{2,n-1} \dots x_{2,1}}_{n-1} + 0 \underbrace{x_{2,n-1} \dots x_{2,0}}_n \underbrace{00 \dots 0}_{n-1} \\ &= x_{2,0} \underbrace{x_{2,n-1} \dots x_{2,0}}_n \underbrace{x_{2,n-1} \dots x_{2,1}}_{n-1}. \end{aligned} \quad (16)$$

The value of C , as given in (12), is:

$$C = \langle (-2^{2n-1} + 2^{n-1})x'_3 \rangle_{2^{2n-1}} - K \quad (17)$$

where

$$K = 2^{2n-1} - 2^{n-1} = \underbrace{01 \dots 10}_{n-1} \dots 0. \quad (18)$$

Let the $(n + 1)$ bit expression of x'_3 is given by:

$$x'_3 = x'_{3n} \underbrace{x'_{3,n-1}x'_{3,n-2} \dots x'_{3,0}}_n \quad (19)$$

or

$$x'_3 = 2^n x'_{3n} + X'_3. \quad (20)$$

Therefore, parameter C given in (17) can be evaluated as follows: Substituting (20) into (17) and applying the above-mentioned property, it follows that

$$\begin{aligned}
& \langle (-2^{2n-1} + 2^{n-1})X'_3 \rangle_{2^{2n-1}} \\
&= \langle - \underbrace{(x'_{3,0} \underbrace{0 \dots 0}_n x'_{3,n-1} \dots x'_{3,1})}_{n-1} \\
&\quad + 0 \underbrace{x'_{3,n-1} \dots x'_{3,0}}_n \underbrace{0 \dots 0}_{n-1} \rangle_{2^{2n-1}} \\
&= \langle (\overline{x'_{3,0}} \underbrace{x'_{3,n-1} \dots x'_{3,0}}_n \overline{x'_{3,n-1} \dots x'_{3,1}})_{n-1} \\
&\quad + 0 \underbrace{1 \dots 1}_n \underbrace{0 \dots 0}_{n-1} \rangle_{2^{2n-1}} \\
&= \langle (\overline{x'_{3,0}} \underbrace{x'_{3,n-1} \dots x'_{3,0}}_n \overline{x'_{3,n-1} \dots x'_{3,1}}) + K \rangle_{2^{2n-1}}
\end{aligned} \quad (21)$$

and

$$\langle (-2^{2n-1} + 2^{n-1})2^n x'_{3n} \rangle_{2^{2n-1}} = 0 \underbrace{x'_{3n} \dots x'_{3n}}_n \underbrace{0 \dots 0}_{n-1}. \quad (22)$$

Adding (21), (22) and subtracting (18), it is obtained

$$\begin{aligned}
C &= \underbrace{x'_{3,0} x'_{3,n-1} \dots x'_{3,0} \overline{x'_{3,n-1} \dots x'_{3,1}}}_n + 0 \underbrace{x'_{3n} \dots x'_{3n}}_n \underbrace{0 \dots 0}_{n-1} \\
&= \underbrace{x'_{3,0} x_{or,n-1} \dots x_{or,0} \overline{x'_{3,n-1} \dots x'_{3,1}}}_n,
\end{aligned} \quad (23)$$

where $x_{or,i} = x'_{3,i} \vee x'_{3n}$, for $0 \leq i \leq n-1$ (\vee denotes a logic OR operation). Note that $x_{3,i}$ and x_{3n} , can never be 1 at the same time.

To implement the modulo addition of three $2n$ -bit numbers (A , B and C) efficiently, we may use $2n$ full-adders as carry-save-adders (CSA) to convert three $2n$ bit numbers into two. The carry-out from the most significant bit (c_{2n}) is fed to the least significant bit position (c_0). Then fast $2n$ -bit carry-propagate-adder (CPA) with end-around-carry (EAC), is used to perform the modulo addition of two numbers to obtain the final result. The architecture is shown in Fig. 5.

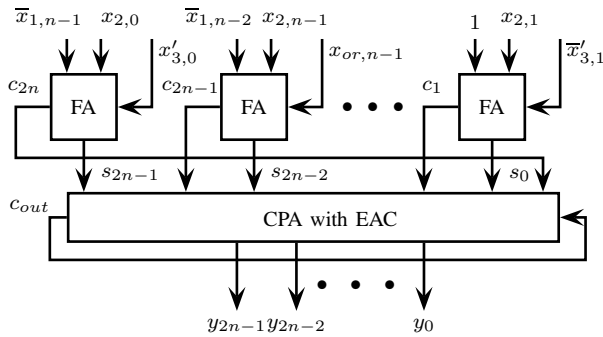


Fig. 5. The implementation of modulo $(2^{2n} - 1)$ addition of three $2n$ -bit numbers A , B and C .

E. An example

Consider the moduli set $\{16, 15, 17\}$ which is a special case of the moduli set $\{2^n, 2^n - 1, 2^n + 1\}$ for $n = 4$. To convert the

RNS number $X = (12, 3, 9)$ into its corresponding weighted binary representation, we have

$$\begin{array}{l|l}
x_1 = 12 & 1100 \\
x_2 = 3 & 0011 \\
x'_3 = 9 - 1 = 8 & 01000
\end{array}$$

Based on (14), (16) and (23), Y can be computed as

$$\begin{array}{r}
A = \quad 0011 \ 1111 \\
B = \quad 1001 \ 1001 \\
C = \quad 1100 \ 0011 \quad + \\
\hline
\text{Sum vector} = \quad 0110 \ 0101 \quad s_{2n-1} s_{2n-2} \dots s_0 \\
\text{Carry vector} = \quad \boxed{1} | 0011 \ 011 \quad c_{2n} c_{2n-1} \dots c_1 \\
\hline
c_{out} = \quad \boxed{0} | 1001 \ 1100 \\
\hline
\text{Correct Result: } Y = \quad 1001 \ 1100
\end{array}$$

Finally, based on the equation (8), the final weighted binary number, X , can be simply calculated as

$$X = Y 2^4 + x_1 = 1001 \ 1100 \ 1100 = 2508.$$

Thus, $X = 2508$, which can be verified to be true.

III. ARCHITECTURE OF THE FILTER

Difference equations for each channel of FIR filter, implemented as RNS, can be defined as:

$$y_j(n) = \left\langle \sum_{i=0}^{N-1} \langle b_{i,j} x_j(n-i) \rangle_{m_j} \right\rangle_{m_j}, \quad \text{for } j = 1, 2, 3 \quad (24)$$

where $x_j(n)$ and $y_j(n)$ are the residue representations of the input and the output signals of the filter modulo m_j , respectively, and $b_{i,j}$, $i = 0, 1, 2, \dots, N-1$ are the filter coefficients in RNS representation.

FIR filter can be implemented in a conventional scheme using delay elements. The delay elements actually pass the values delaying them by certain amount of time so that the signal values of the previous steps are multiplied with the corresponding coefficients. In this process, at each step, we need the computation of whole function.

The same FIR filter can be realized using Systolic Multiply-Accumulate architecture by implementing a pipelined Direct-Form filter [19], as depicted in Fig. 6. In this technique, the computation is partitioned into smaller parcels that can be assigned to a series of different concurrent processing elements in such a way as to achieve advantage in speed.

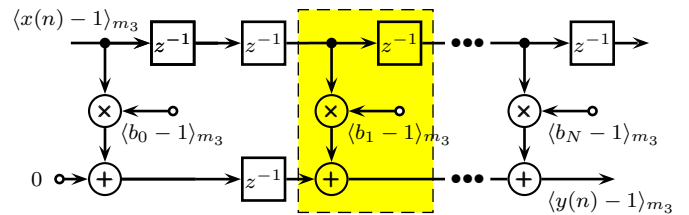


Fig. 6. Systolic realization of diminished-1 encoded channel ($m_3 = 2^n + 1$) of N -th-order nonrecursive digital filter. One processing element is dashed part of figure.

This linear phase lowpass filter, designed by means of published program based on the Parks-McClellan algorithm, is normalized so that the passband edge is 0.4π , stopband edge is

0.5π and the minimum stopband attenuation is 32.625dB. The filter coefficients are shown in Table III for double precision (the IEEE 754 standard) and for 10-bit precision in integer notation.

TABLE III
THE 31TH-ORDER FIR LOWPASS FILTER COEFFICIENTS FOR MODULI
SET $\{2^n - 1, 2^n 2^n + 1\}$, WITH $n = 6$.

Coefficients b_i	Double precision	Int.	RNS number ^a		
			$b_{i,1}$	$b_{i,2}$	$b'_{i,3}$
$b_0 = b_{24}$	-0.0005790732070	0	/	/	/
$b_1 = b_{23}$	0.0107143423917	5	5	5	4
$b_2 = b_{22}$	0.0056224531799	3	3	3	2
$b_3 = b_{21}$	-0.0121381434840	-6	58	57	58
$b_4 = b_{20}$	-0.0186695715150	-10	54	53	54
$b_5 = b_{19}$	0.0085434429402	4	4	4	3
$b_6 = b_{18}$	0.0385495109566	20	20	20	19
$b_7 = b_{17}$	0.0119972274970	6	6	6	5
$b_8 = b_{16}$	-0.0606997415311	-31	33	32	33
$b_9 = b_{15}$	-0.0684021145565	-35	29	28	29
$b_{10} = b_{14}$	0.0782461959053	40	40	40	39
$b_{11} = b_{13}$	0.3044489251280	156	28	30	25
b_{12}	0.4150604524227	213	21	24	17

^aThe RNS number $b'_{i,3} = \langle b_i \rangle_{m_3}$ is diminished-1 coded.

Since integer values of coefficients b_0 and b_{31} are equal to zero, the filter length is reduced to $N = 30$, as it is shown in Table III.

Integer values in the third column in Table III are transformed from floating point value (second column) in two steps. The first step is the conversion of floating point filter coefficients, b , into binary string b using two MATLAB[®] functions, `Q_1=quantizer('round',Format)` and `b_binary=num2bin(Q_1,b)`. Value of parameter `Format` creates parameters of binary numbers: `[wordlength,fractionlength]` for signed fixed-point mode. For 10-bit precision format these parameters are `wordlength=10` and `fractionlength=9`.

This paper investigates binary-to-residue converter for the modulo set $\{63, 64, 65\}$ with diminished-1 encoded $2^n + 1$ channel. In the following example we describe the fixed point-to-residue number system conversion of coefficient b_1 . Double precision of filter coefficient b_1 is -0.012138143484039 which is converted into binary number `b_binary=11111111010`, then into integer number `b_int=-6`, and finally into RNS number `b_RNS=(58, 57, 59)`.

The filter generated by RNS moduli set $\{2^n - 1, 2^n, 2^n + 1\}$ with diminished-1 encoded channel, for $n = 6$ provides the dynamic range $M = 262\,080$. Hereby the filter can operate in this range and provide better bit efficiency than existing standard RNS based filters.

A. Filter Performance

The simulation, performed in Matlab (R2010a), depicts the effects of this approach on the filter design.

Assume that the data sequence is quantized to 8 bits (including sign) and that filter must be implemented without

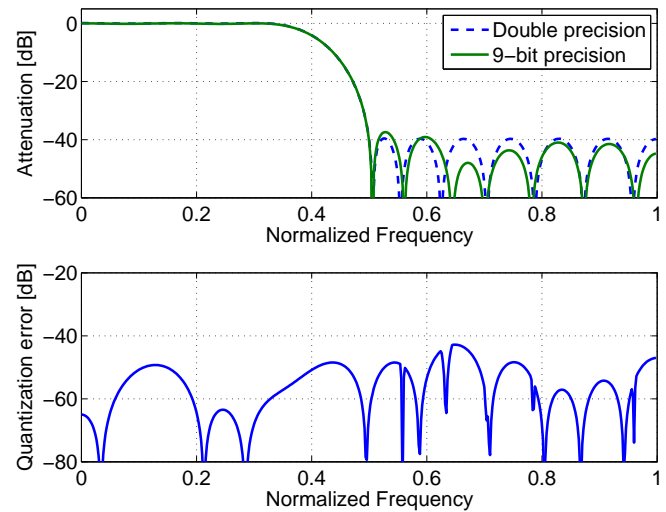


Fig. 7. Attenuation response (top) and quantization error for the coefficient rounding to 9-bit (bottom).

rounding error. An absolute upper bound of filter response $|y_m(n)|$ is given by equation (25)

$$|y_m(n)| \leq \max\{|x(n)|\} \sum_{k=1}^{23} |b_k| = 216320 \quad (25)$$

$$\approx 17.72 \text{ bits.}$$

The moduli set $\{63, 64, 65\}$ provides a dynamic range of 17.99 bits, which is adequate for the most practical cases since the bound of 17.87 bits, given by (25), is extremely pessimistic [20].

Figure 8 shows impulse response of the RNS channels. In $\{64, 63, 65\}$ proposed residue number system unit sample is

$$\delta(n) = \begin{cases} (51, 54, 47), & \text{for } n = 0 \\ (0, 0, 64), & \text{for } n > 0. \end{cases} \quad (26)$$

First two channels are normally encoded, but the third is diminished-1 encoded.

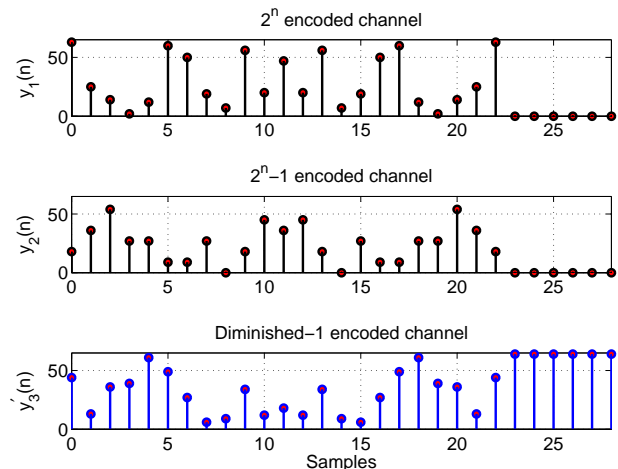


Fig. 8. The impulse response of the RNS channels: 2^n channel, above; $2^n - 1$ in the middle; $2^n + 1$ diminished-1 encoded channel, down.

Response of each channel is symmetric about 11-th sample. In diminished-1 encoded channel zero is coded with 64.

The impulse response of this digital filter is shown in Figure 9, where samples are given in integer form. The required number of bits is the sum of the coefficient bits and data bits. In this design it is 17 bits. Thus, dividing by 2^{17} the integer response is transformed into fixed point response.

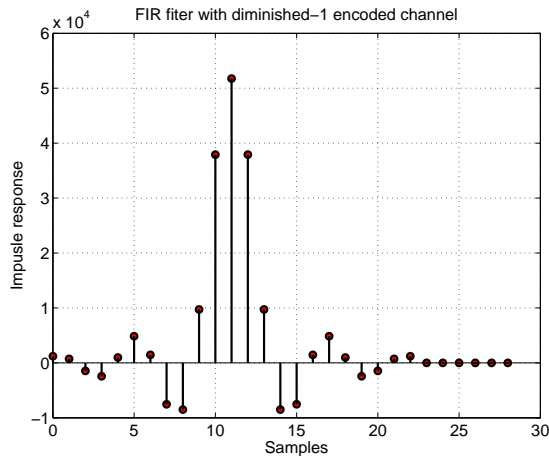


Fig. 9. Impulse response of the RNS lowpass filter.

IV. CONCLUSION

The design of a finite impulse response digital filter in a residue number system has been presented. The RNS coding technique with diminished-1 encoded channel is attractive for FIR filters which require only multiplication and addition because these operations are very fast in an RNS. The architecture of all building blocks, except residue-to-binary converter with diminished-1 encoded channel and architectures for modulo multiplication, has already been discussed in previous papers. The architecture for reverse convertor that includes diminished-1 encoded channel, which uses only binary adders without memory blocks, is proposed in this paper. To achieve high speed, new partial product generator combining with the Wallace tree is adopted for the multipliers.

Future research includes the extension of this study to Xilinx chips, the power-figure measurement and a full characterization of each design option at layout level.

ACKNOWLEDGMENT

This work was supported by the Serbian Ministry of Education and Science in the frame of the project TR 33008 and III 44004.

REFERENCES

- [1] W. K. Jenkins and B. Leon, "The use of residue number systems in the design of finite impulse response digital filters," *IEEE Trans. on Circuits and Systems*, vol. CAS-24, no. 4, pp. 191–201, Apr. 1977.
- [2] M. A. Soderstrand and B. Sinha, "A pipelined recursive residue number system digital filter," *IEEE Trans. on Circuits and Systems*, vol. CAS-31, no. 4, pp. 415–417, Apr. 1984.
- [3] P. A. Regalia, S. K. Mitra, P. Vaidyanathan, M. K. Renfors, and Y. Neuvo, "Three-structured complementary filter bank using all-pass sections," *IEEE Trans. on Circuits and System*, vol. CAS-34, no. 12, pp. 1470–484, Dec. 1987.

- [4] T. K. Shahana, R. James, B. Jose, K. Jacob, and S. Sasi, "Performance analysis of FIR digital filter design: RNS versus traditional," in *International Symposium on Communications and Information Technologies. ISCIT'07*, Kochi, Kerala, India, Oct. 17–19, 2007, pp. 1–5.
- [5] R. Conway and J. Nelson, "Improved RNS FIR filter architectures," *IEEE Trans. on Circuits and Systems-II: Express Briefs*, vol. 51, no. 1, pp. 26–28, Jan. 2004.
- [6] L. M. Leibowitz, "A simplified binary arithmetic for the Fermat number transform," *IEEE Transactions on Acoustics, Speech, and Signal Processing*, vol. ASSP-24, no. 5, pp. 356–359, Oct. 1976.
- [7] R. Zimmermann, "Efficient VLSI implementation of modulo $(2^n \pm 1)$ addition and multiplication," in *Proceedings of the 14th IEEE Symposium on Computer Arithmetic*, Adelaide, Australia, Apr. 1999, p. 158167.
- [8] Z. Wang, G. A. Jullien, and W. C. Miller, "An efficient tree architecture for modulo $2^n + 1$ multiplication," *VLSI Signal Processing*, vol. 14, no. 3, pp. 241–243, Mar. 1996.
- [9] H. T. Vergos, C. Efstathiou, and D. Nikolos, "High speed parallel-prefix modulo $2^n + 1$ adders for diminished-one operands," in *Proceedings of 15th IEEE Symposium on Computer Arithmetic*, Vail, CO, USA, June 11–13, 2001, pp. 211–217.
- [10] H. Vergos and C. Efstathiou, "A unifying approach for weighted and diminished-1 modulo $2^n + 1$ addition," *IEEE Trans. on Circuits and Systems-II: Express Briefs*, vol. 55, no. 10, pp. 1041–1045, Oct. 2008.
- [11] R. Chaves and L. Sousa, $\{2^n + 1, 2^{n+k}, 2^n - 1\}$: a new RNS moduli set extension. IEEE, 2004, pp. 210–217. [Online]. Available: <http://ieeexplore.ieee.org/lpdocs/epic03/wrapper.htm?arnumber=1333279>
- [12] C. Efstathiou, H. T. Vergos, and D. Nikolos, "Handling zero in diminished-one modulo $2^n + 1$ adders," *Int. J. Electronics*, vol. 90, no. 2, pp. 133–144, Feb. 2003.
- [13] C. Efstathiou, I. Voyiatzis, and N. Sklavos, "On the modulo $2^n + 1$ multiplication for diminished-1 operands," in *Proc. of the 2nd Int. Conf. on Signals Circuits and Systems (SCS 2008)*.
- [14] J. W. Chen, R. H. Yao, and W. J. Wu, "Efficient modulo $2^n + 1$ multipliers," *IEEE Transactions on Circuits and Systems*, vol. 19, no. 12, pp. 2149–2157, Dec. 2011.
- [15] A. Hämmäläinen, M. Tommiska, and J. Skyttä, "6.78 gigabits per second implementation of the IDEA cryptographic algorithm," in *Proceedings of the 12th Conference on Field-Programmable Logic and Applications (FPL 2002)*, M. Glesner, P. Zipf, and M. Renovell, Eds. Montpellier, France: Springer-Verlag, Sept. 2–4, 2002, pp. 760–759.
- [16] J.-L. Beuchat, "Some modular adders and multipliers for field programmable gate arrays," in *Proceedings of 17th International Symposium on Parallel and Distributed Processing, IPDPS'03*. Los Alamitos, CA, USA: IEEE Computer Society, Apr. 22–26, 2003, pp. 190–197.
- [17] C. Efstathiou, H. T. Vergos, G. Dimitrakopoulos, and D. Nikolos, "Efficient diminished-1 modulo $2^n + 1$ multipliers," *IEEE Transactions on Computers*, vol. 54, no. 4, pp. 491–496, Apr. 2005.
- [18] Z. Wang, G. Jullien, and W. Miller, "An improved residue-to-binary converter," *IEEE Transactions on Circuits and Systems I*, vol. 47, no. 9, pp. 1473–1440, Sept. 2000.
- [19] A. Antoniou, *Digital Signal Processing: Signals, Systems, and Filters*. New York: McGraw-Hill, 2006.
- [20] W. K. Jenkins and B. Leon, "The use of residue number systems in the design of finite impulse response digital filters," *IEEE Trans. on Circuits and Systems*, vol. CAS-24, no. 4, pp. 191–201, Apr. 1977.

Dragana Živaljević was born in Niš, Serbia, Yugoslavia, on February 14, 1972. She enrolled in the Faculty of Electronic Engineering, University of Niš, Serbia and received B.Sc. degree in 2001. Since 2002 she has been working as a lecturer and research assistant at the Department of Theoretical Electrical Engineering at the Faculty of Electronic Engineering in Niš. She is involved in conducting auditing exercises for courses Electrical Engineering I and II, Electrical Circuits Theory, Electromagnetic, Digital signal processing and Signals and systems.

Negovan Stamenković was born on march 30, 1979. He received the B.Sc. degree and M.Sc. degrees in electronics and telecommunications from the Electrical and Engineering Department at Faculty of Technique in Kosovska Mitrovica. He received Ph.D. degree in electronics and telecommunications from Faculty of Electronic Engineering at University of Niš. He was elected professor the Faculty of Sciences and Mathematics in Kosovska Mitrovica. His research is based on signal processing residue numerical system. ⁶²

Estimation of Direction of Arrival of Multiple Sound Sources in 3D Space Using B-Format

Hasan Khaddour, Jiří Schimmel, and Michal Trzos

Abstract—This contribution deals with sound source direction estimation in the three-dimensional space. An energetic analysis method based on B-format signals processing is presented in this paper. This method is able to estimate the direction of arrival for multiple sound sources in the three dimensional space. A single SoundField microphone can be used to pick-up B-format signals indirectly. The method has been simulated in Matlab and tested in a real environment. Experimental results demonstrate the validity of this method.

Keywords—Sound source localization, B-format signals, energetic analysis method.

I. INTRODUCTION

In the last years, several sound source localization methods have been invented to localize targets. They can be mainly divided into active and passive systems. Active systems send a sound pulse and receive the echo coming back after reaching a target, and then calculate the distance between the target and the main station. This method is used in active SONAR (sound navigation and ranging) [1]. The passive systems listen to the sound coming from the targets to locate them. Such method is used in passive SONAR. The passive systems can be divided into groups depending on the physical principle they use to localize the sound sources. The most physical principles used to localize the sound sources are the time delay estimation [2] and the phase difference [3]. Physical principle of the phase difference and time delay is essentially the same but the methods differ in approach to the estimation. Two or more microphones are used to pick-up the sound coming from the sound sources and then some methods are used to calculate the time delay. The time delay can be calculated as the time which gives the maximum correlation between the sound signals that picked up by the microphones. In case where the method is used to localize several sound sources, more microphones are needed. The phase difference depends on the frequency of the sound signal and on the propagation path difference. The phase difference should be calculated in the frequency domain after using short time Fourier transform with

Hanning window for instance. The corresponding outputs for each signal are then multiplied to achieve the cross spectrum. The cross spectrum is then overlapped and averaged to get the phase difference spectrum [4].

Many sound source localization methods have been proposed in the last decade. They differ in the number of sound sources they can localize and the ability of localization in the three dimensional space. The new methods try to reduce the number of used microphones. A method proposed in [5] uses three microphones to localize the sound sources in three dimensional space. However, that method needs special reflector and source counting, and it is used to localize a dominant sound source. Other methods can be used to localize multiple sound sources, whereas they use more microphones. For instance, in [6] an array of eight microphones is used for sound source localization and tracking. However, the previous method is able to estimate the distance of the sound source too.

This paper presents an approach referred to as sound source direction estimation using energetic analysis, which aims at estimating the direction of arrival for multiple sound sources in three dimensional space depending on energetic analysis of B-format signals, i.e., the direction of the sound sources. Three B-format signals are needed to estimate the direction of the sound sources in the horizontal plane only, while four B-format signals are needed to estimate the direction of the sound sources in three dimensional space.

The paper is organized as follows: B-format signals are described in Section 2. The energetic analysis method is introduced in Section 3. Section 4 presents the simulation results. Experimental results in both horizontal and vertical planes are presented in Section 5 and conclusion can be found in Section 6.

II. B-FORMAT SIGNALS

A. B-format Principle

B-format signals consist of four signals namely $x(t)$, $y(t)$, $z(t)$ and $w(t)$, which carry the information about the acoustic field near to the microphone [7]. The signals $x(t)$ and $y(t)$ carry information about horizontal plane, $z(t)$ carries information about vertical plane and $w(t)$ is an omnidirectional signal, see Fig. 1.

The encoding equations for B-format signals are [7]

$$\begin{aligned} x(t) &= \cos \alpha \cos \beta s(t), \\ y(t) &= \sin \alpha \cos \beta s(t), \\ z(t) &= \sin \beta s(t), \end{aligned} \tag{1}$$

Manuscript received November 10, 2012. The described research was performed in laboratories supported by the SIX project; the registration number CZ.1.05/2.1.00/03.0072, the operational program Research and Development for Innovation.

H. Khaddour is with the Department of Telecommunication FEEC, Brno University of Technology, Brno, Czech Republic (phone: +420-541-149-210; fax: +420-541-149-192; e-mail: xkhadd00@stud.feec.vutbr.cz).

J. Schimmel is with the Department of Telecommunication FEEC, Brno University of Technology, Brno, Czech Republic (phone: +420-541-149-210; fax: +420-541-149-167; e-mail: schimmel@feec.vutbr.cz).

M. Trzos is with the Department of Telecommunication FEEC, Brno University of Technology, Brno, Czech Republic (phone: +420-541-149-195; fax: +420-541-149-192; e-mail: xtrzos00@stud.feec.vutbr.cz).

doi: 10.11601/ijates.v2i2.35

$$w(t) = \frac{1}{\sqrt{2}}s(t)$$

where α represents the azimuth angle of the source, β represents the elevation angle of the source and s represents the sound signal.

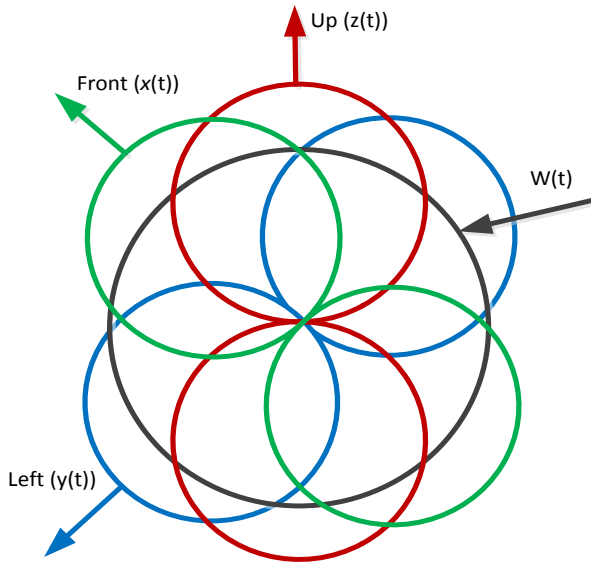


Fig.1. Polar patterns of B-format components.

In order to record B-format signals directly, a combination of coincident conventional microphones is needed, whereas three figure-of-eight microphones are used to pick-up the signals $x(t)$, $y(t)$, and $z(t)$, an omnidirectional microphone is used to pick up the $w(t)$ signal.

B. A-format Signals

B-format signals can be derived from A-format signals. A single SoundField microphone can be used to pick-up A-format signals [8]. As can be seen in Fig.2, the microphone consists of four capsules to pick up the sound in the directions left-front, right-front, left-back and right-back.



Fig.2. SPS200 SoundField microphone used to record A-format signals.

After recording A-format signals, B-format signals can be derived by the equations [9]

$$x(t) = 0.5((LF - LB) + (RF - RB)),$$

$$y(t) = 0.5((LF - RB) - (RF - LB)),$$

$$z(t) = 0.5((LF - LB) + (RF - RB)),$$

$$w(t) = 0.5((LF + LB) + (RF + RB))$$

(2)

where $x(t)$, $y(t)$, $z(t)$ and $w(t)$ are B-format signals, and LF, RF, LB and RB correspond to the signals recorded by the capsules left-front, right-front, left-back and right-back respectively.

III. ENERGETIC ANALYSIS METHOD

The principle of energetic analysis method is that the sound source direction is the opposite direction of the intensity vector of the sound. This principle is used also in directional audio coding (DirAC) [10].

In time domain, the instantaneous acoustic intensity can be written as [11]

$$\vec{I}(t) = p(t)\vec{v}(t) \quad (3)$$

where $p(t)$ is the acoustic pressure and $\vec{v}(t)$ represents the particle velocity vector.

In energetic analysis method, the sound signals are first divided in time and then in frequency using short Fourier transform method (STFT). For each time frame, the intensity vectors are computed in frequency domain. The instantaneous intensity vector can be derived from the B-format signals, it can be written as [12]

$$\mathbf{I}(t, f) = [I_x(t, f), I_y(t, f), I_z(t, f)]^T \quad (4)$$

where its component can be derived from the equations

$$I_x(t, f) = \frac{1}{\sqrt{2}Z_0} \text{Re}\{W^*(t, f) \cdot X(t, f)\},$$

$$I_y(t, f) = \frac{1}{\sqrt{2}Z_0} \text{Re}\{W^*(t, f) \cdot Y(t, f)\}, \quad (5)$$

$$I_z(t, f) = \frac{1}{\sqrt{2}Z_0} \text{Re}\{W^*(t, f) \cdot Z(t, f)\}$$

where Z_0 is the acoustic impedance of the air, t is time, f is frequency, $*$ denotes complex conjugate, $X(t, f)$, $Y(t, f)$, $Z(t, f)$ and $W(t, f)$ are the Fourier transform for the B-format signals $x(t)$, $y(t)$, $z(t)$ and $w(t)$ respectively.

After calculating the intensity vector for each time frame, the direction of sound can be calculated using these equations for the azimuth [11]

$$\alpha(t, f) = \begin{cases} \tan^{-1} \left[\frac{-I_y(t, f)}{-I_x(t, f)} \right] & \text{for } I_y(t, f) \geq 0, \\ \tan^{-1} \left[\frac{-I_y(t, f)}{-I_x(t, f)} \right] - 180^\circ & \text{for } I_y(t, f) < 0, \end{cases} \quad (6)$$

and this equation is used to estimate the elevation

$$\beta(t, f) = \tan^{-1} \left[\frac{-I_z(t, f)}{\sqrt{I_x(t, f)^2 + I_y(t, f)^2}} \right]. \quad (7)$$

As it can be seen from the previous equations, the azimuth and the elevation is calculated for each frequency bin in each time frame, and then the azimuth and the elevation can be determined, see Fig.3.

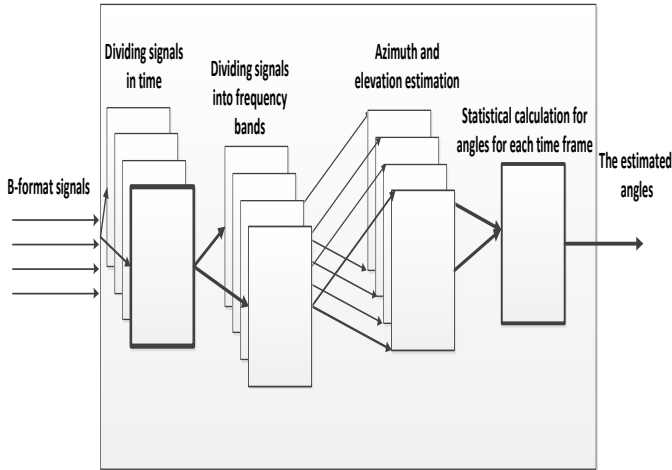


Fig.3. Energetic analysis method's diagram.

During a single time frame, each frequency bin carries information about direction of one sound source with dominant intensity in given frequency bin. We assume that only one single sound source is dominant in this case. This assumption can be hold since the sound signals differ from each other, and they have different spectral intensity in each time frame. After calculating the azimuth and elevation, a statistical process should be done to choose the most likelihood angles, from which the sound comes from as follows: assuming we have only one sound source, the estimation of direction or arrival of sound is determined as the angle that maximizes the summation of function $(\alpha(t, f))$ on the whole frequency interval for each time frame, and it could be written as

$$N(\alpha) = \sum_{k=0}^K p(\alpha(t, f_k) | \alpha), \quad (8)$$

$$\alpha_{estimated} = \arg \max N(\alpha),$$

and the elevation as

$$N(\beta) = \sum_{k=0}^K p(\beta(t, f_k) | \beta), \quad (9)$$

$$\beta_{estimated} = \arg \max N(\beta),$$

where $\alpha_{estimated}$, $\beta_{estimated}$ are the estimated sound source angles (azimuth and elevation respectively), K is the number of the frequency bins for $\alpha \in (-\pi, \pi)$, and $\beta \in (0, \pi)$, $\alpha(t, f_k)$ is the vector of azimuths, t denotes the time frame

index, k is the frequency bin, and $(\alpha(t, f_k) | \alpha)$ is the probability that this signal comes from the direction α which is estimated from each frequency bin according to (6).

IV. SIMULATION RESULTS

Simulation results show the ability of this method to estimate direction of arrival of sound sources in both vertical and horizontal planes. Assuming we have three sound sources around the microphone, B-format signals can be generated from these signals according to (1). In the first simulation scenario, three sound sources were assumed to be around the microphone, with absence of noise. As can be seen in Fig. 4, the method was able to estimate the sound sources directions correctly, where the peaks denote the three estimated angles.

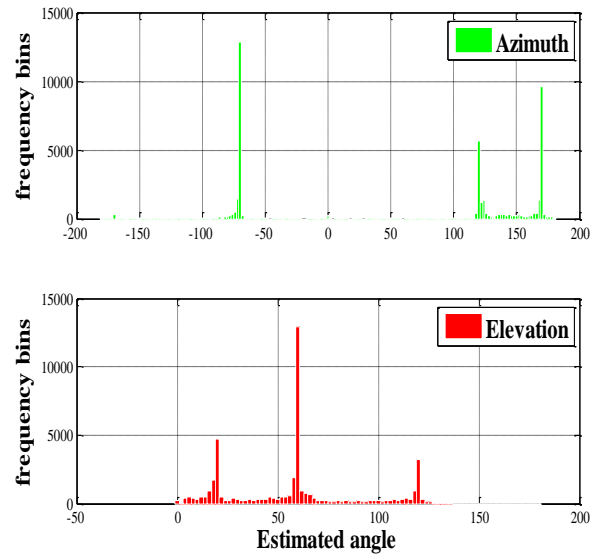


Fig.4. Simulation results in absence of noise.

In this simulation part, two different noise signals were added to each B-format signal. The first noise signal is a fan's noise signal, the spectral density distribution of this signal is shown in Fig.5. The second noise signal is pseudo-random noise with a normal distribution with mean zero and standard deviation of one which is generated by Matlab.

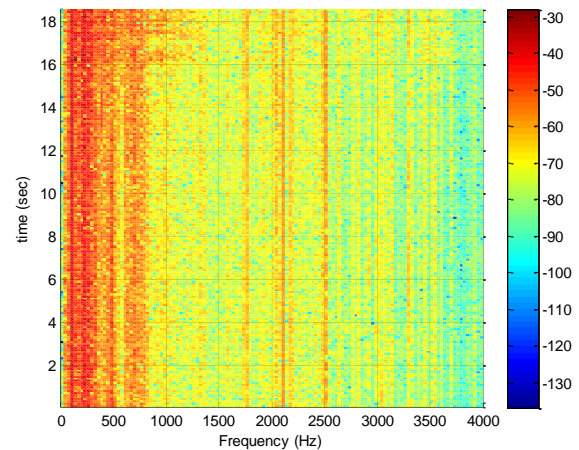


Fig.5. Spectral density distribution for a fan noise sound signal.

The two noise signals were assumed to surround the

microphones in both horizontal and vertical planes. The signals were assumed to be equidistantly separated (i.e. 4 degrees from each other in the horizontal plane and 5 degrees from each other in the vertical plane).

Simulation results are shown in Fig.6. As can be seen, the method is able to determine the direction of the sound sources in both vertical and horizontal plane, where the peaks denote the sound sources direction of arrival. The present of the noise signals affected the accuracy of the method, where some frequency bins denote to the direction of the noise signal sources. The SNR between $w(t)$ and the noise signal in our simulation is about -26 dB.

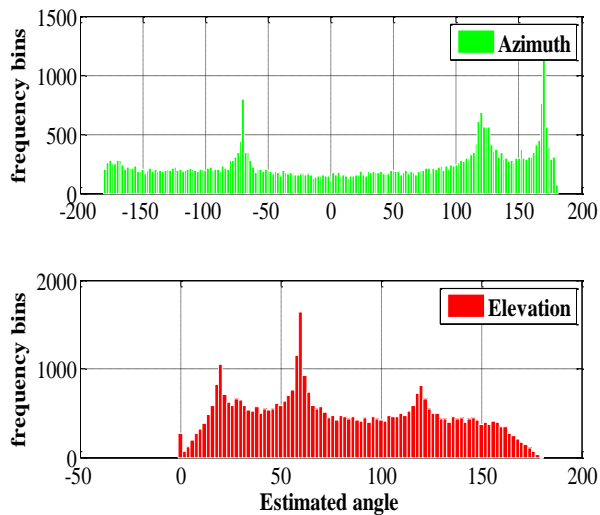


Fig.6. Simulation result with the present of pseudo-random noise signal and a fan noise signal.

V. EXPERIMENTAL RESULTS

The measurements were carried out in the acoustic laboratory at Department of Telecommunications FEEC, Brno University of Technology, where the conditions of the experiment were same as in sound control rooms, listening rooms, or in living rooms with high quality listening environment; the laboratory provides semi-diffuse field with reverberation time $RT_{60} < 0.3$ s in all octave bands.

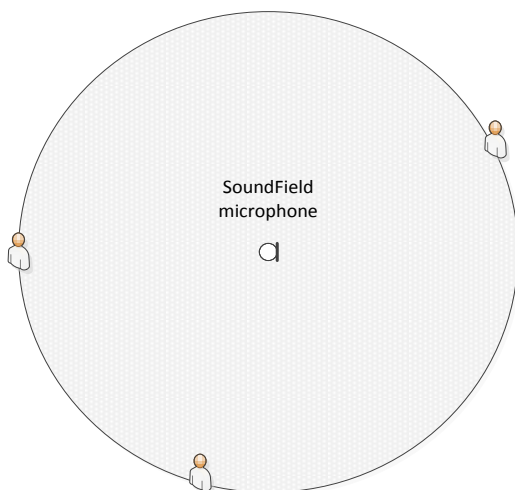


Fig.7. Recording the sound using soundfield microphone. The measurements were carried out in both horizontal and

vertical plane. The recording was made for three speakers (three men), who stood around the microphone in different arbitrary positions, see Fig.7.

Soundfield microphone was used to pick-up the sound, after recording the A-format signals, the B-format signals were derived according to (1).

In the first part of our experiment, three men were talking simultaneously in three arbitrary positions around the microphones, see Fig.7; the measurements were repeated forty times. The results for those forty measurements in the horizontal plane are shown in Fig.8. The results are shown using box plots. The boxes have lines at lower quartile, median, and upper quartile values. The whiskers show the extent of the rest of the data. The outliers are presented by red cross outside of the whiskers. As can be seen in Fig.8, the median error for the speakers was about 5 degrees for the first speaker, and 4 degrees for the second and the third speaker.

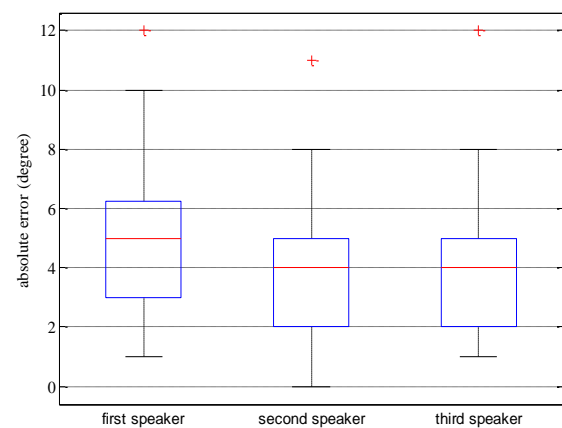


Fig.8. Average absolute angle error for the three speakers in the horizontal plane.

In the second part of the experiment, the same three men, as in the first part, were talking simultaneously in vertical plane; the measurement was repeated twenty times. The absolute angle error in the vertical plane is shown in Fig.9, it can be seen that the median error in this case was about 5 degrees for the first and second speakers and 4 degrees for the third speaker.

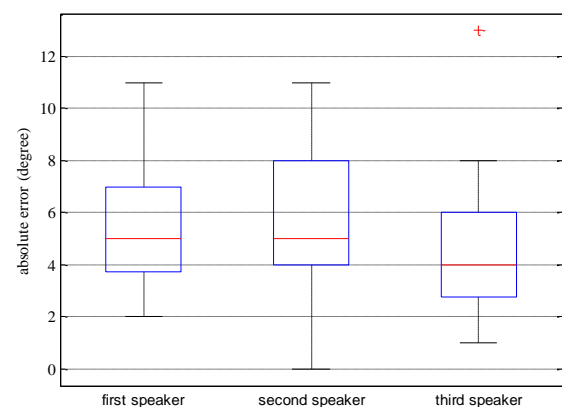


Fig.9. Average absolute angle error for the three speakers in the vertical plane.

The error that happens when this method is used comes mostly from the reverberation in the room and from the noise signals.

As can be seen in Fig.8 and Fig. 9 the method is able to estimate the direction of arrival for multiple sound sources in both horizontal and vertical plane, the median error was about 4 degrees.

Compared to our method, eight microphones are used in a method presented in [6] for three dimensional localization and tracking of sound sources, whereas our method is able to estimate the direction of the sound sources in three dimensional space using four signals. However, the absolute angle error is bigger in our method. The angle absolute error in our method is about 4 degrees whereas the angular accuracy was better than one degree for a stationary source at 1.5 meter distance in the method presented in [6]. The simulation results for the method presented in [5] showed that the method was able to localize a dominant sound source using three microphones. The angle of arrival absolute error for this method differs depending on the kind of added noise and the SNR. The simulation results for this method showed that the angle error in absence of white Gaussian noise was about 3% when SNR was about -20 dB, and the angle error was 100% in absence of pink noise and SNR less than 0 dB. However, our method is able to localize multiple sound source using only three signals in the horizontal plane and four signals in the three dimensional space with absence of mixed fan's noise and pseudorandom noise and SNR about -26 dB.

VI. CONCLUSION

A method for three dimensional sound sources direction estimation was presented. This method is able to estimate the direction of multiple sound sources in both horizontal and vertical plane. Simulation results showed the affectivity of this method in both absence and presence of the noise signals. Experimental results showed that this method was able to estimate the direction of sound sources in three dimensional space.

REFERENCES

- [1] de Moura, N.N.; Seixas, J.M.; Filho, W.S.; Greco, A.V.; , "Independent Component Analysis for Optimal Passive Sonar Signal Detection," *Intelligent Systems Design and Applications, 2007. ISDA 2007. Seventh International Conference on* , vol., no., pp.671-678, 20-24 Oct. 2007.
- [2] Carter, G.C.; , "Coherence and time delay estimation," *Proceedings of the IEEE* , vol.75, no.2, pp. 236- 255, Feb. 1987.
- [3] Schmidt, R.; , "Multiple emitter location and signal parameter estimation," *Antennas and Propagation, IEEE Transactions on* , vol.34, no.3, pp. 276- 280, Mar 1986.

- [4] Shimoyama, R.; Yamazaki, K.; , "Acoustical source localization using phase difference spectrum images", *Acoust. Sci. & Tech.*, 24 pp.161-171 February 2003.
- [5] Pourmohammad, A.; Ahadi, S.M.; , "TDE-ILD-HRTF-Based 3D entire-space sound source localization using only three microphones and source counting," *Electrical Engineering and Informatics(ICEEI), 2011 International Conference on* , vol., no., pp.1-6, 17-19 July 2011.
- [6] Valin, J.-M.; Michaud, F.; Rouat, J.; , "Robust 3D Localization and Tracking of Sound Sources Using Beamforming and Particle Filtering," *Acoustics, Speech and Signal Processing, 2006. ICASSP 2006 Proceedings. 2006 IEEE International Conference on* , vol.4, no., pp.IV, 14-19 May 2006.
- [7] Benjamin, E.; Lee, R.; Heller, A. ; "Localization in horizontal-only ambisonic systems, " in *Proc. 121st Convention of the Audio Engineering Society*, San Francisco, pp.12, 2006.
- [8] *Sound field technology, how was it work.* [Online]. [Cited 25.10.2012]. Accessible from <http://www.soundfield.com/soundfield/soundfield.php>.
- [9] Rusemy, F., McCormick, T. *Sound and Recording*. Linacre House, Jordan Hill, Oxford OX2 8DP, UK. 2009.
- [10] Pulkki, V. ; "Spatial Sound Reproduction with Directional audio coding" *J. Audio Eng.Soc.*,vol.55,pp.503-516,Jun 2007.
- [11] Williams, E.; *Fourier Acoustics: Sound Radiation and Nearfield Acoustical Holography* , Academic Press, USA. 1999.
- [12] E. Ahonen, J.; Pulkki, V.; Kuech, F.; Kallinger, M.; Schultz-Amling, R.; "Directional analysis of sound field with linear microphone array and applications in sound reproduction". In *Proc. AES 124th Convention*, Amsterdam, The Netherlands, May 2008.

Hasan Khaddour received his Eng. title from the Department of Telecommunications and Electronics, Faculty of Mechanical and Electrical Engineering, Tishreen University, Syria, in 2007. Since 2009, he is a Ph.D. candidate at the Department of Telecommunications, Faculty of Electrical Engineering, Brno University of Technology (BUT), Czech Republic. His current research is focused on sound source localization, acoustical zooming, and sound rendering methods.

Jiří Schimmel received his M.Sc. and Ph.D. degrees in Electronics and Communications in 1999 and in Teleinformatics in 2006. He is currently an assistant professor at the Department of Telecommunications of the Faculty of Electrical Engineering and Communication of Brno University of Technology, Czech Republic. His research is focused on acoustics, multichannel digital audio signal processing, and software and hardware development for real-time audio signal processing systems. He is a member of the AES and IEEE.

Michal Trzos received B.Sc. degree in teleinformatics and M.Sc. degree in telecommunications and informatics from the Faculty of Electrical Engineering, Brno University of Technology (BUT), CZE, in 2007 and 2009 respectively. Since 2009, he is a Ph.D. candidate at the Department of Telecommunications. His main task is to explore new methods of time and frequency warping of audio signals. His research interests include: general-purpose computing on graphics processing units, audio algorithm parallelization, time-frequency transformations, and speech processing.

Definition of Typical Textures of Sedimentary Grains Using Co-occurrence Features And *K*-means Clustering Technique

Aleš Křupka

Abstract— The paper deals with a definition of typical structure forms, which can be extracted from the surface of sedimentary grains. The co-occurrence features are used for this purpose. To find typical patterns, the *K*-means clustering technique is used to group related data in feature space. Then, it is visually investigated if related data in feature space are also related when being perceived by human. The scheme for a specific grain texture definition is proposed and three models of grain textures are experimentally created. The first model involves especially significant grain corners and edges, the second model involves homogeneous parts of a grain, the third model can be used for coarse and abraded surface recognition.

Keywords—Texture, sedimentary grains, co-occurrence matrix, *K*-means, clustering.

I. INTRODUCTION

The goal of geomorphological research is to reveal a relief genesis of an investigated area. This research can be carried out by the methodology called exoscopy. Specifically, this process means the analysis of unlithified sedimentary grains. The grains are examined and typical structural features are sought on its surface. Such features can be the degree of roundness, presence of fractures, and so on [1]. When a set of grains (contained in one sample) is analyzed, the histograms of particular features are constructed and typical features for a given genesis are stated. Because these grains are of small sizes, electron microscope is utilized for magnifying and capturing them, see Fig. 1. After zoomed images are obtained, they are manually analyzed by experienced expert. This procedure is very time consuming. Because the analysis is done by using images, it could be possible to incorporate image processing techniques into the analysis to shorten the analysis time or to bring some new information suitable for genesis evaluation.

The objective of this paper is to define typical structure forms, which can be recognized on the surface of sedimentary grains by using a computer. As stated in the previous paragraph, the information about a grain surface character, described by typical structure forms, can be used to build statistics about a set of grains (one sample) and these statistics can be used for genesis estimation in the exoscopy analysis. The purpose of computer usage is to ease the routine work of experts. Typical structure forms, which are

sought on the grain surface, have been already defined by geomorphologists. However, the implementation of a procedure which would be able to extract the defined structures is not straightforward due to the complex nature of grain surface. Thus, structure forms, which can be easily obtained by using computers and also which can be interpreted by human expert need to be found.

The co-occurrence features and a clustering technique are used in this task. The computer analysis of grains is conducted from the perspective of texture analysis for which the co-occurrence features are widely used. The reason is that the grain surface structures exhibit some degree of randomness and generally, texture can be seen as a mixture of typical patterns with some degree of random variability [2]. Then, the *K*-means clustering technique is used for investigating the feature space presented by the co-occurrence features. Individual clusters, which represent a given texture type in feature space, are examined if they also represent a particular texture type when visually perceived by human. There are papers dealing with texture and clustering utilization [3][4]. However, they are motivated by using the texture analysis for segmentation. Moreover, these methods are evaluated on the images from general synthetic testing databases. In this study, the main point is to define grain structure forms, which can be described by co-occurrence features.

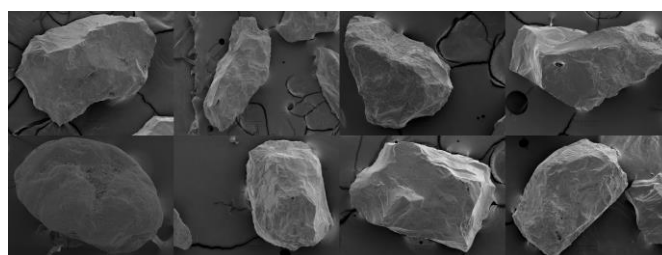


Fig. 1. Examples of grain images acquired by electron microscopy

II. PRINCIPLES

A. Co-occurrence matrix

Co-occurrence matrix [5] represents spatial relations between values of pixels in an image. Consider images p_1 and p_2 , where p_2 is created by shifting p_1 with distance (x,y) in Cartesian coordinates. These images are overlapped and number of pixel pairs with values (i,j) , where i is value in p_1 and j in p_2 , is written on the position of i -th row and j -th column in the co-occurrence matrix $P(i,j)$. $P(i,j)$ is thus constructed for a given parameters (x,y) . When $P(i,j)$ is

Manuscript received March 28, 2013.

A. Křupka is with Department of Telecommunications, Brno University of Technology, 612 00 Brno, Czech republic
e-mail: akrupka@phd.feec.vutbr.cz

normalized by number of pairs, joint distribution $p(i,j)$ of pair values is obtained. The co-occurrence matrix is square and its size is equal to number of possible intensity values in images p_1 and p_2 . The size of co-occurrence matrix thus can be reduced by stronger quantization of image. The co-occurrence matrix is still very raw representation of texture, thus different measures are used to describe texture [6]. The mostly used measures are the following

$$\text{contrast} = \sum_{i,j} |i-j|^2 p(i,j) \quad (1)$$

$$\text{correlation} = \sum_{i,j} \frac{(i-\mu_i)(j-\mu_j)p(i,j)}{\sigma_i\sigma_j} \quad (2)$$

$$\text{energy} = \sum_{i,j} p(i,j)^2 \quad (3)$$

$$\text{homogeneity} = \sum_{i,j} \frac{p(i,j)}{1+|i-j|} \quad (4)$$

where the range of i and j is given by size of $p(i,j)$, μ_i, μ_j are marginal means of $p(i,j)$ distribution, σ_i, σ_j are marginal standard deviations of $p(i,j)$ distribution. When p_1 is a subpart of some bigger image, then the features can be considered as local. This way, the texture of image subpart is described. By changing the parameter (x,y) , different features for a given sub-window can be extracted using previous formulas so a feature vector for the sub-window is obtained. Because no prior information about a texture type of the extracted sub-windows is known, no labels belong to the extracted feature vectors and thus, the desired texture models cannot be formed using some supervised machine learning algorithm. Moreover, it is desirable to evaluate the possibilities of co-occurrence features obtained from the sedimentary grains. Therefore, the key idea is to investigate the feature space of co-occurrence features if it is possible to specify some of feature space subparts, which present some kind of texture. This way, typical structure forms of sedimentary grains could be defined and it could be then distinguished between them. For this reason, clustering can be used to inspect if similarity in data space corresponds to texture similarity perceived by human.

B. K-means

The well-known K -means algorithm of clustering can be used [7]. This algorithm allows to group D -dimensional data consisting of N samples x_n into clusters according to their inter-samples distances, where $n = 1, \dots, N$. The goal is to construct centroids $\{\mu_k\}$, where $k = 1, \dots, K$, such that centroid μ_k belongs to k -th cluster. The data point x_n is then assigned to the cluster, whose centroid is in the smallest distance from x_n . Euclidean metric $\|x_n - \mu_k\|^2$ is usually used as the distance. During the procedure of searching for optimal centroids μ_k , an optimization objective is given by

$$J = \sum_{n,k} r_{nk} \|x_n - \mu_k\|^2$$

where $r_{nk} = 1$, if data sample x_n is assigned to k -th cluster, otherwise $r_{nk} = 0$. Thus, the term J represents the sum of the squares of the distances between sample and its assigned cluster with centroid μ_k . To minimize J , sets of the $\{r_{nk}\}$ and the $\{\mu_k\}$ need to be found. This is done by an iterative optimization procedure where each iteration consists of two steps. In the first step, the minimization is done with respect to $\{r_{nk}\}$, which means to assign data samples x_n to its closest cluster centroids μ_k . In the second step, the minimization is done with respect to $\{\mu_k\}$, the value of μ_k is computed as the

mean of data samples assigned to the k -th cluster. This optimization is repeated until convergence. Usually the initialization of the set $\{\mu_k\}$ is done by assignment of randomly selected data samples to the cluster centroids μ_k . The optimization procedure does not guarantee to reach the global optimum of J , so to bring up the chance of ending up in the best local optimum, the iterative optimization can be repeated multiple times with different random initialization of the centroids μ_k , after that, the model with the lowest J is selected.

III. METHOD

A. Implemented procedure

This part describes the implemented procedure using previously mentioned principles. A primitive used for the texture evaluation is a square sub-window taken from an image. The square sub-windows are sequentially extracted from the image with a given step. Co-occurrence matrices for several offsets (x,y) are then constructed from the sub-windows, and measures (1)(2)(3)(4) are computed. This way a dataset from available image set is obtained, the feature extraction process is shown in Fig. 2.

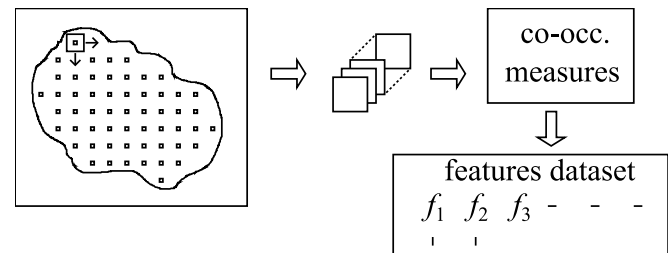


Fig. 2. Procedure of feature extraction: From the images, square subparts are obtained, which are used for construction of co-occurrence matrices. The measures of co-occurrence matrices constructed from a single sub-window form a single feature vector.

After the extraction, examination of feature data is performed. The K -means clustering technique is used to divide the dataset into parts homogeneous in feature space. Then the result of clustering is visually evaluated, see Fig. 3. From the first clustering result, visually recognizable type of texture, which seems to be consistently included in one or more clusters, is selected.

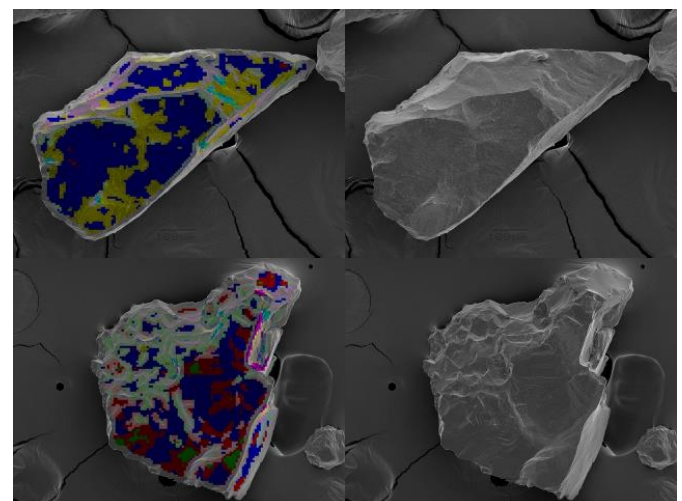


Fig. 3. Example of initial clustering for $K = 9$.

It is certainly possible that more than one type of texture perceived by human can be included into one cluster, therefore, the selection scheme demonstrated in Fig. 4 is applied. This selection scheme can be understood as a decision tree, where the clusters not fitting to a given texture are discarded. On the rest of data, K -means procedure is applied and the result is again visually examined. This way the subpart of feature space, which belongs to visually related textures, is determined more specifically.

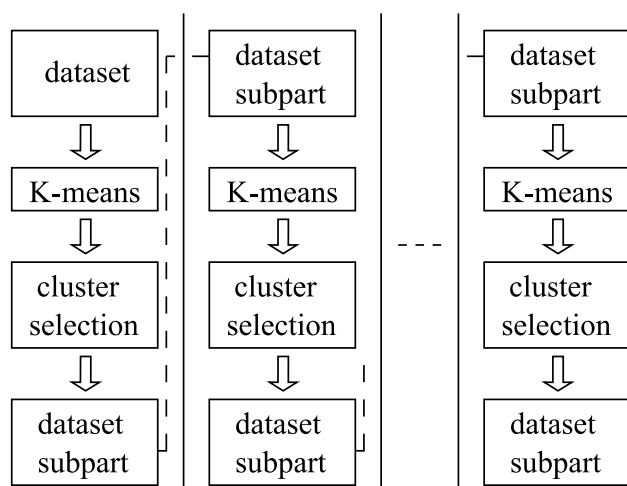


Fig. 4. Procedure for texture modeling. A model is specified by a subpart of feature space.

B. Experiment scheme and properties

Here follow the parameters of the experiment. The resolution of the images is 1280x960 pixels. A sedimentary grain is located in the middle of image and covers a significant part of the image. The square sub-windows for features extraction are of size 30 pixels and they are picked with horizontal and vertical step of 8 pixels. To avoid extracting sub-windows from the background parts of an image, manually prepared masks determining the area of a grain are used for controlling the extraction of the sub-windows. From every sub-window, co-occurrence matrices are extracted for parameters (1,0), (1,1), (0,1), (-1,1), (15,0), (15,15), (0,15), (-15,15), which represent shifts in directions of 0, 315, 270, 225 degrees, the opposite directions are ignored from the assumption of texture periodicity. The shift of 1 or 15 pixels in x and y directions is chosen to exhibit co-occurrences in closer spatial relations as well as in the distance of half sub-window width. The intensity values of sub-windows are uniformly quantized to 16 levels to get smaller size of co-occurrence matrices. From the prepared co-occurrence matrices, the feature vectors are computed as described in Section III a). The number of features in a vector is 32 because of 8 offsets of co-occurrence matrices multiplied by 4 measures computed from them. For getting texture data the set of 100 images is used.

The K is set to 9 to provide sufficiently fine clustering and still to allow good cluster visualization by different colors, see Fig. 3. Then the set of 100 pictures is visually examined and a type of texture, which seems to be well defined by clusters, is selected. Thus the subpart of dataset is selected for the next stage of clustering. This procedure is repeated several times to define the best possible subpart of feature space, which corresponds to visually consistent texture type.

The model created by scheme in Fig. 4 is then visually evaluated on the other independent test set of images.

IV. EXPERIMENTAL RESULTS

A. Created models

The experiments were conducted according to description in the previous part. During the experiments, three texture models using co-occurrence features were created.

The first model locates the sharp and contrast edges as can be seen in Fig. 5. The color marks located in different parts of the image represent the centers of sub-windows, whose content meets the given texture model.

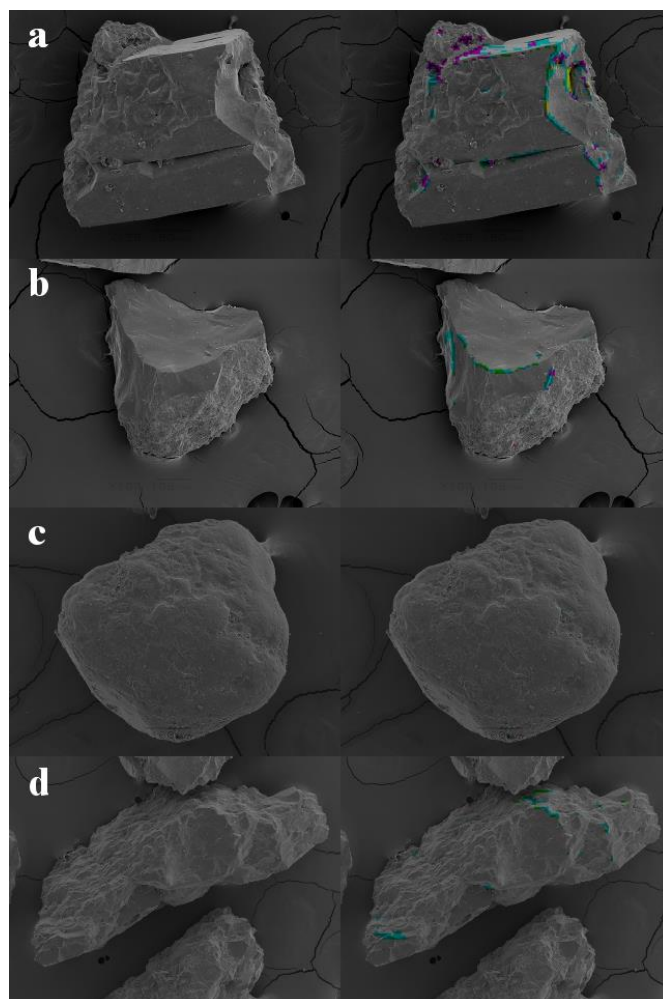


Fig. 5. Example of visualization using the first model: Left side presents the original image; right side highlights the sub-windows, whose texture belongs to the first model.

The second model was designed to address especially homogeneous part of the grain surface. This way especially smooth and plain parts of grain are detected which is visualized on samples in Fig. 6.

The third model is aimed to texture of rough and variable grain surface, which is illustrated in Fig. 7.

B. Discussion

As can be seen, the clustering of dataset is being used for defining typical structural pattern contained in an examined image subpart. According to initial clustering results, three texture models were defined as subparts of the whole feature

space using procedure in Fig. 4. In the right part of Fig. 5, Fig. 6 and Fig. 7, the positions of sub-windows whose feature vectors belong to the subpart of feature space defined by a model are highlighted by color spots. Different colors stand for different clusters defined in the last stage of procedure shown in Fig. 4, however, all of these different clusters belong to one defined model.

The first constructed model defines the feature space subpart, which includes especially the parts of grain surface containing significant rapid intensity changes, see Fig. 5. The corners connecting two well visible plains are the most probable to be involved by the model, see Fig. 5a, b. On the other hand, well rounded grains do not contain a lot of these corners and thus a small number of sub-windows belongs to the first model, see Fig. 5c. A grain with coarse surface can miss well distinct corners, therefore, a small number of color spots can be seen in Fig. 5d.

The second model is designed for inclusion typically homogeneous parts of texture. Fig. 6a,b demonstrate highlighted homogeneous plains. Also parts of a well rounded grain without coarse structure are captured by the second model, see Fig. 6c. Conversely, a grain with rough structure has a minimum of homogeneous parts which is also reflected in small number of highlighted sub-windows in Fig. 6d.

The third model is aimed to coarse structure generated e.g. by surface abrasion, which is clearly visible in Fig. 7 where the sub-windows containing rough texture are highlighted.

The distinctive corners as well as smooth plains on the grain surface are omitted by the third model.

The classified sub-windows according to created models can be used for percentage computation of a given texture occurrence on the grain surface. This way, statistics can be evaluated by geomorphologists and these results can be included to the conclusions stated about particular geomorphological genesis. This classification scheme can be also used as one particular step in possible multi-stage grain processing. As can be noticed in the presented figures, some sub-windows can be highlighted by a model in spite of their visual non-similarity to the model, which can be caused by intersection of visually different textures in feature space. However, the experiments showed that typical textures are densely filled with correctly classified sub-windows, thus areas with a high concentration of highlighted sub-windows can be considered as areas of texture given by the used model. This offers e.g. to determine grain parts for further specific processing dependent on texture. The sub-windows highlighted by the first model are typically positioned into thin lines so they represent the corners of the grain. If these lines would be properly extracted by further processing, the roundness of a grain could be evaluated not only from the shape borders of 2D projection (for which some methods have been done) but also from the presence of corners inside the grain.

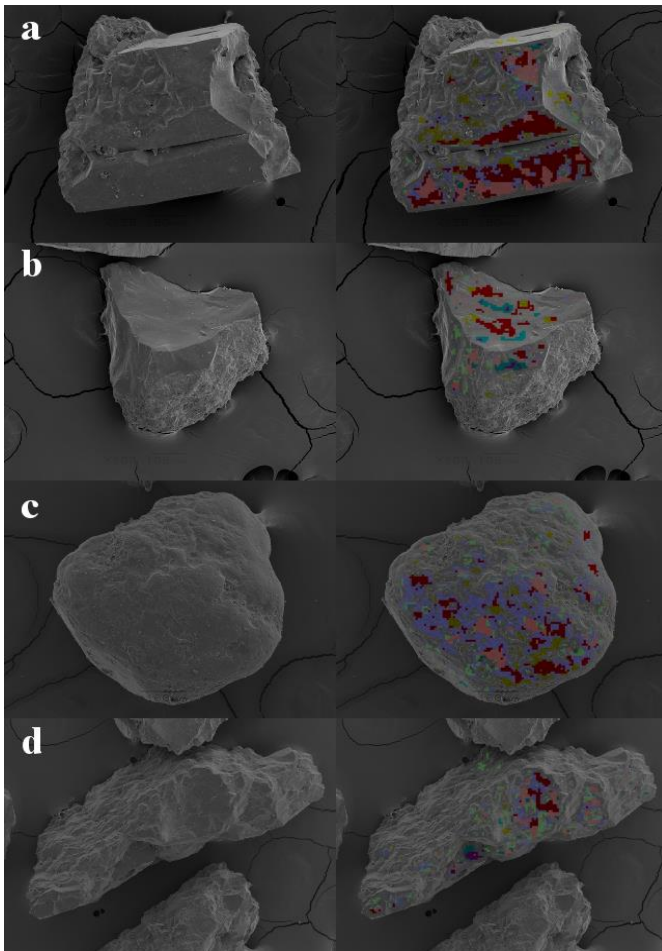


Fig. 6. Example of visualization using the second model: Left side presents the original image; right side highlights the sub-windows, whose texture belongs to the second model.

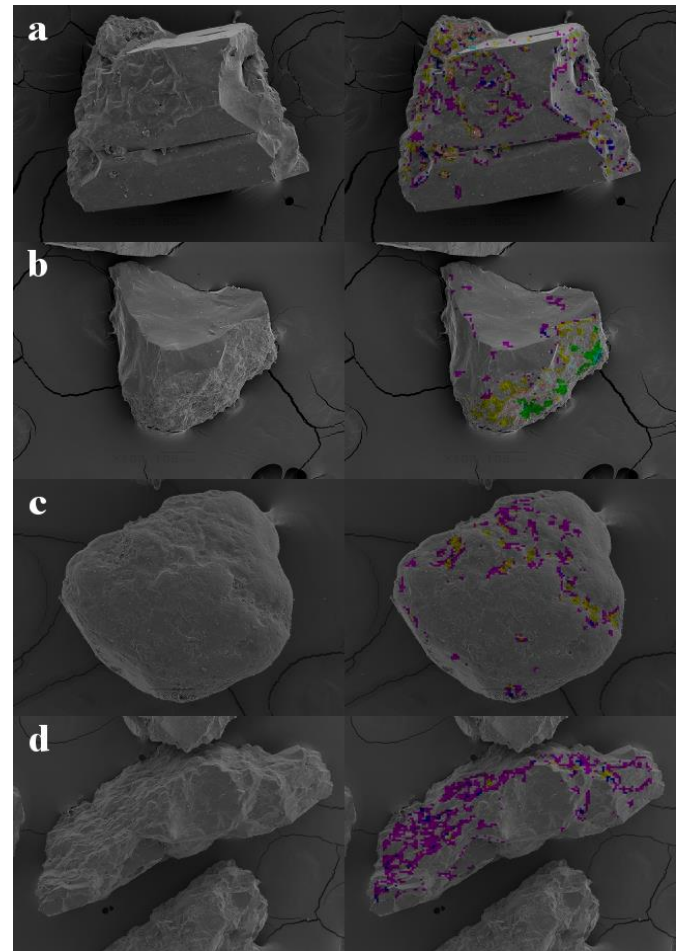


Fig. 7. Example of visualization using the third model: Left side presents the original image; right side highlights the sub-windows, whose texture belongs to the third model.

V. CONCLUSION

The main purpose of this work was to find typical structure patterns of sedimentary grains, which can be described by co-occurrence features. The possibilities of the main co-occurrence features were explored using *K*-means clustering technique instead of a prior definition of textures and utilization of some supervised machine learning techniques. The reason was that the structure forms defined by geomorphologists cannot be easily extracted from images using computers because of their complex nature. Thus the feature space of co-occurrence features was examined to find typical subspaces representing visually consistent texture, for which *K*-means algorithm was used. By visual inspection of clustering result the typical classes were defined. The separate models were constructed for detection of sharp edges, homogeneous surface and rough surface. The sharp edges positions can be further processed to locate the corners or sharp lines. The parts with frequent detections of homogeneous sub-windows can be considered as smooth plain of surface without significant changes. Frequent detections of rough surface can determine the extensively abraded part of grain. The degree of presence of these three defined structure forms can be then used as input data for the exoscopic analysis.

The future work will be aimed at utilization of extracted texture as a base for more specific texture classification and also for an evaluation of statistical occurrence of these computer extractable surface structures in different geomorphological geneses.

REFERENCES

- [1] L. Křížová, M. Křížek, L. Lisá, Applicability of quartz grains surface analysis to the study of the genesis of unlithified sediments, *Geografie*, vol. 116, no. 1, 2011, pp. 59–78.
- [2] M. Mirmehdi, X. Xie, J. Suri, Handbook of texture analysis, Imperial College Press, 2008, pp. 1-6.
- [3] D. A. Clausi, *K*-means Iterative Fisher (KIF) unsupervised clustering algorithm applied to image texture segmentation, *Pattern Recognition*, vol. 35, no. 9, 2002, pp. 1959-1972.
- [4] Ch. Li, R. Chiao, Multiresolution genetic clustering algorithm for texture segmentation, *Image and Vision Computing*, vol. 21, no. 11, 2003, pp. 955-966.
- [5] R. M. Haralick, K. Shanmugam, I. Dinstein, Textural Features for Image Classification, *IEEE Transactions on Systems, Man and Cybernetics*, vol. 3, no. 6, 1973, pp.610-621.
- [6] R. Jain, R. Kasturi, B. G. Schunk, *Machine Vision*, McGraw-Hill, 1995, pp. 236-238.
- [7] C. M. Bishop, *Pattern Recognition and Machine Learning*, Springer, 2006, pp. 423-430.

Aleš Křupka is currently a student in Ph.D. programme Teleinformatics at Faculty of Electrical Engineering, Brno University of Technology. He is especially interested in image processing and machine learning. His research is aimed to discovering new methods of machine analysis of sedimentary grain images.

Programmable Cellular Automata Encryption Algorithm Implemented in Reconfigurable Hardware

Petre Anghelescu

Abstract — This article presents an encryption system based on the PCA (Programmable Cellular Automata) theory and the implementation in reconfigurable hardware in order to achieve high speed communication for real time applications. The proposed encryption algorithm belongs to the class of symmetric key and the entire model was implemented on a reconfigurable hardware in FPGA (Field-Programmable Gate Arrays) device of type Spartan 3E XC3S500E in order to take the full advantage of the inherent parallelism of the PCA. Based on PCA state transitions certain fundamental transformations are defined which represents block ciphering functions of the proposed enciphering scheme. The experimental results prove that the proposed enciphering scheme provides high speed, good security and it is ideally for hardware implementation in FPGA devices.

Keywords—Block ciphers, Cellular automata, Cryptography, Programmable cellular automata, Reconfigurable hardware.

I. INTRODUCTION

Data security for many internet based applications is becoming more and more important with the rapid growth of the quantity of the information transmitted using network communications.

In present, promising applications for cryptographic algorithms may be classified into two categories: *processing of large amount of data at real time* (potentially in a high speed network) – examples include telephone conversations, telemetry data, video conferencing, streaming audio or encoded video transmissions and so forth – and *processing of very small amount of data at real time* (in a moderately high-speed network transmitted unpredictably) – examples include e-commerce or m-commerce transactions, bank account information, e-payments and micro-browser-based (WAP-style), HTML page browsing and so forth. In both cases, cryptography is the best solution against the unauthorized use of the information.

In the recent years, researchers have remarked the similarities between bio-inspired systems – as cellular automata (CAs), chaos and cryptography [1], [2]. Several of

the CAs features can be correlated with the cryptographic properties. A relevant relationship between cellular automata and cryptography was revealed by Shannon in his fundamental early work [3]. In [3], Shannon discusses about a system composed from simple components that interact between them – with a transparent local compartment – but the global compartment of the entire system unsuspected, things that are well known in the cellular automata theory.

The essence of the theoretical and practical efforts which are done in this new field is represented by the idea that CAs cryptosystem is capable to have similar performances regarding the classic methods based on computational techniques.

Also, technologic evolution in the field of communication using reprogrammable hardware structures (FPGA and CPLD), gives appropriate solutions for the implementation of the cryptographic modules in high speed applications.

The cryptosystem presented in this paper uses four one-dimensional PCAs arranged in pipeline and a SRAM memory that store the evolution rules used by the PCAs. The entire cryptosystem is implemented in hardware on a FPGA of type Xilinx Spartan 3E XC3S500E and the plaintext/ciphertext is received/transmitted using User Datagram Protocol (UDP) connection.

The paper is organized as follows. The following section presents basic theoretical foundations of the proposed work. We describe some basics of CA, PCA and reconfigurable hardware. Section III shows how the PCA theory was used in order to construct a block encryption technique. In this section it is presented the structure of the entire PCA based encryption system. Section IV contains experimental results and the analysis of results. In this section the proposed encryption method was tested and verified on a FPGA board and using UDP connection protocol. Conclusions and future research directions will end the paper.

II. CONCEPT AND THEORY OF CA, PCA AND RECONFIGURABLE HARDWARE

A. Cellular Automata (CA)

CAs, introduced by J. v. Neumann [4] and further popularized by S. Wolfram [5], are computational models that can perform complex computation with only local information. The simple structure of CA has attracted researchers from different fields of interests and has undergone rigorous theoretical and experimental analysis.

CA represents a particular class of dynamical systems that

Manuscript received October 25, 2012, revised March 08, 2013. This work was supported by CNCSIS UEFISCSU, project number PN II-RU PD 369/2010, contract number 10/02.08.2010.

Petre Anghelescu – University of Pitesti, Department of Electronics, Communications and Computers. Str. Targu din Vale, No. 1, 110040, Pitesti, Arges, Romania. Corresponding author phone: +4 0724193051 and e-mail: petre.anghelescu@upit.ro
doi: 10.11601/ijates.v2i2.12

enable to describe the evolution of complex systems with simple rules, without using partial differential equations. A CA consists of a regular uniform n-dimensional array of cells where every cell can take values either 0 or 1. Each cell evolves in each time step (discrete steps) depending on some combinational logic on itself and its neighbors as shown in Fig. 1.

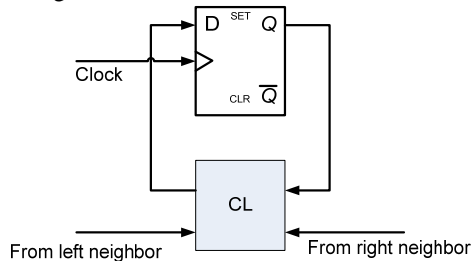


Fig. 1. The component of a cellular automata cell.

Such a CA is called three-neighborhood CA. The combinational logic is called the *rule* of the CA. The next state function for a three-neighborhood CA cell can be expressed as follows:

Say,

i – position of an individual cell in an one dimensional array,

t – time step,

$a_i(t)$ – output state of the central cell (i -th cell) at the t -th time step.

Then,

$$a_i(t+1) = f[a_i(t), a_{i+1}(t), a_{i-1}(t)] \quad (1)$$

where f denotes the local transition function known as a rule of the CA.

In the CA theory, there are two classic types of neighbourhoods: the Moore neighbourhood that comprises 3 cells for one-dimensional CA and 9 cells for two-dimensional CA (Fig. 2a); the von Neumann neighbourhood with 3 cells for one-dimensional CA and 5 cells for two-dimensional CA (Fig. 2b).

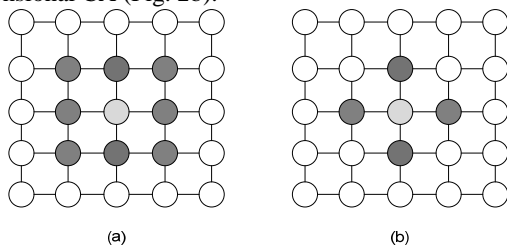


Fig. 2. Classical neighborhood (a) – Moore Neighborhood, (b) – von Neumann Neighborhood

S. Wolfram has studied the relationships between CA and different dynamical systems and suggested a classification of CA behavior in this context. According to [5] there are four classes of CA:

Class I – the CA evolution reaches a certain final state and stays there (limit points).

Class II – the CA encounters simple or cyclic structures (limit cycles).

Class III – the majority of initial states lead to arbitrary patterns (chaotic behavior of the kind associated with strange attractors).

Class IV – generates global complex structures (very long transients with no apparent analog in continuous dynamic systems).

This classification of the CA is done by means of empirical observations and simulations (space-time patterns) and mainly refers to 1-D CAs, but similar ones can be made for 2-D or 3-D cases.

In case of 1-D, three neighborhoods, two states (0 and 1) CA, the number of all possible uniform rules is 2^8 . These rules are enumerated using Wolfram’s naming convention [5] from rule number 0 to rule number 255 and can be represented by a 3-variable Boolean function. Among the rules, rule 51, rule 60 and rule 102 are used in this paper to design the encryption algorithm. The three rules are presented in Table I.

TABLE I
AN EXAMPLE OF CA NUMBERING RULES

Rules name	7 111	6 110	5 101	4 100	3 011	2 010	1 001	0 000
51	0	0	1	1	0	0	1	1
60	0	0	1	1	1	1	0	0
102	0	1	1	0	0	1	1	0

Each CA rule corresponds to a unique combinational logic. For example, using Veitch-Karnaugh diagram, rule 60 specifies an evolution from the neighborhood configurations to the next state as:

$$\text{Rule 60: } a_i(t+1) = a_i(t) \oplus a_{i-1}(t). \quad (2)$$

That is, the next state of the i th is obtained by XORing the present states of the current cell and its left neighbor. In this case, XOR yields true if exactly one, but not both, of two conditions is true.

In a CA, different cells may have different evolution rules. If all cells have the same CA rule, then this CA is called a uniform CA; otherwise it will be called a hybrid CA. If all cells rules involve XOR or XNOR only, like rule 60, then this CA is called additive CA. If in a CA the rules only involve XOR operation, then it is called a non-complemented CA and the corresponding rules are referred to as non-complemented rules. If the rules only involve XNOR operations, then the CA is called a complemented CA. The corresponding rules are called complemented rules.

B. Programmable Cellular Automata (PCA)

The programmable cellular automata (PCA) was firstly introduced in [6] and are modified CA structures, where the combinational logic of each cell is not fixed but controlled by a number of control signals such that different functions (evolution rules) can be realized on the same structure. As the matter of fact, PCA are essentially a modified CA structure. We can say that a CA is a PCA if it employs some control signals that implement various functions dynamically in terms of different rules.

For example, using such a cell structure as in Fig. 3, all possible non-complemented additive rules can be achieved through the combinations of the control signals of C_1 , C_2 and C_3 switches.

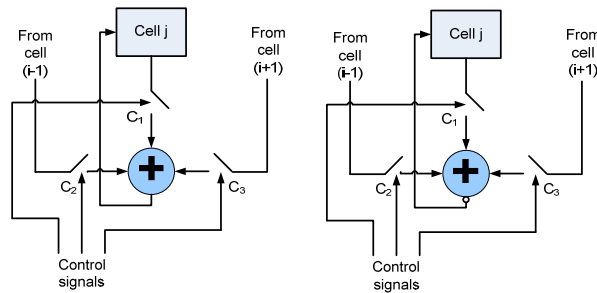


Fig. 3. An example of a cell of PCA.

In this paper one dimensional PCA defined over binary state alphabet (state 0 or 1) with neighborhood size three and dynamically combination of rules 51, 60 and 102 is used.

In conclusion, the very large phenomenology of the CA and PCA models, its apparently big complexity and parallel, regular, cascable and local interconnections (however, this parallelism, when emulated in software or in sequential hardware, disappears) offer a good basis for applications in cryptography.

C. Reconfigurable Hardware

The reconfigurable devices, firstly introduced by G. Estrin in 1960, consist on a hybrid machine composed by a general purpose microprocessor interconnected with programmable logic devices [7].

The most popular reconfigurable hardware devices are FPGAs. FPGA circuits represent a compromise between circuits with microprocessor and ASIC (Application Specific Integrated Circuits) circuits [8]. *On one hand*, they present flexibility in programming, called here reconfiguration, which is a feature for microprocessors. Even if FPGA cannot be programmable while operation, they can be configured anytime is needed, having a structure based on RAM programmable machines. *On the other hand*, they allow parallel structures implementation, with response time less than a system with microprocessor.

FPGAs are programmable semiconductor devices introduced by Xilinx in the mid 1980s that are based around a matrix of configurable logic blocks connected via programmable interconnects. A number of tools are available for synthesizing logic designs such as Hardware Description Languages (HDL) Verilog, and especially, VHDL, are the two most widely spread hardware languages.

Cryptographic realizations in hardware offer high speed and bandwidth providing real-time encryption if needed [9], [10]. Besides cryptography, applications of FPGAs can be found in the domains of evolvable and biologically-inspired hardware, network processors, real-time systems, rapid ASIC prototyping, digital signal processing, interactive multimedia, machine vision, computer graphics, robotics, embedded applications, and so forth. In general, FPGAs tend to be a good choice when dealing with algorithms that can benefit from the high parallelism offered by the FPGA fine-grained architecture.

FPGAs offer advantages for reducing time to design, power consumption, flexibility, high-speed and security.

III. PCA ENCRYPTION ALGORITHM

The encryption method proposed in this paper is based on the PCAs that exhibit periodic behavior (each state lies in some cycle). In these cases, their evolution depends essentially of the initial state, but we can say that after a while the initial state is “forgotten”, in sense that the initial state cannot be retrievable through analyses of the current configuration.

The encryption system is composed from four one-dimensional PCA arranged in pipeline. The block diagram of the proposed PCA encryption system is presented in Fig. 4.

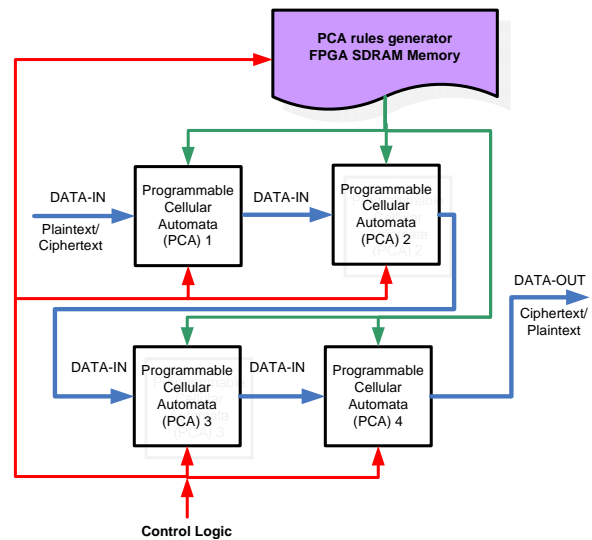


Fig. 4. Block diagram of PCA encryption system.

In the cipher scheme, one 8-bit message block is enciphered by one enciphering function. The PCAs control signals are activated with the help of the signals that are stored in the FPGA SDRAM memory rules. For the sake of simplicity, the enciphering function has four fundamental transformations FTs (PCA = 4) to operate on 8-bit data. It is obvious that for high security applications, more fundamental transformations are to be used.

The block cipher (decipher) procedure can be defined as follows:

1. Load the PCA_1 with one byte plaintext (ciphertext) from I/O. The initial block of the message is the initial state of the PCA_1 . The global configuration of the PCA_4 represents the encrypted message.
2. Load a rule configuration control word from memory rules file into the $PCA_1 \dots PCA_4$.
3. Run the PCA (1, 2, 3 and 4) for 1 ... 7 cycles (in the next paragraph I will explain why must have 1...7 cycles).
4. Repeat steps 2 and 3 for four times.
5. Send one byte ciphertext (plaintext) to I/O (from the PCA_4). If not end of the plaintext (ciphertext) go to step 1. Otherwise, stop the process.

In the block cipher algorithm four 8-cell PCAs are cascaded to form a pipeline CA. With the pipeline, four CA fundamental transformations (FTs) can be performed simultaneously. That means one enciphering function can be done in a single pipeline.

The PCA use for evolution a combination of rules 51, 60

and 102. The rules specify the evolution of the CA from neighborhood configuration to the next state and these are presented, as numerical values, in Table I.

The corresponding combinational logic of rules 51, 60, 102 for PCA can be expressed as follows:

$$\text{Rule 51: } a_i(t + 1) = \overline{a_i(t)}. \tag{3}$$

$$\text{Rule 60: } a_i(t + 1) = a_i(t) \oplus a_{i-1}(t). \tag{4}$$

$$\text{Rule 102: } a_i(t + 1) = a_i(t) \oplus a_{i+1}(t). \tag{5}$$

The PCA configured with the rules 51, 60 and 102 has a state-transition diagram that consists of *equal circles of even length*. As an example, 8-cell PCA with rule configuration <51, 51, 60, 60, 60, 60, 51 and 51> generates cycles as depicted in Fig. 5.

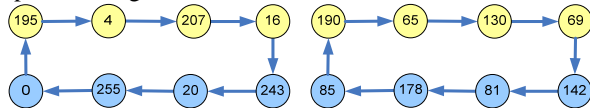


Fig. 5. The state transitions diagram of a non-maximum-length PCA.

Any PCA transformation takes two input parameters. The first one is the seed of the PCA and the second one is the number of clock cycles that needs to be run. We have found that for a PCA with a combination of rules 51, 60 and 102 the initial seed of the PCA reappear after an even number of evolution cycles (see Fig. 5).

In Fig. 5, the PCA has two equal length cycles and each cycle has a cycle length 8. Considering this PCA as an enciphering function and defining a plaintext as its original state it goes to its intermediate state after four cycles which is enciphering process. After running another four cycles, the intermediate state returns back to its original state which decipheres ciphertext into plaintext ensuring deciphering process.

Table II shows the number of 8-cell CA configurations, each generates cycles of length 2, 4, 8 or 16.

TABLE II
CA HAVING EVEN CYCLES LENGTH

Rules applied to cells	8-cell CA having 2 length cycles	8-cell CA having 4 length cycles	8-cell CA having 8 length cycles	8-cell CA having 16 length cycles
	51, 60 (or 102)	7	327	156

In this encryption algorithm are used only the configurations of the rules that generates cycles of length 8. So the system designer is free to take any number in the 156 combinations (see Table II) to enhance the security of the system. The rules with 8-cycle length are presented in detail in my previous papers [11] and [12].

The proposed PCA encryption method has many differences in main concepts in comparing with previous proposed methods [11], [12]. One of the main differences is the nature of method. In the proposed encryption algorithm, we have four PCA's arranged in pipeline in order to achieve good security, but in [11] and [12] we have only one PCA. Also, the communication interface was serial RS232 and here we use TCP/IP connection (UDP protocol) in order to

achieve high speed and encrypt/decrypt data sent over the Internet.

Because of the fact that the PCA does not generate sequences of maximum-length for all the possible combinations (512) of the rules we must apply from the FPGA RAM memory only the combinations (156) that generate cycles of length 8.

As is presented in my previous paper [13] and according with the CA theory, a single basic PCA cell was designed (as is depicted in Fig. 6).

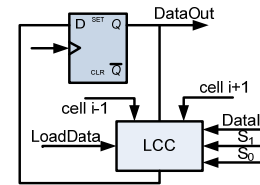


Fig. 6. The structure of the PCA cell.

The cell consists of a D flip-flop and a logic combinational circuit (LCC). The LCC includes multiplexers and XNOR logic gates to implement the rules of CA and to control the loading of data and operation of the CA. When the load control signal (LoadData) is "logic 1", data is loaded into D flip-flop. When LoadData is "logic 0", data is run into the cell according to the rules applied to the rule control signals (S1, S0) and the states of neighborhoods. After an established number of cycles (1 to 7), the data on the Q output of the flip-flop is sent out and new data is loaded in.

In this research are connected together eight cells in order to build an 8-cell PCA as is presented in Fig. 7.

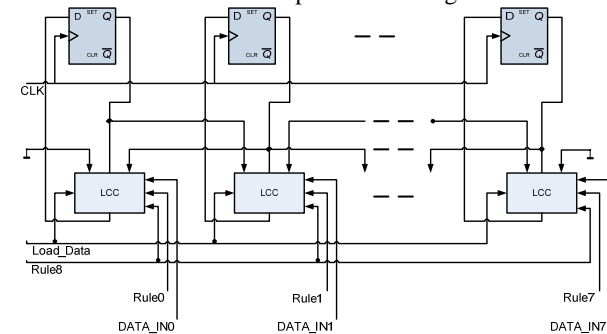


Fig. 7. PCA structure.

We note that the PCAs evolution rules must be downloaded into the FPGA RAM memory before start the encryption/decryption process. When the encryption process begins, rules are read out in sequence and applied to the four pipelined PCAs.

IV. TESTING, RESULTS AND SECURITY ANALYSIS

The general structure of the system is presented in Fig. 8.

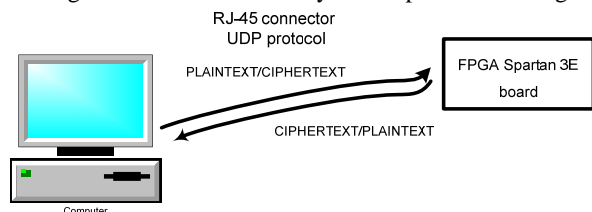


Fig. 8. General system architecture.

The hardware project implements the four pipelined PCA, the memory for storing the evolution rules and the UDP protocol (Fig. 9).

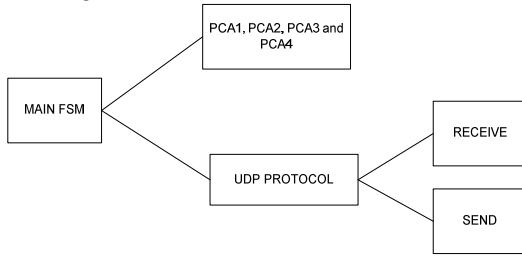


Fig. 9. Hardware design.

The PCA encryption system was implemented in hardware in a Spartan 3E XC3S500E FPGA board from Xilinx [14] (Fig. 10).



Fig. 10. Spartan 3E XC3S500E FPGA.

In hardware, the PCA cryptosystem was developed using VHDL, which is a standard language for hardware description. Using VHDL we tested the application modules in order to verify that the results obtained through software programming (using C# language) agree with hardware simulation. Because a lot of simulation and research has been carried out using 8-bit PCAs in this research, an 8-bit four PCAs was chosen for our design.

The FPGA board is interfaced with a host computer using RJ-45 connector and using UDP protocol (see Fig. 11).



Fig. 11. The application of the encryption system.

The UDP allows high speed data transfer from the PC to the cryptosystem. The message split into 1KB packages is sent to the FPGA board using the UDP client – server connection (Fig. 12)

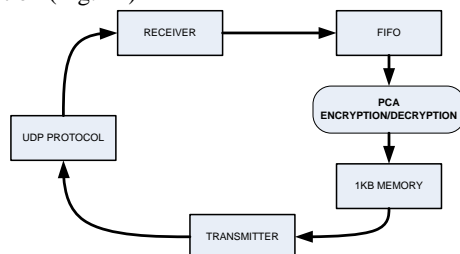


Fig. 12. UDP protocol.

As the bytes reach destination they are immediately encrypted using the correspondent bytes of the PCA's state and then saved into the 1KB RAM memory of the board. In the FPGA, the message received is treated character by character as we explained above and the encryption/decryption dates are sent by the FPGA to the PC to be displayed and stored. In hardware, the encryption rules are downloaded to the RAM before encryption. When the encryption process begins, rules are read out in sequence and sent to the PCA. The process of read of the RAM rules does not introduce delays in the process of encryption because are read in parallel with the encryption of a block of message.

An illustrative example for the encryption-decryption process applied to a short text file is presented in Fig. 13.

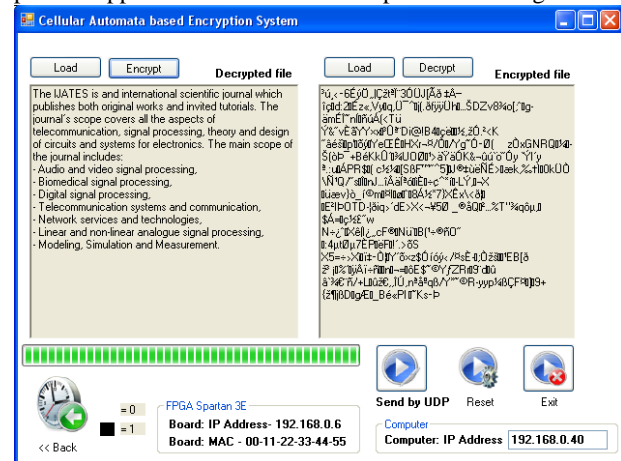


Fig. 13. Spartan 3E XC3S500E FPGA.

It is relevant to note that the distribution of the encrypted text is uniform in all ASCII intervals and not only in zone of alphanumeric intervals (as is depicted in Fig. 14 and Fig. 15).

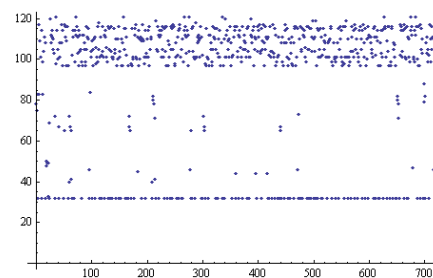


Fig. 14. Plaintext distribution.

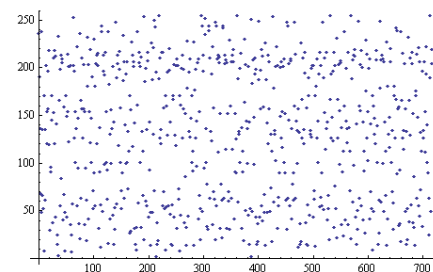


Fig. 15. Ciphertext distribution.

On x-axis we have the number of characters that compose the message (plaintext in Fig. 14 and ciphertext in Fig. 15), and on y-axis we represent the distribution of the

plaintext/ciphertext.

The PCA encrypted sequences was tested using a set of 16 statistical tests conceived by the National Institute of Standards and Technology (NIST) [15]. The NIST test generates probabilistic results with respect to some characteristics that describe the pseudo-random number generators. The encrypted sequences pass the NIST tests and the system is accepted as possible random.

The timing analyzer was used to determine the maximum operating frequency (approximately 5Mbps at 50MHz FPGA – XC3S500E). To improve this value further application can use larger RAM memories in order to store more encrypted UDP packages into the FPGA before starting back to PC transmission phase.

V. CONCLUSIONS AND FUTURE RESEARCH DIRECTIONS

The paper presents a symmetric key block encryption algorithm based on PCA theory. The main contribution is the design, the implementation and the analysis of the pipelined PCA encryption algorithm in reconfigurable hardware using UDP communication protocol.

As PCA achieves high parallelism and only local interconnections we simplify the implementation and with low cost. Also, the encryption and decryption devices share the same module, and could be implemented efficiently in hardware due to simple structure of PCA.

A prototypal hardware realization of this module was realized and described, and the modules presented are programmed by means of a VHDL language.

Future works include larger storage memories (for higher speed), more flexible parameters for system initialization and the implementation in FPGA of both UDP and TCP/IP protocol (for increased transmission safety).

REFERENCES

- [1] A. Fuster-Sabater, P. Cabalero-Gil, "Chaotic Cellular Automata with Cryptographic Application", 9th International Conference on Cellular Automata for Research and Industry, Springer-Verlag Berlin Heidelberg, LNCS 6350, pp. 251–260, 2010.
- [2] C. S. Rao, S. R. Attada, M. J. Rao, K. N. Rao, "Implementation of object oriented encryption system using layered cellular automata", *International Journal of Engineering Science and Technology (IJEST)*, ISSN : 0975-5462, Vol. 3, No. 7, July 2011, Available: <http://www.ijest.info/docs/IJEST11-03-07-163.pdf>.
- [3] C. Shannon, "Communication Theory of Secrecy Systems", *Bell Sys. Tech. J.* 28, pag. 656–715, 1949, Available: netlab.cs.ucla.edu/wiki/files/shannon1949.pdf.
- [4] J. von Neumann, *Theory of self-reproducing automata*, edited and completed by Burks, A.W. (Ed.), Univ. of Illinois Press, London, 1966.
- [5] S. Wolfram, *A new kind of science*, Wolfram Media Inc., ISBN: 1-57955-008-8, 2002.
- [6] S. Nandi, B. K. Kar, P. P. Chaudhuri, "Theory and applications of cellular automata in cryptography", *IEEE Transactions on Computers*, 43(12), 1994, pp. 1346-1356.
- [7] A. Menezes, P. Oorschot, and S. Vanstone. *Handbook of applied cryptography*, CRC Press, ISBN: 0-8493-8523-7, 1996.
- [8] T. Fogarty, J. Miller, and P. Thompson, "Evolving digital logic circuits on Xilinx 6000 family FPGAs," in *Soft Computing in Engineering Design and Manufacturing*, P.Chawdhry, R. Roy, and R. Pant (eds.), Springer: Berlin, pp. 299–305, 1998.
- [9] E. Jamro, P. Russek, A. Dabrowska-Boruch, M. Wielgosz, "The implementation of the customized, parallel architecture for a fast word-match program", *International Journal of Computer Systems Science and Engineering*, Volume 26, Issue 4, pp. 285-292, 2011.
- [10] F. Rodriguez-Henriquez, N. A. Saqib, A. Diaz-Perez, C.K. Koc. *Cryptographic algorithms on reconfigurable hardware*, Springer – Verlag, ISBN 978-0-387-33883-5, 2007.
- [11] P. Angheliescu, S. Ionita, E. Sofron, "Encryption technique with programmable cellular automata (ETPCA)", *Journal of Cellular Automata*, ISSN 1557-5969, Volume 5, Issue 1-2: 79-106, 2010.
- [12] P. Angheliescu, S. Ionita, E. Sofron, "FPGA implementation of hybrid additive programmable cellular automata encryption algorithm", The 8th International Conference on Hybrid Intelligent Systems, HIS 2008, pp. 96-101, 2008.
- [13] P. Angheliescu, "Security of Telemedical Applications over the Internet using Programmable Cellular Automata", *International Journal of Intelligent Computing Research, IJICR*, Volume 3, Issue 1/2, ISSN: 2042–4655, pp. 245-251, 2012.
- [14] Spartan 3E Starter kit board data sheet downloaded from http://www.xilinx.com/support/documentation/boards_and_kits/ug23_0.pdf.
- [15] A. Rukhin, J. Soto, J. Nechvatal, M. Smid, E. Barker, S. Leigh, M. Levenson, M. Vangel, D. Banks, A. Heckert, J. Dray, S. Vo, "A Statistical Test Suite for Random and Pseudo-Random Number Generators for Cryptographic Applications", NIST (National Institute of Standards and Technology) Special Publication 800-22, (2005&2010), <http://csrc.nist.gov/rng/>.

Precision Full-Wave Rectifiers with Current Active Elements and Current Biasing

L. Langhammer and J. Jerabek

Abstract— This article discusses universal precision rectifiers using current active elements and current sources for diode excitation. The paper introduces a circuit solution of the universal precision full-wave rectifier with intention to reduce the negative effect of diode reverse recovery time. Furthermore, experimental results are given and a comparison of the new circuit of precision full-wave rectifier and its known variant is presented.

Keywords—Current conveyor, Diode reverse recovery time, Rectifiers, UCC

I. INTRODUCTION

Precision rectifiers are important building blocks for signal processing and instrumentation of low level signals. The basic problem of conventional precision rectifiers based on diodes and operational amplifiers is that during the transition of diodes from their non-conduction state to their conduction state the operational amplifiers have to recover with a finite small signal, which leads to a significant distortion during zero crossing of the input signal. [1]

Recently, articles describing circuits using active elements operating in a current or mixed mode have appeared. We can mention as examples current conveyors (CC) [2-5], operational transconductance amplifiers (OTA) [6], current followers (CF) [7], digitally adjustable current amplifiers (DACA) [8, 9] and their multiple-output variants such as UCC [3, 4, 5], MOTA [10, 11], MO-CF [11], etc. Using these elements instead of the common operational amplifiers, we can obtain wider bandwidth, improve the signal-to-noise ratio, achieve a higher precision of the output rectified signal and decrease the energy consumption.

The paper [12] describes the bridge rectifier with two conveyors connected as a voltage-to-differential current converter. The issue of temperature sensitivity and sensitivity to small changes of voltage biasing are also solved. Rectifiers which use for their function current followers and operate in the current mode are described in [7]. In this case, a double output current follower (DOCF) and four diodes are used. The problem of small input signals

can be solved by employing an additional voltage follower on the input of the circuit, which provides the high input impedance of the described rectifier. Furthermore, it is possible to come across rectifiers consisting of operational transconductance amplifiers in [6]. The bandwidth of presented circuit is 50 kHz. This circuit does not use diodes and is based on four or five OTA.

We can find one of the basic scheme of full-wave precision rectifier in [1, 13]. The described circuit is the high-frequency precision rectifier consisting of two second-generation current conveyors connected in a form of differential voltage-to-current converter and uses four diodes for its function. In case of small signals at zero crossing transition portion, when the diodes are closed, the differential voltage-to-current converter turns into a high gain voltage differential amplifier. A modified circuit of the high-frequency precision rectifier using the current biasing for diodes proposed in [12] is described in [14]. Another possible solution of the precision full-wave rectifier can be found for example in [15-18].

II. EFFECT OF THE DIODE REVERSE RECOVERY TIME ON PRECISION RECTIFICATION

One of the major factors limiting the use of diodes for high-frequency signals is the diode reverse recovery time. This time can be described as the transition time of the diode from its open state to the closed state. [14, 19] A simple subcircuit with two diodes, which is shown in Fig. 1) is used for the majority of precision rectifier circuits using current diode excitation.

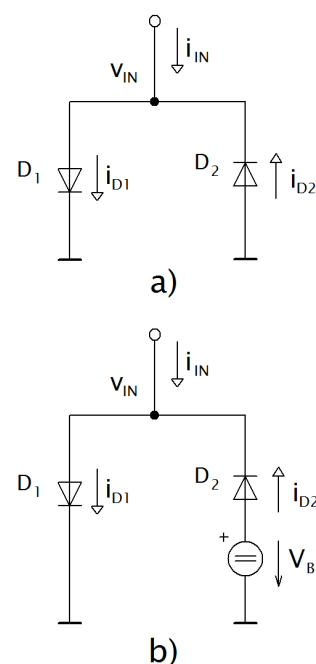


Fig. 1. Subcircuit with current excited diodes b) subcircuit with bias

Manuscript received March 25, 2013.

L. Langhammer Faculty of Electrical Engineering and Communication, Brno University of Technology, Technicka 12, 616 00 Brno, Czech Republic (e-mail: xlangh01@stud.feec.vutbr.cz)

J. Jerabek Faculty of Electrical Engineering and Telecommunication, Brno University of Technology, Technicka 12, 616 00 Brno, Czech Republic (e-mail: jerabekj@feec.vutbr.cz)

When the polarity of the input current is changing the diode stays for a short time in the conductive state even during the opposite polarity, which results in an overshoot of the diode current into the reverse polarity, as shown in Fig. 2). Rising frequency increases the negative effect of the diode reverse recovery time and this leads to increasing distortions of rectified signal. This is due to the fact the semiconductor diode is a non-ideal component. The duration of this period depends on the physical parameters of the diodes respectively on the material from which the diode is made and on its technological performance. Each P or N type of semiconductor contains not only majority carriers but also minority carriers of the opposite polarity. P-N junction remains open for these minority carries during the reverse polarity, therefore, the diode still conducts current until the exhaustion of the minority carriers and then the reverse current decreases to a minimum value.

The diode reverse recovery time t_k can be divided into periods t_s and t_d . During the period t_s the minority carriers are discharged from P-N junction and an almost constant voltage remains on the diode. This voltage is slightly smaller than the forward voltage. This period is followed by the period t_d . In time t_d , the parasitic capacitance of diodes is being charged. After this time, the voltage on the diode remains at the value of the reverse voltage. We can reduce the time t_s by increasing the reverse current flowing through the diode, but this causes a greater overshoot when the polarity changes. [14]

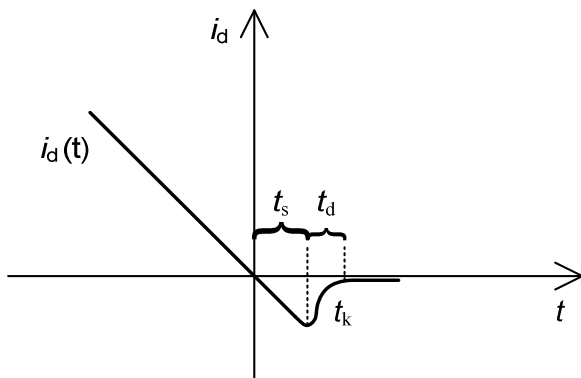


Fig. 2. Detail of the diode current i_d during zero crossing of the input signal

We can obtain a shorter time t_d by modification of the circuit, when we add a voltage source V_B as it can be seen in Fig. 1 b). This modification set diodes during the zero crossing of the input current at the border of their conductive state, thereby it reduces the changes of the voltage at the input node when the input current changes. However, higher bias results into increasing of the current which flows through diodes around the region where the input current changes its polarity. Therefore, the value of the bias for diodes must be set as a compromise between overshoot to opposite polarity of the current flowing through diodes and increasing of the diode zero crossing input current.

III. UNIVERSAL PRECISION FULL-WAVE RECTIFIER WITH CURRENT BIASING

A. Description of the Universal Precision Full-Wave Rectifier

One of the basic precision rectifier circuits which can be found for example in [20] can be seen in Fig. 3 a). The circuit consists of a half-wave rectifier based around the first operational amplifier and a summing amplifier formed by the second operational amplifier. The half-wave rectified current flows through D_2 on a positive half cycle of the input signal v_{IN} . This signal is summed in the summing amplifier with the input signal having relative weights set according to values of resistors $R_4 = R/2$ and $R_1 = R_2 = R_3 = R_5 = R$ resulting in a full-wave rectified signal on the output. Generally, this type of circuit works well at low frequencies, but produces a large waveform distortion at frequencies higher than 1 kHz. This is due to the fact that at the transition point of the input signal, the diodes are closed and the operational amplifier operates in an open-loop configuration. As the input signal frequency increases, limited slew rate more prevents the OA from switch diodes rapidly which leads to a distortion of the output signals. [20]

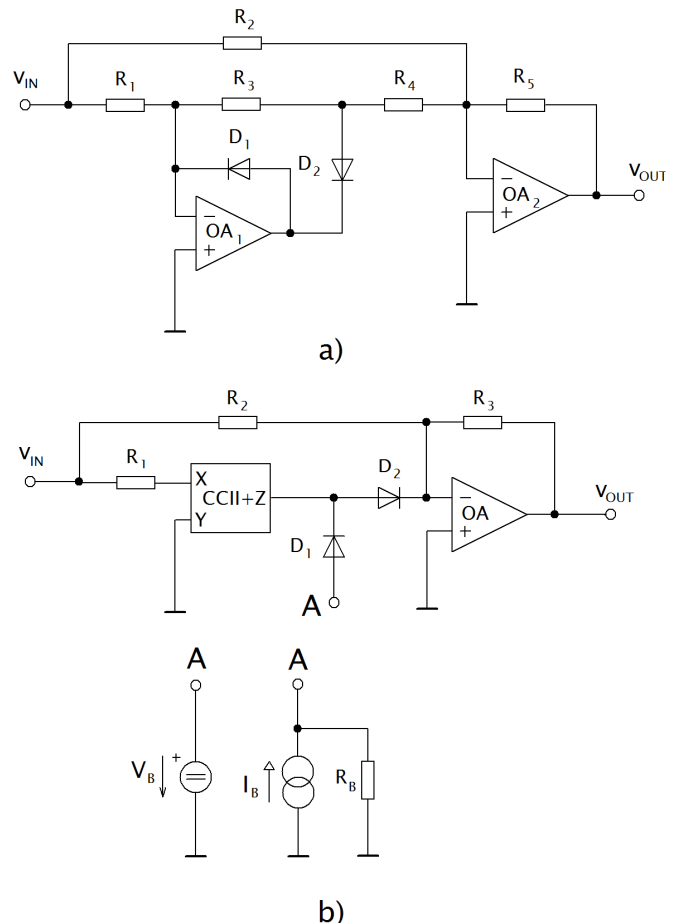


Fig. 3. Universal precision full-wave rectifier a) based on operational amplifiers, b) based on current conveyor and a voltage or current source for bias

This issue can be solved by circuit modifications from Fig. 3 b), when a part of the circuit which operates as the half-wave rectifier is replaced by one with a larger bandwidth. This can be achieved by replacing the operational amplifier by a second generation current conveyor. The high output impedance of the current

conveyors helps overcome the turn-ON resistance of the diodes, so the circuit operates at higher frequencies. Signal weights are again set according to the values of resistors when $R_2 = R_3 = R$ and $R_1 = R/2$ which gives a full-wave rectified signal on the output. As can be seen in Fig. 3 b), the circuit with the current conveyor is supplemented with a voltage source or current source and resistor for biasing to set the diodes close to their open state.

The transfer function for this circuit is given by

$$v_{OUT} = -|v_{IN}|, \quad (1)$$

when

$$R_1 + r_X = \frac{R}{2}, \quad (2)$$

where r_X is the equivalent resistance at the current input of the current conveyor.

In case when the voltage source is used to bias the diodes, the circuit is temperature-sensitive. Another disadvantage of a rectifier with this type of biasing is its sensitivity to small variations of bias voltage which are displayed and the offset voltage appears at the output. A higher temperature stability can be achieved by using a DC current source to bias the diodes. The output offset voltage is easily controlled and adjusted to its minimal level. [12] Therefore, the next proposal considers using current sources to bias diodes.

B. Proposal and Experimental measurements

The proposed circuit can be seen in Fig. 4. It uses the design of a circuit modification for bias taken from [12] and modified for universal precision full-wave rectifier. The modification involves an addition of two current sources, two diodes, and two operational amplifiers, where OA_2 is working as a voltage follower and OA_3 as a current-to-voltage converter. This circuit works properly only in voltage mode. When the OA_3 is omitted simulations show the circuit is supposed to work also in a mixed and current mode. The bias current flows through the diodes D_3 and D_4 and produces a voltage drop across them. This voltage is then fed into a voltage follower. Residual current flowing through D_1 and D_2 creates a voltage drop across these diodes and as a result the diodes are set close to the open state. The current is then diverted through another current source to ground, so it is possible to set the zero offset of the output signal.

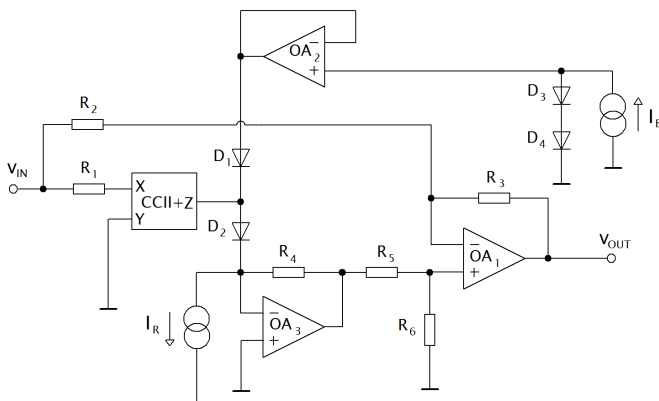


Fig. 4. Proposed circuit of the universal precision full-wave rectifier with current biasing

The summing operational amplifier is replaced by a differential amplifier to achieve a proper operation of the circuit. Resistances are set $R_2 = R_3 = R_4 = R_5 = R_6 = R$ and $R_1 = R/2$. This circuit was implemented in the form of printed circuit board and experimental measurements were carried out to verify its function. For the implementation the transconductance operational amplifier OPA861 [21] was used as the current active element and THS4052C [22] as the operational amplifier, diodes of type 1N4148 and resistors of values $1\text{ K}\Omega$ and $470\ \Omega$ were used. For illustration a comparison of the basic universal precision full-wave rectifier from Fig. 3 b) and the proposed circuit is presented. For the basic circuit a voltage source of value $V_B = 0.6\text{ V}$ is used to bias the diodes. In case of the proposed circuit, the biasing current I_B and residual current I_R are both set to $40\ \mu\text{A}$. In Fig. 5 a) shows the output rectified signals for the input signal frequency of 1 MHz and the amplitude of 1 V . Figure 5 b) shows a comparison of output rectified signals with the same input frequency when the amplitude of the input signal was 0.2 V . From the output waveforms it can be seen that the proposed circuit achieves significantly better results for signals with smaller amplitudes than the basic circuit.

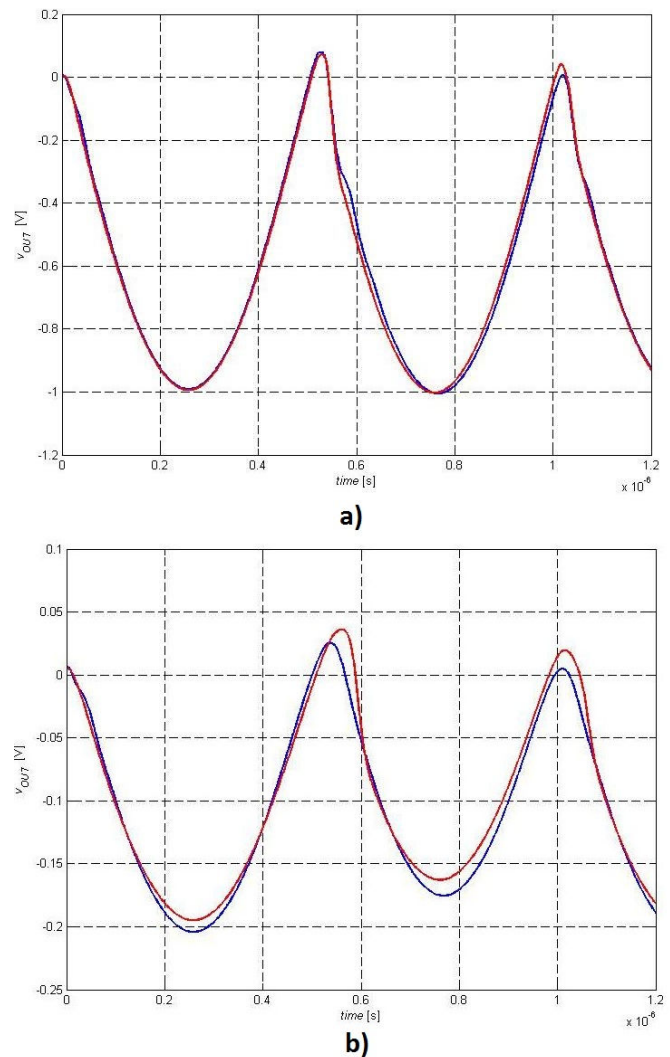


Fig. 5. Measured output waveforms of proposed circuit (blue line) and basic circuit from fig. 3b (red line) when input signal frequency was 1 MHz and amplitude a) 1 V , b) 0.2 V

Fig. 6) shows a comparison of the transfer function of implemented circuits. As can be seen the transfer function does not follow the expected gradient during the positive half-cycle due to the parasitical resistance r_X of the conveyor's current input. This negative effect is not so significant for the proposed circuit.

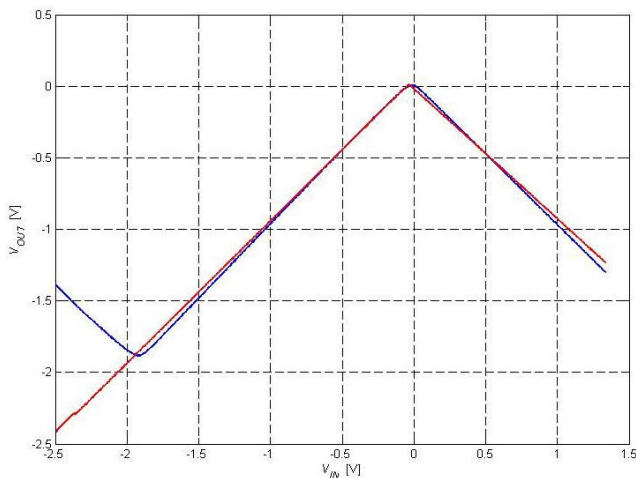


Fig. 6. Measured DC transfer functions proposed circuit (blue line) and basic circuit from Fig. 3b (red line)

From Fig. 7) it is possible to compare the details of the transfer function of the proposed circuit when using current diode biasing and without bias. This picture shows that the output offset can be set to a minimum value using the current sources to bias the diodes.

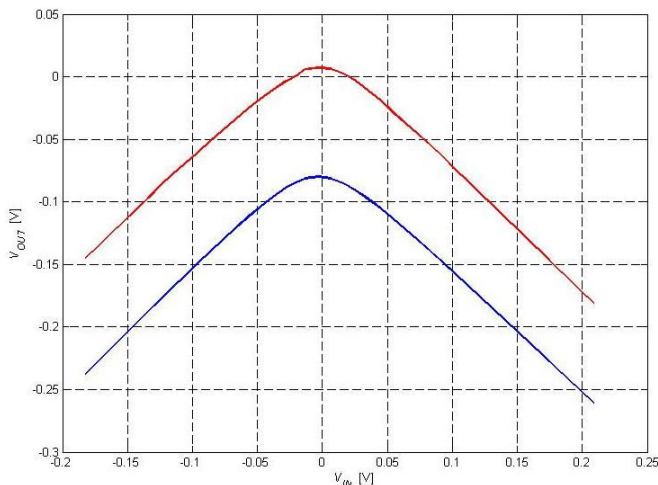


Fig. 7. Detail of DC transfer function around zero crossing of proposed circuit with bias (red line), without bias (blue line)

In conclusion, the DC value transfer p_{DC} has been analyzed to compare the accuracy of circuits. Results are based on simulations of these circuits when the input signal frequency was in the range from 10 kHz to 1 MHz and the amplitude of the input signal was 100 mV. From Fig. 8 can be seen that the proposed circuit gives better results when the frequency is increasing. The DC value transfer is given by (3) [23]

$$p_{DC} = \frac{\int_T y_R(t) dt}{\int_T y_{ID}(t) dt}, \quad (3)$$

where $y_R(t)$ represents the actual rectifier signal, $y_{ID}(t)$ represents the ideally rectified signal and T is the period of the input signal.

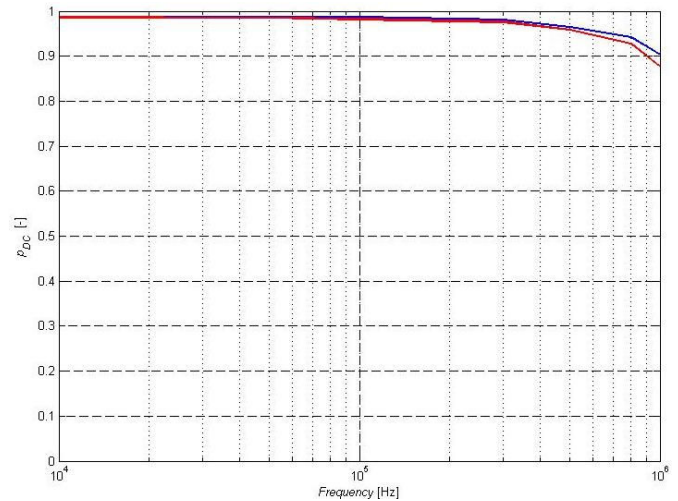


Fig. 8. Measured DC value transfer p_{DC} proposed circuit (blue line) and basic circuit from Fig. 3b (red line)

IV. CONCLUSION

The aim of this work is to propose a circuit solution of the universal precision full-wave rectifier with current sources to bias diodes with an effort to limit the effect of the diode reverse recovery time. The function of the proposed circuit was verified by experimental measurements. The paper compares measured rectified output waveforms, measured DC transfer functions of implemented circuits and DC value transfer p_{DC} based on simulations.

Using the modification of the biasing solution presented in [12] wider bandwidth has been achieved by reducing distortions caused by the negative effect of the diode reverse recovery time. Another advantage of proposed circuit is that the output offset can be easily controlled and set to its minimum level. Better results of the small signal rectification than in case of the basic circuit with a voltage source to bias diodes are also obtained.

REFERENCES

- [1] TOUMAZOU C., LIDGEY F. J., CHATTONG S.: High frequency current conveyor precision full-wave rectifier. IEE 1994, Electronics Letters Online No: 19940539.
- [2] LIU S.L., WU D. S., TSAO H. W., WU J., TSAY J. H.: Nonlinear circuit applications with current conveyors. IEE PROCEEDINGS-G, Vol. 140, No. 1, FEBRUARY 1993.
- [3] SPONAR R., VRBA K.: Measurements and Behavioral Modeling of Modern Conveyors. IJCSNS International Journal of Computer Science and Network Security, VOL.6 No.3A, March 2006.
- [4] VRBA, K., JERABEK J.: Selected features of the universal current conveyor, example of the application design. Elektrevue, 24.10.2006, č. 41, s. ISSN 1213-1539.
- [5] JERABEK, J.; VRBA, K. SIMO type low-input and high-output impedance current-mode universal filter employing three universal current conveyors. AEU - International Journal of Electronics and Communications, 2010, vol. 64, no. 6, pp. 588-593
- [6] JONGKUNSTIDCHAI C., FONGSAMUT C., KUMWACHARA K., SURAKAMPONTORN W. : Full-wave rectifiers based on operational transconductance amplifiers. C. Jongkunsitdchai et al. / Int. J. Electron. Commun. (AEU) 61 (2007) 195 – 201.
- [7] TILIUTE D. E.: Full-wave current-mode precision rectifiers using unity-gain cells. Electronics and Electrical Engineering.- Kaunas: Technologija, 2003. – No. 7(49). – P. 26-29.
- [8] JERABEK J., SOTNER R., VRBA K., KOUDAR I.: Fully differential versatile adjustable filter with current active elements. Elektrevue, 2010/7 – 15. 2. 2010, ISSN 1213 - 1539.
- [9] JERABEK, J.; KOTON, J.; SOTNER, R.; VRBA, K. Adjustable band-pass filter with current active elements: two fully-differential and single-ended solutions. ANALOG INTEGRATED CIRCUITS AND SIGNAL PROCESSING, 2013, vol. 74, no. 1, pp. 129-139.

- [10] JERABEK J., VRBA K.: Novel Universal Filters Using Only Two Current Active Elements, In Proc of Third Int Conf on Systems (ICONS'08), IEEE Computer Society, Cancun, pp. 285-289, 2008.
- [11] JERABEK J., VRBA K., JELINEK M.: Versatile adjustable filter with current followers transconductance amplifiers and a minimum number of components. *Elektrorevue*, 2010/46 - 2. 7. 2010, ISSN 1213 - 1539.
- [12] WILSON B., MANNAMA V.: Current-mode rectifier with improved precision. IEE 1995, *Electronics Letters Online No: 19950185*.
- [13] HAYATLEH K., PORTA S. LIDGEY F. J.: Temperature independent current conveyor precision rectifier. IEE 1994, *Electronics Letters Online No: 199414.54*.
- [14] KUBANEK D., VRBA K.: Precision rectifiers with current excitation of diodes and the effect of the diode reverse recovery time to their function. *Elektrorevue*, 2010/6 – 15. 2. 2010, ISSN 1213 - 1539.
- [15] KOTON J., HERENC SAR N., VRBA K., CICEKOGLU O.: Versatile Precision Full-Wave Rectifier Using Current and Voltage Conveyor, Latest Trends on Circuits, Systems and Signals, ISSN: 1792-4324.
- [16] BURLIAN J., KOTON J., HERENC SAR N.: Universal Voltage Conveyor and Current Conveyor in Fast Full-Wave Rectifier, The International Journal of Advances in Telecommunications, Electrotechnics, Signals and Systems Vol 1, No 2-3, pp. 37-41, 2012, doi: 10.11601/ijates.v1i2-3.8, ISSN: 1805-5443.
- [17] KOTON J., HERENC SAR N., VRBA K.: Current and Voltage Conveyors in Current and Voltage-Mode Precision Full-Wave Rectifiers, *RADIOENGINEERING*, VOL. 20, NO. 1, APRIL 2011.
- [18] KOTON J., HERENC SAR N., VRBA K.: Precision Full-wave Rectifier Using Current Conveyors and Two Diodes, ICN 2012 : The Eleventh International Conference on Networks, ISBN: 978-1-61208-183-0.
- [19] LANGHAMMER, L. Non-linear circuits using current active elements. Brno University of Technology, Faculty of Electrical Engineering and Telecommunication, 2012. 66 s. Supervisor of the master's thesis Ing. Jaroslav Koton, Ph.D..
- [20] GIFT S. J. G., MAUNDY B.: Versatile precision full-wave rectifiers for instrumentation and measurements, Manuscript received December 7, 2005; revised May 3, 2007. Digital Object Identifier 10.1109/TIM.2007.904565.
- [21] Texas Instruments - OPA861 - Wide bandwidth Operational Transconductance Amplifier (OTA) (datasheet). Online, < <http://www.ti.com/product/opa861> >
- [22] Texas Instruments - THS4052 - 70-MHz high-speed Amplifiers (datasheet). Online, < <http://www.ti.com/product/th4052> >
- [23] D. Biolek, V. Biolkova, and Z. Kolka, "AC Analysis of Operational Rectifiers via Conventional Circuit Simulators," *WSEAS Transactions on Circuits and Systems*, vol. 3, no. 10, pp. 2291–2295, 2004.

Novel Robust Optimization and Power Allocation of Time Reversal-MIMO-UWB Systems in an Imperfect CSI

Sajjad Alizadeh and Hossein Khaleghi Bizaki

Abstract— Time Reversal (TR) technique is an attractive solution for a scenario where the transmission system employs low complexity receivers with multiple antennas at both transmitter and receiver sides. The TR technique can be combined with a high data rate MIMO-UWB system as TR-MIMO-UWB system. In spite of TR's good performance in MIMO-UWB systems, it suffers from performance degradation in an imperfect Channel State Information (CSI) case. In this paper, at first a robust TR pre-filter is designed together with a MMSE equalizer in TR-MIMO-UWB system where is robust against channel imperfection conditions. We show that the robust pre-filter optimization technique, considerably improves the BER performance of TR-MIMO-UWB system in imperfect CSI, where temporal focusing of the TR technique is kept, especially for high SNR values. Then, in order to improve the system performance more than ever, a power loading scheme is developed by minimizing the average symbol error rate in an imperfect CSI. Numerical and simulation results are presented to confirm the performance advantage attained by the proposed robust optimization and power loading in an imperfect CSI scenario.

Keywords—MMSE equalizer, Time Reversal (TR) technique, MIMO channel, Ultra-Wideband (UWB) system.

I. INTRODUCTION

Ultra-wide band (UWB) systems have recently received much interest from both research community and industry. One of the main applications of UWB system is its ability of high data rate transmission in indoor environments, where remarkable temporal channel resolution and so, high complexity of the receiver structure, are inevitable [1]-[2]. However, due to the wide bandwidth property, UWB systems suffer from a very long delay spread of multipath channels, especially in indoor environments.

On the other hand, transmission over a Multiple Input Multiple Output (MIMO) channel has been shown as one of the important techniques in modern communications because of its high spectral efficiency [3]. In order to benefit a high data rate system with high spectral efficiency, the UWB system can be used in MIMO channels as MIMO-UWB system. Time Reversal (TR) technique can be used to reduce the long delay spread of the UWB channel. TR can mitigate not only the Inter Symbol Interference (ISI) but also the Multi Stream Interference (MSI) caused by transmitting several data streams, simultaneously [4]-[6]. The main

advantages of the TR technique are: temporal and spatial focusing [6]. In temporal focusing, the received signal is compressed in the time domain. Owing to this property, the ISI caused by the original multipath channel is greatly reduced. Also, in spatial focusing, the received signal is focused on the intended user at some specific position which is determined by the transmitter or user that uses the corresponding channel to pre-filter the intended data signal. In this paper, the TR technique is considered to overcome both MSI and ISI in MIMO spatial multiplexing as a low cost, low power and low complexity receiver solution.

In a MIMO-UWB system, we have $N_T \times N_R$ multipath channels between transmitter and receiver sides, where N_T and N_R denote the number of transmit and receive antennas, respectively. Obtaining the TR pre-coding waveform for the m^{th} transmit antenna and N_R receive antennas is straightforward [4]. First, a sounding pulse is sent through all the N_R antennas from receiver to the transmitter. Second, the received signals at each transmitter antenna are then recorded, digitized, and time reversed. If the sounding pulse is sufficiently short, we can directly use the time-reversed version of received signals as the TR pre-coder. Otherwise, deconvolution effort is necessary to remove the pulse effect from the received sounding signal [4]. Practically, if we use the deconvolution efforts (e.g. CLEAN Algorithm [7]-[8]); some errors may be caused in the channel estimation. In spite of TR's good performance, it is very sensitive to erroneous Channel State Information (CSI). Therefore the improved algorithm should be considered in a TR-MIMO-UWB communication system in imperfect CSI.

Most of the research on TR pre-coding assumes that perfect CSI is given at the transmitter side [5], [9]-[10]. Authors in [5] proposed an antenna selection scheme for TR-MIMO-UWB communication system in a perfect CSI case to reduce the number of transmit antenna. Also, a MMSE equalizer is used for TR-UWB system with perfect CSI in [9] to mitigate the residual ISI and increase transmission data rate. Some power loading schemes are used in [10] for TR-MISO-UWB system with perfect CSI. Unfortunately, these methods suffer from the effects of the imperfect CSI in the transmitter.

On the other hand, the imperfect CSI has been considered in some of the research on TR-MIMO-UWB system, especially in recent years [6], [11]-[14]. The effect of channel imperfection on the TR-MIMO-UWB system performance has been evaluated in [6] for low and high data rate transmissions. Authors of this literature have practically shown that the TR system is almost robust in imperfect CSI where the robustness can be obtained with performance degradation. In the mentioned reference when the noise level

Manuscript received May 27, 2013.

Sajjad Alizadeh is with the Electrical and Electronic Engineering University Complex, Malek Ashtar University of Technology, Tehran, Iran, (e-mail: s.alizadeh@chmail.ir).

Hossein Khaleghi Bizaki is with the Electrical and Electronic Engineering University Complex, Malek Ashtar University of Technology, Tehran, Iran, (e-mail: bizaki@ee.iust.ac.ir).

doi: 10.11601/ijates.v2i2.49

of channel estimation is noticeable, using the TR method cannot yield satisfactory performance. Unfortunately, an optimization scheme has not been provided in this literature to overcome the effects of the channel imperfection. In this paper, we propose a pre-processing method as robust optimization to compensate the estimation error in an imperfect CSI scenario for MIMO-UWB systems.

The robustness of TR technique in imperfect CSI caused by a time varying channel environment has been studied in [11] by experimental results. It has been shown that, if the channel maintains some partial correlation with the previous channel, the TR method can give a good performance even if the total correlation of the channels is very low. But if the correlation of the channels is not available, they have not proposed a theoretical solution for system performance improvement. Also, a post-time-reversed MIMO-UWB transmission scheme has been proposed in [12] which improves the TR robustness against imperfect CSI caused by channel estimation error when compared with the conventional TR scheme. We propose simpler robust optimization schemes, in this paper, with the same attained performance. Also, in our previous works [13]-[14], we had provided the pre-filtering solutions for the channel estimation error compensation by using the channel estimation error covariance matrix for the Single-Input Single-Output (SISO) Time Reversal UWB systems. In this paper, similar approaches (pre-filtering method) with a procedure different from these literatures are used to analysis and improve the TR-MIMO-UWB systems in an imperfect CSI scenario. Therefore, based on mentioned researches on TR pre-coding and also, works of [13]-[16], this paper proposes a novel pre-filter optimization and power allocation scheme at transmitter side to improve the TR-MIMO-UWB system performance in an imperfect CSI scenario.

The rest of the paper is organized as follow; we introduce the system model in Section II. In Section III, a novel robust optimization scheme is derived based on a MMSE equalizer in the TR-MIMO-UWB system. The power adaptation policies optimizing the average symbol error rate performance are derived for imperfect CSI in Section IV. Numerical and simulation results characterizing the performance of the proposed methods are presented in Section V, and finally, conclusions are drawn in Section VI.

II. TR-MIMO-UWB SYSTEM MODEL

The TR-MIMO-UWB system is depicted in Fig. 1 with N_T transmit and N_R receive antennas. Let us consider a UWB system using binary pulse amplitude (BPAM) modulation with pulse shaping according to FCC desired power spectrum density [1]-[2]. The input signal is converted into N_R streams, pre-coded with TR pre-filter, and then sent to N_T transmitting antennas, simultaneously. The resultant signal passes through the multipath MIMO channel and then, is corrupted by an AWGN. Thus, there are $N_T \times N_R$ multipath channel between transmit and receive antennas. For simplicity of analysis, we assume that the maximum length of each channel realization is L [5]-[6]. The TR pre-filter is used in the spatial multiplexing UWB system in order to cope with the ISI and MSI problems. Finally, after passing

the received signal through the MMSE equalizer, the data stream is detected based on a threshold value ν_T .

The effect of channel estimation error can be considered as $\mathbf{H} = \hat{\mathbf{H}} + \Delta\mathbf{H}$ where \mathbf{H} , $\hat{\mathbf{H}}$ and $\Delta\mathbf{H}$ are the true value, estimated value and estimation error of the channel impulse response (CIR), respectively. It is assumed that the entries of $\Delta\mathbf{H}$ are i.i.d. random variables with zero mean complex Gaussian noise. The pre-filter with respect to the estimation errors can be modeled as $\mathbf{H}_T = \hat{\mathbf{H}}_T + \mathbf{F}_C$ where \mathbf{H}_T , $\hat{\mathbf{H}}_T$ and \mathbf{F}_C are the robust TR pre-filter, the conventional TR pre-filter and the compensator pre-filter, respectively. The estimated CIR between i -th transmit antenna and j -th receive antenna can be denoted as

$$\hat{h}_{ij}(t) = \sum_{l=1}^L \hat{\alpha}_l^{ij} \delta(t - \hat{\tau}_l^{ij}) ; i = 1, \dots, N_T, j = 1, \dots, N_R \quad (1)$$

where $\hat{\alpha}_l$ is the estimated amplitude, $\hat{\tau}_l$ is the delay of the l -th tap and L is the maximum delay spread. The discrete time vector form of CIR in reversed order is denoted as: $\hat{\mathbf{h}}_{ij} = [\hat{h}_{ij}[L-1], \dots, \hat{h}_{ij}[1], \dots, \hat{h}_{ij}[0]]_{1 \times L}$. Also the estimation error vector of the CIR is defined as: $\Delta\mathbf{h}_{ij} = [\Delta h_{ij}[L-1], \dots, \Delta h_{ij}[1], \dots, \Delta h_{ij}[0]]_{1 \times L}$ where $i=1, \dots, N_T, j=1, \dots, N_R$ and $l=0, \dots, L-1$. In matrix form we have [5]

$$\hat{\mathbf{H}} = \begin{pmatrix} \hat{\mathbf{h}}_{11} & \hat{\mathbf{h}}_{21} & \dots & \hat{\mathbf{h}}_{N_T 1} \\ \hat{\mathbf{h}}_{12} & \hat{\mathbf{h}}_{22} & \dots & \hat{\mathbf{h}}_{N_T 2} \\ \vdots & \vdots & \ddots & \vdots \\ \hat{\mathbf{h}}_{1N_R} & \hat{\mathbf{h}}_{2N_R} & \dots & \hat{\mathbf{h}}_{N_T N_R} \end{pmatrix}_{N_R \times N_T L}$$

$$\Delta\mathbf{H} = \begin{pmatrix} \Delta\mathbf{h}_{11} & \Delta\mathbf{h}_{21} & \dots & \Delta\mathbf{h}_{N_T 1} \\ \Delta\mathbf{h}_{12} & \Delta\mathbf{h}_{22} & \dots & \Delta\mathbf{h}_{N_T 2} \\ \vdots & \vdots & \ddots & \vdots \\ \Delta\mathbf{h}_{1N_R} & \Delta\mathbf{h}_{2N_R} & \dots & \Delta\mathbf{h}_{N_T N_R} \end{pmatrix}_{N_R \times N_T L}$$

If estimated CIR of all channels $\hat{\mathbf{h}}_{ij}$ are known at the transmitter side, time reversed version of them are used to pre-filter the transmit data. Thus we can construct the pre-filter matrix based on the time reversed form of the estimated channels which is an $N_T L \times N_R (2L-1)$ matrix as [6]

$$\hat{\mathbf{H}}_T = \begin{pmatrix} \overline{\mathbf{H}}_{11} & \overline{\mathbf{H}}_{12} & \dots & \overline{\mathbf{H}}_{1N_R} \\ \overline{\mathbf{H}}_{21} & \overline{\mathbf{H}}_{22} & \dots & \overline{\mathbf{H}}_{2N_R} \\ \vdots & \vdots & \ddots & \vdots \\ \overline{\mathbf{H}}_{N_T 1} & \overline{\mathbf{H}}_{N_T 2} & \dots & \overline{\mathbf{H}}_{N_T N_R} \end{pmatrix}_{N_T L \times N_R (2L-1)}$$

where each sub-matrix $\overline{\mathbf{H}}_{ij}$ is an $L \times (2L-1)$ Toeplitz matrix defined by [6] as

$$\overline{\mathbf{H}}_{ij} = \begin{pmatrix} \hat{h}_{ij}[0] & \dots & \hat{h}_{ij}[L-1] & 0 & \dots & 0 \\ 0 & \hat{h}_{ij}[0] & \dots & \hat{h}_{ij}[L-1] & 0 & \dots & 0 \\ \vdots & \vdots & \ddots & \vdots & \ddots & \ddots & \vdots \\ 0 & \dots & 0 & \hat{h}_{ij}[0] & \dots & \hat{h}_{ij}[L-1] \end{pmatrix}_{L \times (2L-1)}$$

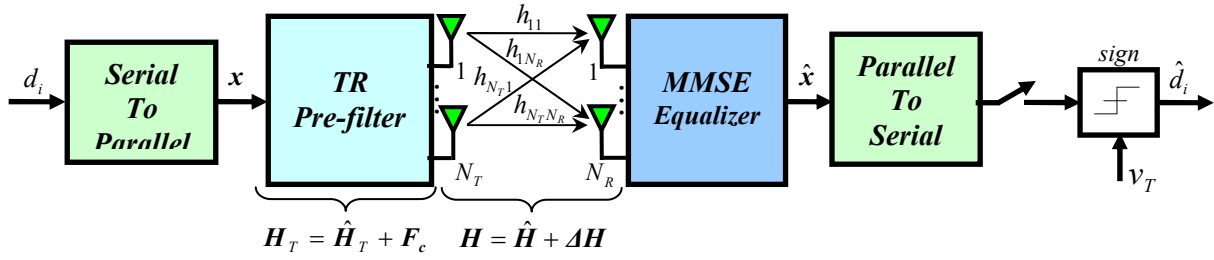


Fig. 1. Block diagram of TR-MIMO-UWB system.

If we define

$$\mathbf{F}_c = \begin{pmatrix} \bar{\mathbf{F}}_{11} & \bar{\mathbf{F}}_{12} & \cdots & \bar{\mathbf{F}}_{1N_R} \\ \bar{\mathbf{F}}_{21} & \bar{\mathbf{F}}_{22} & \cdots & \bar{\mathbf{F}}_{2N_R} \\ \vdots & \vdots & \ddots & \vdots \\ \bar{\mathbf{F}}_{N_T1} & \bar{\mathbf{F}}_{N_T2} & \cdots & \bar{\mathbf{F}}_{N_TN_R} \end{pmatrix}_{N_T \times N_R (2L-1)}$$

then each sub-matrix $\bar{\mathbf{F}}_{ij}$ is an $L \times (2L-1)$ Toeplitz matrix defined by

$$\bar{\mathbf{F}}_{ij} = \begin{pmatrix} f_{ij}[0] & \cdots & f_{ij}[L-1] & 0 & \cdots & 0 \\ 0 & f_{ij}[0] & \cdots & f_{ij}[L-1] & 0 & \cdots & 0 \\ \vdots & \vdots & \ddots & \vdots & \ddots & \ddots & \vdots \\ 0 & \cdots & 0 & f_{ij}[0] & \cdots & f_{ij}[L-1] & 0 \end{pmatrix}_{L \times (2L-1)}$$

The goal is the calculation of the error compensator matrix \mathbf{F}_c with the assumption that the probability distribution of the error coefficients are as: $\Delta h_{ij}[l] \sim CN(0, \sigma_e^2)$. Also, $\mathbf{C}_{\Delta H} = E\{\Delta \mathbf{H}^H \Delta \mathbf{H}\}$ and $E\{\Delta \mathbf{H}\} = 0$ are assumed to be known.

The received symbols vector at the MIMO channel output with TR pre-filter can be written as $\mathbf{y} = \mathbf{H}_{TR} \mathbf{x} + \mathbf{n}$ where

$$\mathbf{x} = \frac{1}{\sqrt{N_T}} [x_1, x_2, \dots, x_{N_T}]^T, \quad \mathbf{y} = \frac{1}{\sqrt{N_R}} [y_1, y_2, \dots, y_{N_R}]^T,$$

$\mathbf{n} = [n_1, n_2, \dots, n_{N_R}]^T$ and $\mathbf{H}_{TR} = \mathbf{H} \mathbf{H}_T$ are the transmitted symbols, the received symbols, AWGN noise and equivalent TR response, respectively. The vector \mathbf{x} contains *i.i.d.* random variables with zero mean $E\{\mathbf{x}\} = 0$ and variance $E\{\mathbf{x} \mathbf{x}^H\} = \sigma_x^2 \mathbf{I}$. For simplicity of analysis, we assume $\mathbf{n} \sim CN(0, \sigma_n^2 \mathbf{I})$, $\sigma_x^2 = 1$ and also, the antipodal modulation is considered.

I. ROBUST TR OPTIMIZATION BASED ON MMSE CRITERION

It is desired to calculate the error compensator pre-filter \mathbf{F}_c in an imperfect CSI with the assumption that the matrices $\hat{\mathbf{H}}$, $\hat{\mathbf{H}}_T$ and $\mathbf{C}_{\Delta H}$ are known. The error vector is considered as the difference between the transmitted symbols and the detected symbols, as $\mathbf{e} = \hat{\mathbf{x}} - \mathbf{x}$. Thus MMSE solution should minimize the cost function $E\{|\mathbf{e}|^2\} = E\{|\hat{\mathbf{x}} - \mathbf{x}|^2\}$ with respect to pre-filter \mathbf{F}_c . For simplicity of analysis we use the orthogonality principle, instead of the MMSE solution [15]. In this case, the orthogonality principle can be considered as $E\{\mathbf{e} \mathbf{x}^H\} = 0$ in which we obtain $E\{\hat{\mathbf{x}} \mathbf{x}^H\} = E\{\mathbf{x} \mathbf{x}^H\}$.

By considering the MMSE equalizer in the receiver side, the estimated symbol $\hat{\mathbf{x}}$ can be expressed as [9]

$$\hat{\mathbf{x}} = (\mathbf{H}_{TR}^H \mathbf{H}_{TR} + \frac{1}{\rho} \mathbf{I})^{-1} \mathbf{H}_{TR}^H \mathbf{y} \quad (2)$$

where $\rho = \frac{\sigma_x^2}{\sigma_n^2}$ is the signal to noise ratio. By using (2), the

cross-correlation between the estimated and the transmitted symbols can be calculated as

$$E\{\hat{\mathbf{x}} \mathbf{x}^H\} = \sigma_x^2 E\{(\rho \mathbf{H}_{TR}^H \mathbf{H}_{TR} + \mathbf{I})^{-1} (\rho \mathbf{H}_{TR}^H \mathbf{H}_{TR})\} \quad (3)$$

Because $\rho \mathbf{H}_{TR}^H \mathbf{H}_{TR}$ is symmetric, we can use the following approximation [17]

$$(\rho \mathbf{H}_{TR}^H \mathbf{H}_{TR})(\rho \mathbf{H}_{TR}^H \mathbf{H}_{TR} + \mathbf{I})^{-1} \cong \frac{1}{\rho^2} (\mathbf{H}_{TR}^H \mathbf{H}_{TR})^{-2} - \frac{1}{\rho} (\mathbf{H}_{TR}^H \mathbf{H}_{TR})^{-1} + \mathbf{I} \quad (4)$$

Thus, by using the above approximation, (3) can be written as

$$E\{\hat{\mathbf{x}} \mathbf{x}^H\} = \frac{\sigma_x^2}{\rho^2} E\{(\mathbf{H}_{TR}^H \mathbf{H}_{TR})^{-2}\} - \frac{\sigma_x^2}{\rho} E\{(\mathbf{H}_{TR}^H \mathbf{H}_{TR})^{-1}\} + \sigma_x^2 \mathbf{I} \quad (5)$$

As a result, based on the orthogonality principle, i.e., $E\{\hat{\mathbf{x}} \mathbf{x}^H\} = E\{\mathbf{x} \mathbf{x}^H\}$ we obtain

$$E\{\mathbf{H}_{TR}^H \mathbf{H}_{TR}\} = \frac{1}{\rho} \mathbf{I} \quad (6)$$

where $\mathbf{H}_{TR} = \hat{\mathbf{H}} \hat{\mathbf{H}}_T + \hat{\mathbf{H}} \mathbf{F}_c + \Delta \mathbf{H} \hat{\mathbf{H}}_T + \Delta \mathbf{H} \mathbf{F}_c$ is the equivalent TR channel response matrix of size $N_R \times N_R (2L-1)$ which is given by

$$\mathbf{H}_{TR} = \begin{pmatrix} \bar{\mathbf{h}}_{11} & \bar{\mathbf{h}}_{21} & \cdots & \bar{\mathbf{h}}_{N_R1} \\ \bar{\mathbf{h}}_{12} & \bar{\mathbf{h}}_{22} & \cdots & \bar{\mathbf{h}}_{N_R2} \\ \vdots & \vdots & \ddots & \vdots \\ \bar{\mathbf{h}}_{1N_R} & \bar{\mathbf{h}}_{2N_R} & \cdots & \bar{\mathbf{h}}_{N_RN_R} \end{pmatrix}_{N_R \times N_R (2L-1)}$$

where each vector $\bar{\mathbf{h}}_{ij}$ is a $1 \times (2L-1)$ auto-correlation ($i = j$) or cross-correlation ($i \neq j$) vector. Note that, the peak value of auto-correlation is located at the L^{th} index. By TR method, the desired auto-correlation part in the equivalent CIR for the TR-MIMO scenario forms a strong peak and dominates in the L^{th} sample of the received signal captured by any antenna [6].

We assume $\Delta \mathbf{H}$ and $\hat{\mathbf{H}}$ are mutually independent. Substituting \mathbf{H}_{TR} into (6), we have

$$\hat{\mathbf{H}}_T^H \hat{\mathbf{H}}^H \hat{\mathbf{H}}_T + \hat{\mathbf{H}}_T^H \hat{\mathbf{H}}^H \hat{\mathbf{H}} \mathbf{F}_c + \mathbf{F}_c^H \hat{\mathbf{H}}^H \hat{\mathbf{H}}_T + \mathbf{F}_c^H \hat{\mathbf{H}}^H \hat{\mathbf{H}} \mathbf{F}_c + \hat{\mathbf{H}}_T^H \mathbf{C}_{\Delta H} \hat{\mathbf{H}}_T + \hat{\mathbf{H}}_T^H \mathbf{C}_{\Delta H} \mathbf{F}_c + \mathbf{F}_c^H \mathbf{C}_{\Delta H} \hat{\mathbf{H}}_T + \mathbf{F}_c^H \mathbf{C}_{\Delta H} \mathbf{F}_c = \frac{1}{\rho} \mathbf{I} \quad (7)$$

With some manipulating of (7) we have

$$(\hat{\mathbf{H}}_T + \mathbf{F}_c)(\hat{\mathbf{H}}_T + \mathbf{F}_c)^H = \frac{1}{\rho} (\hat{\mathbf{H}}^H \hat{\mathbf{H}} + \mathbf{C}_{\Delta H})^{-1} \quad (8)$$

Finally, the elements of the estimation error compensator matrix F_C can be obtained from compensated pre-filter matrix $H_T = \hat{H}_T + F_C$ as

$$H_T H_T^H = \frac{1}{\rho} (\hat{H}^H \hat{H} + C_{\Delta H})^{-1} \quad (9)$$

where the non-square complex-valued matrix H_T can be found through the singular value decomposition (SVD) of (9) as follows [18].

Given the $N_T L \times N_R(2L-1)$ matrix H_T , let U be the $N_T L \times N_T L$ matrix whose columns are the orthogonal eigenvectors of $H_T H_T^H$, and V be the $N_R(2L-1) \times N_R(2L-1)$ matrix whose columns are the orthogonal eigenvectors of $H_T^H H_T$. Also, let r be the rank of the matrix H_T . Then, there is a SVD of H_T as $H_T = U \Sigma V^H$ where the eigenvalues $\lambda_1, \dots, \lambda_r$ of $H_T H_T^H$ are the same as the eigenvalues of

$$H_T^H H_T \text{ and also, for } 1 \leq i \leq r, \text{ let } \sigma_i = \sqrt{\lambda_i}, \text{ with } \lambda_i \geq \lambda_{i+1}.$$

Then the $N_T L \times N_R(2L-1)$ matrix Σ is composed by setting $\Sigma_{ii} = \sigma_i$ for $1 \leq i \leq r$, and zero otherwise. Thus based on (9) we have $H_T H_T^H = U \Sigma V^H V \Sigma^H U^H = U \Sigma \Sigma^H U^H$, that is, the left-hand side is a square symmetric matrix, and the right-hand side represents its symmetric diagonal decomposition. The values σ_i are referred to as the singular values of H_T . Then for (9) we have $U \Sigma \Sigma^H U^H = \frac{1}{\rho} (\hat{H}^H \hat{H} + C_{\Delta H})^{-1}$. As a result, the above discussion in the calculation of H_T from (9) can be expressed as the following subroutine in which a pseudo-code is presented for the numerical implementation of the proposed robust TR optimization algorithm based on MMSE criterion. This code is expressed as

- Compute the SVD of matrix $\frac{1}{\rho} (\hat{H}^H \hat{H} + C_{\Delta H})^{-1}$ in (9) and order its singular values, i.e., U_I , Σ_I and V_I as $[U_I, \Sigma_I, V_I] = \text{svd}\{\frac{1}{\rho} (\hat{H}^H \hat{H} + C_{\Delta H})^{-1}\}$.
- Set $U = U_I$.
- Construct a zero matrix as $\Delta O = \text{zeros}(N_T L, N_R(2L-1) - N_T L)$.
- Set $\Sigma = [\text{sqr}t(\Sigma_I) \quad O]$.
- Compute the SVD of matrix \hat{H}_T and order its singular values, i.e., U_θ , Σ_θ and V_θ as $[U_\theta, \Sigma_\theta, V_\theta] = \text{svd}\{\hat{H}_T\}$.
- Set $H_T \approx U \Sigma V_\theta^H$.

II. POWER LOADING

A. In Conventional TR-MIMO-UWB System

In transmission over parallel channels, it can happen that we are faced with sub-channels that would require enormous transmit power to achieve acceptable bit or symbol error rates, especially in an imperfect CSI case. In this case it is beneficial, given the fixed amount of transmit power

available, not to aim for equal error rates in all sub-channels, but perform an optimum power loading by minimizing the average bit error rate [16]. Some power allocation schemes are proposed in [10] to reduce the delay spread of the channel impulse response in the TR-MISO-UWB systems. Authors in [10] did not consider imperfect CSI case and also ISI and MSI effects on system performance in which their analysis is true in ideal and fantastic case. Therefore, based on previous findings such as [15] and [16], we propose a new power loading scheme for TR-MIMO-UWB systems by minimizing the average bit error rate (BER) at the receiver in an imperfect CSI scenario.

The received signal at the MIMO channel output with TR pre-filtering, as mentioned in Section 2, without the channel estimation error compensation is given by

$$y = (\hat{H} + \Delta H) \hat{H}_T x + n \quad (10)$$

where ΔH and n are assumed mutually independent and uncorrelated matrices. The received signal at j^{th} receive antenna can be expressed by

$$y_j = \underbrace{\sum_{i=1}^{N_T} \hat{h}_{ij} \bar{H}_{ij} x_j}_{\text{Signal}} + \underbrace{\sum_{i=1}^{N_T} \sum_{\substack{k=1 \\ k \neq j}}^{N_R} \hat{h}_{ij} \bar{H}_{ik} x_k}_{v_j} + \underbrace{\sum_{i=1}^{N_T} \sum_{k=1}^{N_R} \Delta h_{ij} \bar{H}_{ik} x_k}_{w_j} + \underbrace{n_j}_{\text{Noise}} \quad (11)$$

The first part of the received signal is the desired data symbol. In this part, the equivalent channel is the autocorrelation of channels. Also, v_j and w_j are the interference from other symbols and the interference from the channel estimation error, respectively. In v_j and w_j parts, the equivalent channel is the cross-correlation of channels, which is small generally in comparison with the former. Also, v_j and w_j terms in (11) appears as interference which degrades the performance of TR-MIMO-UWB system, especially in imperfect CSI. Some of this interference can be reduced by a MMSE equalizer, but, we try to maximize the Signal to Interference plus Noise Ratio (SINR) more than ever by a power allocation scheme. The SINR at the j^{th} received antenna is given by

$$SINR_j = \frac{\left\| \sum_{i=1}^{N_T} \hat{h}_{ij} \bar{H}_{ij} \right\|_F^2}{\left\| \sum_{i=1}^{N_T} \sum_{\substack{k=1 \\ k \neq j}}^{N_R} \hat{h}_{ij} \bar{H}_{ik} \right\|_F^2 + E\left\{ \left\| \sum_{i=1}^{N_T} \sum_{k=1}^{N_R} \Delta h_{ij} \bar{H}_{ik} \right\|_F^2 \right\} + E\left\{ \|n_j\|_F^2 \right\}} \quad (12)$$

where $\|\cdot\|_F$ denotes the Frobenius norm. If we define

$R_{ij} = \hat{h}_{ij} \bar{H}_{ij}$ as auto-correlation vector of the channel vector

\hat{h}_{ij} and, $C_{ik} = \hat{h}_{ij} \bar{H}_{ik}$ as cross-correlation vector of \hat{h}_{ij} with

other sub-channels then, the SINR at the j^{th} received antenna is expressed as

$$SINR_j = \frac{\sum_{i=1}^{N_T} \sum_{l=0}^{2L-2} |\mathbf{R}_{ij}(l)|^2}{\sum_{i=1}^{N_T} \sum_{\substack{k=1 \\ k \neq j}}^{N_R} \sum_{l=0}^{2L-2} |\mathbf{C}_{ik}(l)|^2 + L\sigma_e^2 \sum_{i=1}^{N_T} \sum_{k=1}^{N_R} \sum_{l=0}^{L-1} |\hat{\mathbf{h}}_{ik}(l)|^2 + \sigma_n^2} \quad (13)$$

where the estimation errors of the different sub-channels are assumed to be mutually independent, i.e., $\Delta \mathbf{h}_{ij} \perp \Delta \mathbf{h}_{mn}$ where \perp is the symbol, standing for mutual independence. If the channel estimation is perfect and also, because of focusing property of TR, we can neglect the interference part. Then the SNR is

$$SINR_j = \frac{\sum_{i=1}^{N_T} \sum_{l=0}^{2L-2} |\mathbf{R}_{ij}(l)|^2}{\sigma_n^2} \quad (14)$$

Performance of the TR-MIMO-UWB system depends on transceiver structure and the received signal properties, e.g., its probability density function (PDF). For $Lt_s \geq 5n\text{sec}$ where t_s is time resolution of the channel, the average numbers of paths is high, so using central limit theorem, the sum of a large number of independent, zero-mean random variables form a Gaussian PDF for the path gain [19]-[20]. But for $Lt_s < 5n\text{sec}$ path gain PDF isn't Gaussian and as the Lt_s increases, the non-Gaussian shape tends more to Gaussian, and the densities become more bell shaped [20]. According to the above discussion, the average BER of the TR-MIMO-UWB system, assuming BPAM modulation, can be derived approximately from Eq. (13) as

$$BER \approx \frac{1}{N_T} \sum_{j=1}^{N_T} Q(\sqrt{2SINR_j p_j}) \quad (15)$$

where p_j , $P_T = \sum_{j=1}^{N_T} p_j$ and $Q(x)$ are the transmit power assigned to j^{th} transmit antenna, the total transmitted available power and the Marcum Q-function, respectively.

$Q(x)$ is defined as

$$Q(x) = \frac{1}{\sqrt{2\pi}} \int_x^{+\infty} \exp(-t^2/2) dt \quad (16)$$

For simplicity, we assume $\sigma_x^2 = 1$, so that $P_T = N_T$. The optimum power allocation vector $\mathbf{P} = [p_1, \dots, p_{N_T}]^T$ that minimizes the average BER, when an imperfect CSI is presented, can be obtained by introducing the Lagrange function as

$$L_G = \frac{1}{N_T} \sum_{j=1}^{N_T} Q(\sqrt{2SINR_j p_j}) - \lambda (N_T - \sum_{j=1}^{N_T} p_j) \quad (17)$$

With partial derivative we obtain

$$\frac{\partial L_G}{\partial p_j} = \frac{-1}{2N_T \sqrt{\pi}} \sqrt{\frac{SINR_j}{p_j}} \exp(-SINR_j p_j) + \lambda \quad (18)$$

Solving $\partial L_G / \partial p_j = 0$ for p_j , we can allocate the power to each transmit antenna in a manner that

$$\left(\frac{1}{SINR_j}\right) p_j \exp(SINR_j p_j) = \frac{1}{4N_T^2 \lambda^2 \pi} \quad (19)$$

and finally

$$p_j(\lambda) = \frac{1}{SINR_j} W\left(\left(SINR_j\right)^2 \frac{1}{4N_T^2 \lambda^2 \pi}\right) \quad (20)$$

where $W(x)$ is the real valued Lambert's W-function defined as the inverse of the function $f(x) = x \exp(x)$ for $x \geq 0$, i.e., $W(x) = a \Leftrightarrow a \exp(a) = x$ [21]. Since the $W(x)$ function is real and concave, the unique solution for power allocation vector can be found by the following simple iterative procedure [22]

- Choose a positive λ , which fulfils

$$\sum_{j=1}^{N_T} (SINR_j) \frac{1}{4N_T^2 \lambda^2 \pi} \leq P_T \quad (21)$$

- Calculate

$$\hat{P}_T = \sum_{j=1}^{N_T} \frac{1}{SINR_j} W\left(\left(SINR_j\right)^2 \frac{1}{4N_T^2 \lambda^2 \pi}\right) \quad (22)$$

- If \hat{P}_T is not yet sufficiently close to P_T then multiply λ by P_T / \hat{P}_T and go back to step (2).
- Compute $\mathbf{P} = [p_1, \dots, p_{N_T}]^T$ according to (20).

Note that since $W(x)$ for $x > -1/e$ is a monotonic function then according to (20) the highest powers ($\max p_j$) are assigned to the weakest signals so the SINR values approximately stay constant for all sub-channels.

B. In Robust TR-MIMO-UWB System

Proposed power loading scheme presented in Section 4.1 can be combined with robust optimization strategy mentioned in Section 3, but TR pre-filter should be calculated in an imperfect CSI scenario. In this case, Eq. (10) can be rewritten by considering the compensator pre-filter as

$$\mathbf{y} = (\hat{\mathbf{H}} + \Delta \mathbf{H})(\hat{\mathbf{H}}_T + \mathbf{F}_C) \mathbf{x} + \mathbf{n} \quad (23)$$

The received signal at j -th receive antenna can be expressed by

$$\begin{aligned} y_j = & \underbrace{\sum_{i=1}^{N_T} (\hat{\mathbf{h}}_{ij} \bar{\mathbf{H}}_{ij} + \Delta \mathbf{h}_{ij} \bar{\mathbf{F}}_{ij}) x_j}_{\text{Signal}} \\ & + \underbrace{\sum_{i=1}^{N_T} \sum_{\substack{k=1 \\ k \neq j}}^{N_R} (\hat{\mathbf{h}}_{ij} \bar{\mathbf{H}}_{ik} + \Delta \mathbf{h}_{ij} \bar{\mathbf{F}}_{ik}) x_k + \sum_{i=1}^{N_T} \sum_{k=1}^{N_R} (\Delta \mathbf{h}_{ij} \bar{\mathbf{H}}_{ik} + \hat{\mathbf{h}}_{ij} \bar{\mathbf{F}}_{ik}) x_k}_{\text{Interference}} + \underbrace{n_j}_{\text{Noise}} \end{aligned} \quad (24)$$

Then, the SINR at the j -th receive antenna is given by

$$SINR_j = \frac{\left\| \sum_{i=1}^{N_T} \hat{\mathbf{h}}_{ij} \bar{\mathbf{H}}_{ij} \right\|_F^2 + \left\| \sum_{i=1}^{N_T} \Delta \mathbf{h}_{ij} \bar{\mathbf{F}}_{ij} \right\|_F^2}{\left\| \sum_{i=1}^{N_T} \sum_{\substack{k=1 \\ k \neq j}}^{N_R} \hat{\mathbf{h}}_{ij} \bar{\mathbf{H}}_{ik} \right\|_F^2 + \left\| \sum_{i=1}^{N_T} \sum_{k=1}^{N_R} \hat{\mathbf{h}}_{ij} \bar{\mathbf{F}}_{ik} \right\|_F^2 + dh_j + E\{n_j\|_F^2\}} \quad (25)$$

Where the value dh_j is defined as

$$dh_j = E\left\{ \left\| \sum_{i=1}^{N_T} \sum_{k=1}^{N_R} \Delta \mathbf{h}_{ij} \bar{\mathbf{H}}_{ik} \right\|_F^2 + \left\| \sum_{i=1}^{N_T} \sum_{\substack{k=1 \\ k \neq j}}^{N_R} \Delta \mathbf{h}_{ij} \bar{\mathbf{F}}_{ik} \right\|_F^2 \right\} \quad (26)$$

In addition to \mathbf{R}_{ij} and \mathbf{C}_{ik} , if we define $\mathbf{C}'_{ik} = \hat{\mathbf{h}}_{ij} \bar{\mathbf{F}}_{ik}$ as cross-correlation vector of $\hat{\mathbf{h}}_{ij}$ with

$f_{ik} = [f_{ik}[0], \dots, f_{ik}[L], \dots, f_{ik}[L-1]]_{1 \times L}$ where $k \neq j$, then, the SINR at the j^{th} receive antenna is obtained as

$$SINR_j = \frac{\sum_{i=1}^{N_r} \sum_{l=0}^{2L-2} |\mathbf{R}_{ij}(l)|^2 + L\sigma_e^2 \sum_{i=1}^{N_r} \sum_{l=0}^{L-1} |f_{ij}(l)|^2}{\sum_{i=1}^{N_r} \sum_{k=1}^{N_r} \sum_{l=0}^{2L-2} |C_{ik}(l)|^2 + \sum_{i=1}^{N_r} \sum_{k=1}^{N_r} \sum_{l=0}^{2L-2} |C_{ik}(l)|^2 + dh_j + \sigma_n^2} \quad (27)$$

where dh_j is obtained as

$$dh_j = L\sigma_e^2 \sum_{i=1}^{N_r} \sum_{k=1}^{N_r} \sum_{l=0}^{L-1} |\hat{h}_{ik}(l)|^2 + L\sigma_e^2 \sum_{i=1}^{N_r} \sum_{k=1}^{N_r} \sum_{l=0}^{L-1} |f_{ik}(l)|^2 \quad (28)$$

in which the estimation errors of the different sub-channels are assumed to be mutually independent, i.e., $\Delta \mathbf{h}_{ij} \perp \Delta \mathbf{h}_{mn}$.

Power loading scheme can be obtained in the robust optimized system by replacing Eq. (27) into Eqs. (20), (21) and (22), and using the iterative procedure mentioned in [8]. If the channel estimation is assumed to be perfect, we can neglect the interference terms caused by the channel estimation error, and then the SNR can be written as

$$SNR_j = \frac{\sum_{i=1}^{N_r} \sum_{l=0}^{2L-2} |\mathbf{R}_{ij}(l)|^2 + L\sigma_e^2 \sum_{i=1}^{N_r} \sum_{l=0}^{L-1} |f_{ij}(l)|^2}{\sigma_n^2} \quad (29)$$

As it can be seen from (29), SNR_j values are larger than its counterpart in Eq. (14). Increase in the SNR_j values in Eq. (29) relative to Eq. (14) is because of the error compensator coefficients $f_{ij}(l)$ obtained in robust optimization scheme in Section 3. Therefore, it is expected that the power loading scheme in robust optimization, outperforms relative to conventional TR-MIMO-UWB system in an imperfect CSI. This expression will be denoted by simulation. If $\mathbf{F}_C = 0$ then we obtain the power allocation scheme in conventional TR-MIMO-UWB system in an imperfect CSI scenario.

III. SIMULATIONS AND RESULTS

To evaluate the performance of the proposed optimization methods (robust optimization and power loading) for the TR-MIMO-UWB system, Monte Carlo simulations are conducted in this section. As in [5], the second-order derivative of Gaussian pulse has been used as the transmitted pulse $p(t)$, which is mathematically defined as [5]

$$p(t) = [1 - 4\pi(\frac{t-t_c}{T_p})^2] e^{-2\pi(\frac{t-t_c}{T_p})^2} \quad (30)$$

where T_p is a parameter corresponding to pulse width, and t_c is a time shifting of the pulse. In the following simulations, we consider $T_p = 5ns$, and $t_c = 2.5ns$. Also, one pulse per symbol is assumed, i.e., symbol duration T is assumed $5nsec$ where is equal to transmission rate of $200Mbps$ with BPAM modulation and also, sampling time $t_s = 0.167nsec$ is considered. We assume that the signal is transmitted over UWB channels and perfectly synchronized at receiver. The most widely adopted UWB multipath channel model has been proposed by the IEEE 802.15.3a Task Group [23-24]. According to this proposal, slow fading, dense multipath and quasi-statistic are the key features of the UWB channel. Four scenarios were proposed: CM1-based on line of sight (LOS)

0–4m length, CM2-based on non-LOS (NLOS) 0–4 m, CM3-based on NLOS 4–10 m, and CM4 based on an extreme NLOS environment. As in [5], we use the IEEE 802.15.3a CM4 channel model for each channel in simulations to evaluate our proposed solutions in the worst case scenario of the indoor multipath channels.

To optimize the TR-MIMO-UWB system performance of Fig.1 and to compensate the channel estimation error by pre-filter, we use the robust optimization scenario mentioned in Section 3. The entries of $\Delta \mathbf{H}$ are assumed to be zero mean *i.i.d.* complex Gaussian random variables. In our simulations, we consider 3 values for the estimation error

variance as $\sigma_e^2 = 0.1, 0.2$ and 0.3 . The performance of uncoded TR-MIMO-UWB system with robust optimization scheme is shown in Fig. 2 in imperfect CSI. It can be seen that, for the particular values of the estimation error variance considered in this section, the BER performance of 2×2 TR-MIMO-UWB is considerably improved. For example, with $\sigma_e^2 = 0.1$, the SNR can be improved about 4dB at the average BER = 10^{-3} .

In Figs. 3 and 4, the equivalent CIRs for a 2×2 TR-MIMO-UWB system are compared in perfect and imperfect CSI where $\sigma_e^2 = 0.1$ is assumed. It should be noted that the signal transmitted over the desired channel is focused into a narrow time instant, while ISI channel spreads the signal. This property is useful for ISI mitigation when the signal is transmitted over long delay spread channel [5]. But according to Figs. 3 and 4, in an imperfect CSI, the delay spread of the equivalent channel is increased as compared with perfect CSI. This channel imperfection degrades the performance of TR-MIMO-UWB system. As it is shown in Figs. 3 and 4, the time focusing feature of the TR technique in the robust optimized TR-MIMO-UWB system is yet preserved. Figs. 3 and 4 denote the temporal focusing property of TR technique in four sub-channels, before and after the robust optimization. Someone can understand the time compression of the energy (power) at the center of the compressed equivalent TR response from these figures. But, it might be possible for another one to feel and understand the time focusing of TR method by focusing gain better than the plotted figures. For more understanding of this, according to [25]-[26], focusing gain (FG) is defined as the ratio of the strongest tap power to the total tap power of the received equivalent TR response. If we define the equivalent TR response between i -th transmit antenna and j -th receive antenna as $\bar{\mathbf{h}}_{ij} = [\bar{h}_{ij}[-(L-1)], \dots, \bar{h}_{ij}[0], \dots, \bar{h}_{ij}[L-1]]$, then focusing gain (FG_{ij}) according to [25]-[26] is given by

$$FG_{ij} = \frac{|\bar{h}_{ij}[0]|^2}{\sum_{l=-(L-1)}^{L-1} |\bar{h}_{ij}[l]|^2} \quad (31)$$

We obtained this ratio by averaging over 100 multipath channel realizations between transmit and receive antennas and tabulated in Table 1. As it can be seen from Table 1, the FG in robust optimized TR scheme is more than the imperfect CSI case and less than the perfect CSI scenario. This result proves the performance improvement of Fig. 2 and the temporal focusing of Figs. 3 and 4.

In addition to the robust optimization scheme, we use the

proposed power loading solution mentioned in Section 4 to improve the TR-MIMO-UWB system performance more than ever. In Fig. 5, we can observe the performance of the proposed power loading for the robust optimization. As can be seen from this figure, for instance in $\sigma_e^2 = 0.1$, the performance of power loading is noticeable, especially for high SNR values. Also, as it can be seen from Table 1, the FG in the power loading scheme is more than the robust optimization scheme. This means that the power loading method outperforms the robust optimization scheme. For validity of this, as it can be realized from Fig. 5, the power loading scheme has better performance relative to robust optimization method, especially for high SNR. Such as, according to Fig. 5, for $\sigma_e^2 = 0.1$, the power loading scheme substantially outperforms the robust optimization method about 2dB SNR at the average BER= 10^{-3} .

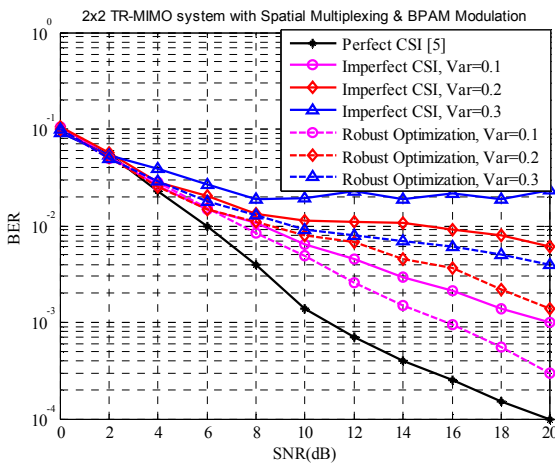


Fig. 2. BER performance of 2x2 TR-MIMO-UWB with robust optimization.

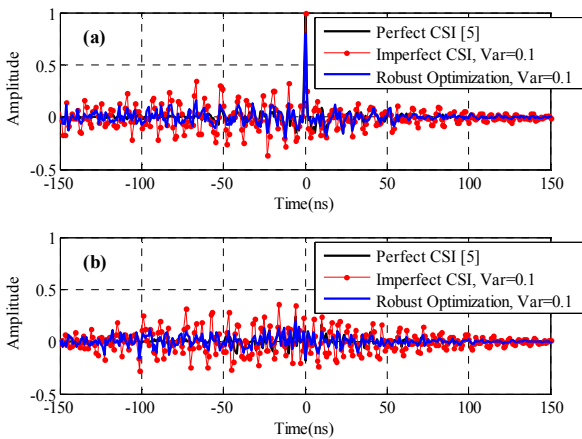


Fig. 3. Plotting (a) \bar{h}_{11} and (b) \bar{h}_{21} of the matrix \mathbf{H}_{TR} (Impulse response of 2×2 TR-MIMO-UWB equivalent channel with pulse shaping).

TABLE I
COMPARISON OF THE PROPOSED SCHEMES (ROBUST OPTIMIZATION & POWER LOADING) IN FOCUSING GAIN TERM BEFORE AND AFTER OPTIMIZATION FOR $\sigma_e^2 = 0.1$

Sub-channel Index	Perfect CSI	Imperfect CSI	Robust Optimization Scheme	Power Loading Scheme
\bar{h}_{11}	0.6621	0.2264	0.3740	0.5643
\bar{h}_{21}	0.0792	0.0236	0.0375	0.0534
\bar{h}_{12}	0.0769	0.0214	0.0332	0.0521
\bar{h}_{22}	0.6577	0.2163	0.3565	0.5536

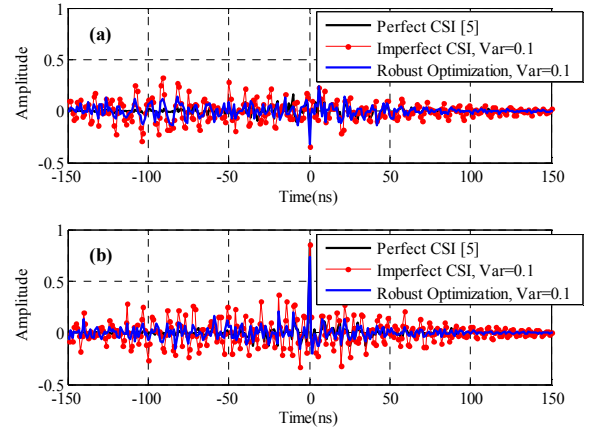


Fig. 4. Plotting (a) \bar{h}_{12} and (b) \bar{h}_{22} of the matrix \mathbf{H}_{TR} (Impulse response of 2×2 TR-MIMO-UWB equivalent channel with pulse shaping).

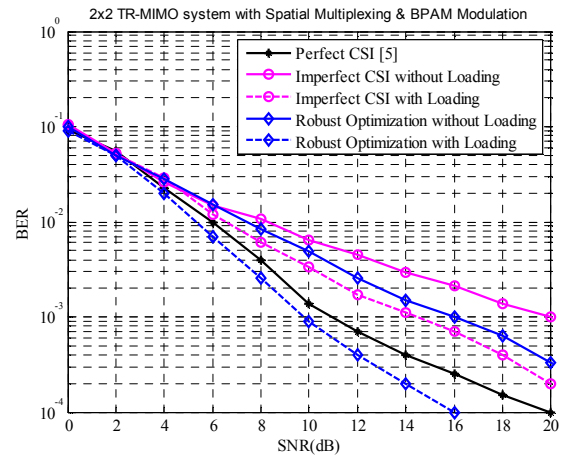


Fig. 5. Power loading in robust optimization for imperfect CSI and $\sigma_e^2 = 0.1$.

IV. CONCLUSION

The imperfect CSI effects, caused by channel estimator error, on TR-MIMO-UWB system were considered in this paper. At first, a pre-filtering approach as robust optimization scheme based on MMSE equalizer is developed. We observed that the robust optimization technique considerably improved the BER performance of 2×2 TR-MIMO-UWB system, where temporal focusing feature of the TR technique in the robust optimized TR-MIMO-UWB system was kept, especially for high SNR values. For instance, 2×2 TR-MIMO-UWB system with the

proposed robust optimization scheme was improved about 4dB SNR at the average BER= 10^{-3} for $\sigma_e^2 = 0.1$. Then, the power loading strategy was proposed for the imperfect CSI and the robust optimized cases. It was observed that it brought a performance gain in the 2x2 TR-MIMO-UWB system in an imperfect CSI scenario and the robust optimized system. Also, it was seen that the power loading scheme has better performance relative to robust optimization method, especially for high SNR. For example in $\sigma_e^2 = 0.1$, the power loading scheme substantially outperforms the robust optimization method about 2dB SNR at the average BER= 10^{-3} .

Note that we proposed the general new solutions for the wireless personal area network (WPAN) TR-MIMO-UWB systems in this paper. It is clear that our methods can be especially used in the extremely multipath indoor environments as the short-range high-data rate transmission, such as, downlink scenario of the access point to the handsets in the indoor environments, the multimedia and other high-data rate transmissions in a wireless home networking and so on.

REFERENCES

- [1] F. Nekoogar, "Ultra-wideband communications: fundamentals and applications", *Pearson Education, First printing*, September 2005.
- [2] Jeffrey H. Reed, "An Introduction to Ultra Wideband Communication Systems", *Prentice Hall PTR*, April 05, 2005.
- [3] G. Foschini and M. Gans, "on the limits of wireless communications in a fading environment when using multiple antennas", *Wireless Pers. Commun.*, 1998, 6, (3), pp.311-335.
- [4] C. Zhou, N. Guo and R. C. Qiu, "Time-Reversed Ultra wideband (UWB) Multiple Input-Multiple Output (MIMO) Based on Measured Spatial Channels", *IEEE Transactions on Vehicular Technology*, 2009, p.p. 1-15.
- [5] H. Nguyen, F. Zheng and T. Kaiser, "Antenna selection for time reversal MIMO UWB systems", In *IEEE 69th Vehicular Technology Conf.*, Barcelona, Spain, 26-29 April 2009.
- [6] T. Kaiser and F. Zheng, "Ultra Wideband Systems with MIMO", *John Wiley & Sons Ltd, UK*, 2010.
- [7] R. J. Cramer, R. A. Scholtz, and M. Z. Win, "Evaluation of an Ultra-Wide-Band Propagation Channel," *IEEE Trans. Ant. Prop.*, Vol. 50, No. 5, pp. 561-570, May 2002.
- [8] R. J. Cramer, "An evaluation of ultra wideband propagation channels," *Ph.D. dissertation, Univ. Southern Calif., Los Angeles, CA*, Dec. 2000.
- [9] T. Strohmer, M. Emami, J. Hansen, G. Papanicolaou, and A. J. Paulraj, "Application of time reversal with MMSE equalizer to UWB Communications", *Proc. IEEE Global Telecommunications Conference*, Dallas, Texas, Nov.29-Dec.3, 2004, pp.3123-3127.
- [10] P. Kyristi, G. Panicolaou, and A. Oprea, "MISO time reversal and 918 delay-spread compression for FWA channels at 5 GHz," *IEEE Antennas 919 Wireless Propag. Lett.*, Dec. 2004, vol. 3, pp. 96-99.
- [11] I. H. Naqvi, P. Besnier and G. El Zein, "Robustness of a time-reversal ultra wideband system in non-stationary channel environment", *IET Microwaves, Antennas and Propagation*, March 2011, Vol. 5, No. 4, pp. 468-475.
- [12] X. Liu, B. Z. Wang, S. Xiao and S. Lai, "Post-Time-Reversed MIMO Ultrawideband Transmission Scheme", *IEEE Transactions on Antennas and Propagation*, May 2010, vol. 58, no.5, pp.1731-1738.
- [13] H. Khaleghi Bizaki, S. Alizadeh, "Mitigation of Channel Estimation Error in TR-UWB system based on a Novel MMSE Equalizer", *Springer Annals of Telecommunications*, doi: 10.1007/s12243-012-0325-8, published online: 06 Oct. 2012.
- [14] S. Alizadeh, H. Khaleghi Bizaki and M. Okhovvat, "Effect of Channel Estimation Error on Performance of Time Reversal-UWB Communication System and its Compensation by Pre-filter", *IET Communications*, vol. 6, no. 12, pp.1781-1794, Nov. 2012.
- [15] H. K. Bizaki and A. Falahati, "Tomlinson-Harashima precoding with imperfect channel state information", *IET. Communication journal*, vol.2, no.1, pp.151-158, January 2008.
- [16] C. Windpassinger, "Detection and Pre-coding for Multiple Input Multiple Output Channels," *Ph.D. dissertation, University of Erlangen, Nürnberg*, June 2004.
- [17] K. B. Petersen, and M. S. Pedersen, "The Matrix Cookbook", Feb. 2006, page 17.
- [18] C. D. Manning, P. Raghavan and H. Schütze, "An Introduction to Information Retrieval", *Cambridge University Press, Cambridge, England*, Chapter 18, April 2009.
- [19] K. Witrisal, "Statistical analysis of the IEEE 802.15.4a UWB PHY over Multipath Channels", *IEEE Wireless Communications and Networking Conference, WCNC2008*, March 31-April 3 2008.
- [20] D. Abbasi-moghadam, V. Tabataba Vakili, "Characterization of Indoor Time Reversal UWB Communication Systems: Spatial, Temporal and Frequency Properties", *Wiley International Journal of Communication Systems*, doi:10.1002/dac.1140, published online 28 April 2010.
- [21] R.M. Corless, G.H. Gonnet, D.E.G. Hare, D.J.Jeffrey, and D.E. Knuth, "On the Lambert W Function", *Advances in Computational Mathematics*, volume 5, 1996, pp. 329-359.
- [22] T. Hunziker, D. Dahlhaus, "Optimal Power Adaptation for OFDM Systems with Ideal Bit-Interleaving and Hard-Decision Decoding", *IEEE International Conference on Communications (ICC)*, vol. 5, 2003, pp.3392-3397.
- [23] J. Foerster et al., "Channel modeling sub-committee report final," *IEEE P802.15 Wireless Personal Area Networks, P802.15-02/490r1-SG3a*, Feb. 2003.
- [24] A. F. Molisch, K. Balakrishnan, D. Cassioli, C. Chong, S. Emami, A. Fort, J. Karedal, J. Kunisch, H. Schantz, U. Schuster, and K. Siwiak, "IEEE 802.15.4a Channel model final report," Tech. Rep.
- [25] A. Akogun, R. C. Qiu, and N. Guo, "Demonstrating time-reversal in ultra-wideband communications using time domain measurements", *The Instrumentation, Systems and Automation (ISA) 51st International Instrumentation Symposium, Knoxville, Tennessee*, May 2005, pp.1-5.
- [26] A. E. Akogun, "Theory and application of time reversal technique to ultra-wideband wireless communication", *MSc. dissertation, Tennessee Technological University*, August 2005.



Sajjad Alizadeh was born in Roudsar, Guilan Province, Iran on November 3, 1983. He received the Associate Degree (A.D.) from Electronics Engineering College (Electronics Industry University) of Shiraz University (Shiraz University of Technology (SUTECH) today), Shiraz, Iran, in 2005 and the B.Sc. degree from Shahid Rajaei Teacher Training University (SRTTU), Tehran, Iran, in 2007, both in electronics. Also he received the M.Sc. degree in Communication Engineering from Imam Hossein University (IHU), Tehran, Iran, in 2011. He has served

as a referee in IET Communications journal. His current research interests are in the area of UWB wireless communications with special emphasis on digital and statistical signal processing, Time Reversal signaling, propagation channels modeling, multiple-antenna (MIMO) schemes, Cognitive Radio networks, and blind detection and parameters estimations in spread spectrum systems.



Hossein Khaleghi Bizaki received his PhD degree in Electrical Engineering, Communication system, from Iran University of Science and Technology (IUST), Tehran, Iran, in 2008. Dr. Bizaki started his work as assistant professor in 2008. Now, he is author or co-author of more than 30 publications. His research interests include Information Theory, Coding Theory, Wireless Communication, MIMO Systems, Space Time Processing, and other topics on Communication System and

Signal Processing.

ISSN 1805-5443



9 771805 544136

02 >